University of Strathclyde

CNQO (Computational Nonlinear and Quantum Optics),
Department of Physics, Faculty of Science

National Physical Laboratory

Atomic Clocks & Sensors, Time & Frequency

The Spontaneous Symmetry Breaking of Light in Passive Kerr Ring Resonators

---

By Lewis Hill

Supported by:

Supervisor:	Prof. Gian-Luca Oppo
NPL Advisor:	Dr Pascal Del'Haye
International Placement:	Assoc. Prof. Stéphane Coen
Second Supervisor:	Dr Alison Yao

A thesis presented for the degree of
Doctor of Philosophy

December 2020

Abstract

Kerr ring resonators, where laser light circulates and interacts with a nonlinear medium, have a vast range of applications, especially in the field of metrology and telecommunications. An important feature that can occur in Kerr ring resonator setups with two field components is a spontaneous symmetry breaking (SSB) of the intensities of the circulating fields. At low input powers, the two components circulate in the resonator with the same intensity, but this symmetry may spontaneously break upon a minute change of input conditions resulting in one component becoming dominant while the other is suppressed. This thesis concerns the study of this symmetry breaking phenomenon and the features that can be exploited in wide-reaching applications in photonics and quantum technologies.

In early chapters we provide an introduction to passive Kerr ring resonators both in terms of the theoretical and experimental setups, and to the established model used to describe a single light beam circulating in a Kerr ring resonator, the Lugiato-Lefever equation (LLE). Systems of coupled LLEs are then used to model multiple modes circulating simultaneously in the resonator. We proceed to describe SSB in the intensities of these modes upon changes of experimentally controllable parameters. Through a linear stability analysis of the system of coupled equations we investigate the possible dynamical regimes starting from useful field oscillations and leading to the novel behaviour of periodic switching between the dominant and suppressed field components. Later, to describe a wide range of experimental setups, this analysis is generalised to arbitrary self- and cross-phase modulation strengths.

In subsequent chapters we describe our studies into how Temporal Cavity Solitons (TCS) evolve within the coupled LLE system. TCS have themselves a wide range of applications in the generation of, for example, optical frequency combs. It is shown for the first time and with external experimental verification, that TCS may also experience SSB in Kerr ring resonators with orthogonal polarization modes, a result which may lead to novel telecommunications applications. These symmetry broken TCS can, under certain conditions, begin to 'breath' in simple and complex manners and even show the periodic switching of the dominant and suppressed components previously mentioned, only now in self-localised pulses instead of continuous waves.

The final chapter of this thesis describes significant advances in two projects which lay the ground for further study. The first section builds on the balancing of asymmetric input conditions in a manner that restores a connected perturbed pitchfork bifurcation. This is important for applications looking to utilise interchangeable suppressed and dominant field roles in systems with physical imperfections. In the second we outline the derivation and early simulations of a new model which expands to four field components. It is shown how the enlarged degrees of freedom leads to 'nested' symmetry breaking bifurcations, opening new avenues for applications requiring more diversity and flexibility than just two coupled components.

Acknowledgements

I would like to give special thanks to my supervisor, **Gian-Luca Oppo**, for his guidance and assistance throughout the duration of this project. I would also like to give my thanks to others who have provided their supervision at various stages: **Pascal Del'Haye**, **Stéphane Coen** and **Alison Yao**.

Owed to their kindness, love and support my **extended family** has my tremendous gratitude, but specifically my **Mother** and **Step-father**, **Father** and **Step-mother**, and **Grandparents**.

For their social and emotional support throughout my time living in New Zealand during the COVID-19 pandemic I give my thanks to **Emma**, **Julena**, **Dave**, **Merkx** and **Oscar**.

Atop the many individuals who have aided me in my doctoral journey, I have also been supported by the following collectives: **SDS** (Strathclyde Doctoral School), the **PGI** (PostGraduate Institute for Measurement Science) and **SUPA** (Scottish Universities Physics Alliance), who have my thanks.

Author's Bibliography

Publications for peer-reviewed journals

- M.T.M. Woodley, J.M. Silver, **L. Hill**, F. Copie, L. Del Bino, S. Zhang, G.-L. Oppo and P. Del'Haye. "Universal symmetry-breaking dynamics for the Kerr interaction of counterpropagating light in dielectric ring resonators". Physical Review A 98 (5), 053863, 2018

- **L. Hill**, G.-L. Oppo, M.T.M. Woodley and P. Del'Haye. "Effects of self-and cross-phase modulation on the spontaneous symmetry breaking of light in ring resonators". Physical Review A 101 (1), 013823, 2020

- G. Xu, A. Nielsen, B. Garbin, **L. Hill**, G.-L. Oppo, J. Fatome, S.G. Murdoch, S. Coen and M. Erkintalo. "Spontaneous symmetry breaking of dissipative optical solitons in a two-component Kerr resonator". arXiv preprint arXiv:2008.13776, 2020

- M.T.M. Woodley*, **L. Hill***, L. Del Bino, G.-L. Oppo and P. Del'Haye. "Self-switching Kerr oscillations of counter-propagating light in microresonators". Physical Review Letters 126 (4), 043901, 2021

Oral Presentations at Peer-reviewed U.K. Conferences

- **L.Hill**, M.T.M. Woodley, G.-L. Oppo, J.M. Silver and P. Del'Haye. "A Spontaneous Symmetry Breaking of Light in Ring Resonators". Photon 2018.

- **L.Hill** "Characteristics of the spontaneous symmetry breaking of light in ring resonators, for application in photonic devices". CAPS 2019.

- **L.Hill**, G. Xu, A. Nielsen, B. Garbin, J. Fatome, G.-L. Oppo, S.G. Murdoch, M. Erkintalo and S. Coen. "Symmetry Broken Solitons and Breathers, and Self-switching Dynamics, in Ring Resonators". Photon 2020.

- **L.Hill**, M.T.M. Woodley, G.-L. Oppo, and P. Del'Haye. "Experimental and theoretical observation of mode switching of counter-propagating light in micro-resonators". Photon 2020.

* Co-first authors

Oral Presentations at Peer-reviewed International Conferences

• G. Xu, A. Nielsen, B. Garbin, J. Fatome, **L. Hill**, G.-L. Oppo, S.G. Murdoch, M. Erkintalo and S. Coen. "Spontaneous polarization symmetry breaking of temporal cavity solitons in optical Kerr resonators". CLEO PR 2020, OSA Technical Digest (Optical Society of America, 2020), paper C2B4.

• G. Xu, A. Nielsen, B. Garbin, J. Fatome, **L. Hill**, G.-L. Oppo, S.G. Murdoch, M. Erkintalo and S. Coen. "Spontaneous symmetry breaking of Kerr cavity solitons". Nonlinear Photonics, NpTu1D. 2

• **L. Hill**, G. Xu, J. Fatome, G.-L. Oppo, S.G. Murdoch, M. Erkintalo and S. Coen. "Breathing dynamics of symmetry-broken polarized temporal cavity solitons in Kerr ring resonators". Nonlinear Photonics, NpTu1D. 3

Poster Presentations at Peer-reviewed U.K. Conferences

• **L. Hill**, G.-L. Oppo, M.T.M. Woodley and P. Del'Haye. "A Spontaneous Symmetry Breaking of Light in Ring Resonators". Postgraduate Institute for Measurement Science Annual Conference 2018.

• **L. Hill**, G.-L. Oppo, M.T.M. Woodley, J.M. Silver and P. Del'Haye. "Spontaneous Symmetry Breaking of Light in Ring Resonators". SUPA Annual Gathering 2018.

• **L. Hill**, G.-L. Oppo, M.T.M. Woodley and P. Del'Haye. "Generality of the symmetry breaking of light in ring resonators". SUPA Annual Gathering 2019.

Poster Presentations at Peer-reviewed International Conferences

• **L. Hill**, G.-L. Oppo, M.T.M. Woodley, J.M. Silver and P. Del'Haye. "Spontaneous Symmetry Breaking of Light in Ring Resonators". YAO 2018.

• M.T.M. Woodley, J.M. Silver, **L. Hill**, F. Copie, L. Del Bino, S. Zhang, G.-L. Oppo and P. Del'Haye. "Spontaneous Symmetry Breaking, Oscillations, and Chaotic Regimes in Bidirectionally-Pumped Ring Resonators". CLEO/Europe-EQEC 2019.

"What is not started will never get finished.""

– Johann Wolfgang von Goethe

Contents

CONTENTS

Chapter 1

Introduction

Owed to the demonstration of the first laser by Theodore H. Maiman in 1960, the field of nonlinear optics has grown significantly in recent decades. Nonlinear optical effects occur as a consequence of a medium's optical properties being altered by their interaction with light [1], which, although not a necessity - see the observation of saturation effects in the luminescence of dye molecules by G.N. Lewis *et al.* in 1941 [2], often requires very high intensity light. This high intensity light is most commonly supplied through the use of a laser.

As an example of a nonlinear effect, consider momentarily the polarisation, $P(t)$, or dipole moment per unit volume, of a material in response to an applied optical field $E(t)$. In contrary to conventional optics, where the induced polarisation field is often described by

$$P(t) = \epsilon_0 \chi^{(1)} E(t) , \tag{1.1}$$

for linear susceptibility $\chi^{(1)}$ and permittivity of free space ϵ_0, in nonlinear optics the polarisation field is better described by following power series

$$P(t) = \epsilon_0 \left[\chi^{(1)} E(t) + \chi^{(2)} E(t)^2 + \chi^{(3)} E(t)^3 + ... \right] , \tag{1.2}$$

where $\chi^{(2-3)}$ are the second- and third-order nonlinear optical susceptibilities respectively. From Eq. (1.2) one observes that, at difference with Eq. (1.1), the polarisation of the material depends in a nonlinear manner on the applied field.

Throughout this thesis we concern ourselves with a special type of nonlinear material - Kerr materials [3,4] - which simplify Eq. (1.2) while still maintaining the possibility to exhibit nonlinear phenomena. Specifically, we study systems made up of continuous Kerr materials which form a connected path or closed loop wave guide for light to travel along. These types of setups are commonly referred to as Kerr ring resonators.

Kerr ring resonators [5] have seen application in a multitude of different fields, including many areas of metrology (for example through the generation of frequency combs [6–13] and improving rotation sensors through enhancing the Sagnac effect [14–18]), telecommunications (by, for example, storing and transferring data using temporal cavity solitons [19–22]), and in the production of components for use in photonic circuits such as isolators and circulators [23] and acting as logic gates [24]. Many of the recent advancements have been owed to the development of high-quality factor resonators [25–29], within which light circulates for many round trips of the closed loop wave guides before exiting - leading to a strong build up of nonlinear effects and allowing for optical bistability [5, 30].

The propagation of a single light field around these ring resonators is often modeled by the Lugiato-Lefever equation [31]. When multiple light fields circulate in Kerr ring resonators simultaneously they can interact with one another as they propagate. This interaction causes coupling effects and leads to coupled equations which can exhibit even more complex dynamics than the single LLE, thus yielding the potential for yet further applications. In this thesis we study in particular two physical situations. The first involves the propagation of two light fields moving in opposing directions, or counter-propagating, with a shared linear polarisation [14, 32], whereas the second involves two fields which co-propagate in the same direction, only now with orthogonal polarisations [33].

In both of these two-field systems, the propagating light fields can exhibit a fascinating effect: spontaneous symmetry breaking, and it is this effect which forms the basis of study for this manuscript.

This thesis is organised as follows.

In **Chapter 2** we provide the reader with an adequate introduction to passive Kerr ring resonators such that the rest of the thesis is grounded in the wider research topic and there is understanding of the prerequisite material that this thesis is based upon. With this said, further background material is still introduced in subsequent chapters as it becomes relevant. In this main chapter of introduction we begin by describing the theoretical set up of a ring resonator and outline some of the key physics involved as light propagates around them. This allows us to derive the well-known Lugiato-Lefever Equation (LLE), for which we then go on to provide methods for solving.

Chapter 3 then begins the main discussion of this thesis, "The Spontaneous Symmetry Breaking of Light in Passive Kerr Ring Resonators". We in-

troduce the two physical situations that are studied through out this manuscript: two co-propagating circularly polarised light fields, a situation modeled with two coupled LLEs, and two counter-propagating linearly polarised light fields, modeled by two coupled Lorentzian equations. It is shown that under certain conditions, notably when the circulating field envelopes are homogeneous (field envelope is constant around the resonator) and stationary (field envelope is constant in time), these two systems are mathematically akin. These homogeneous and stationary solutions (HSS) are then shown in multiple ways to display the potential for a Spontaneous Symmetry Breaking (SSB), where of the two field intensities, which were circulating as equals, one field becomes spontaneously dominant, while the other is suppressed. We then go on to access the stability of these HSS by removing the stationary constraint on the system.

Picking up where we left off, **Chapter 4** continues with the studies of the time dependent system, only now rather than studying the local stability of the HSS we investigate the wider dynamics by numerically integrating the equations. This allows us to predict the field evolutions over time and observe, for example, the oscillations that the fields undergo when the HSS becomes unstable to noise. These oscillations can be harmonic in nature, or they can become extremely complex and chaotic. To visualise the types of oscillations viable within the system we map out Poincaré sections, which mark the local maxima of the oscillations and hence give insight into their complexity. We go on to demonstrate that for certain input parameters the field oscillations can become so large that the ranges of their intensity evolutions overlap entirely, a process which can lead to the interesting dynamic of periodic self-switching.

In reading these early chapters it will become apparent that we have limited ourselves to certain values of the so called self- and cross-phase modulation (SPM and XPM) within our coupled systems. This choice was made due to the experimental parameters provided by collaborators. In **Chapter 5** we widen the scope of our studies to address the same coupled systems but with arbitrary strengths of the SPM and XPM. We begin the chapter with a short introduction describing exactly what SPM and XPM, are and why they arise within the system, before giving examples of what strengths they can take in our studied systems - and hence illustrating why it is important for the analysis to be expanded to incorporate these arbitrary strengths. It is shown that the SPM and XPM influence many behaviours in the system, from the possible range of the well known optical bistability to the size and shape of the set of asymmetric solutions. We end the chapter by generalising the stability analysis of the HSS to arbitrary SPM and XPM strengths and observing the effects of these strengths on the oscillatory behaviour of the field evolutions.

In **Chapter 6** we remove the homogeneous character of the solutions. This allows us to study how the fields vary during their circulations of the resonator, leading to behaviours such as Turing patterns and Temporal Cavity Solitons (TCS). While TCS have been known to exist in LLE systems for some time, we show here that TCS in our coupled systems can also undergo SSB, leading to two soliton profiles with different peak intensities. We go on to show that these solitons, under certain conditions, can begin to also show oscillatory behaviours - commonly referred to as 'breathing'. Again these oscillation or breathing dynamics can be simple or very complex, and we show that it is even possible for the periodic switching behaviour to be observed for TCS.

In the final chapter of this thesis, **Chapter 7**, we give the results from two shorter and complementary studies. In the first part of the chapter we address the situation where the fields within our systems have non-equal input conditions and what effects this may have. Specifically we show that although now the system is heavily asymmetric in its origin, we may restore some typical features of the equal-input-system by a process of balancing the differences in two different input condition. In the chapter's second part we outline the derivation and early simulations of a new model which expands studies to four field components - combining the counter-propagating fields with polarisation effects. It is shown that the enlarged degrees of freedom allows for 'nested' symmetry breaking bifurcations, leading to the possibility of four asymmetric fields circulating simultaneously and thus opening new avenues for applications requiring more diversity and flexibility than just two coupled components.

We then conclude the thesis with a summary of our findings and finally provide an explanation of the numerical methods used throughout this thesis in the appendix.

"Begin at the beginning...
and go on till you come to the end:
then stop."

– Lewis Carroll, Alice in Wonderland

Chapter 2

Passive Kerr Ring Resonators

Contents

2.1 Chapter Introduction

In this main introductory chapter we aim to provide a background on passive Kerr ring resonators, of the physics involved when light propagates around them and finally the purely temporal version of the Lugiato-Lefever equation [31], which has enjoyed much success in accurately modeling the circulating light field's dynamics.

2.2 Theoretical and Physical Passive Kerr Ring Resonators

Let us begin by first discussing the theoretical schematic of a ring resonator. In its most basic definition, a ring resonator is a waveguide which forms a closed loop coupled to some input and output; an example of this is given in Fig. 2.1.
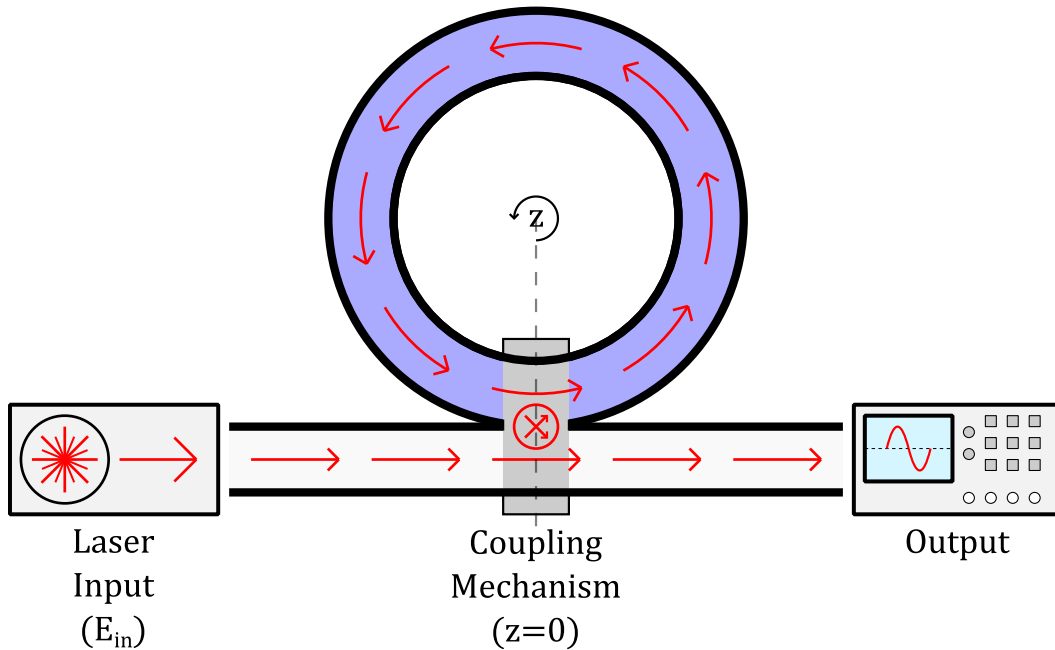
Figure 2.1: Basic setup of a ring resonator. Laser light is sent from some input along a path towards an output, with a coupling mechanism placed somewhere along the way. This coupling mechanism, with transmissivity, T, and reflectively, R, acts as a two way gate, allowing for light to both enter and leave the waveguide of the resonator, which forms a closed loop.

9

In Fig. 2.1 we have some laser input which sends light along a waveguide towards an output. At some point along the input-output path there lies a coupling mechanism of some description (such as a beam splitter, fiber coupler or evanescent-wave coupling), which allows for the input light to leave its current path and join the closed loop path of the resonator itself.

The coupling mechanism may be characterised by its power reflection coefficient, R, and its power transmission coefficient, T. These coefficients represent the respective proportions of light which is reflected (carries on without interruption towards the output) and transmitted (enters the closed loop waveguide of the resonator) by the coupling mechanism.

In this thesis we concern ourselves with high finesse, or low-loss, resonators which partially amounts to being able to state that, for the coupling mechanism of choice, $T \ll 1$. This very low rate of transmission, and conversely very high rate of reflection, acts in both directions for the coupling mechanism. This means that a very low proportion of the laser input will enter the resonator, yet once it has entered the resonator it will remain there, circulating over and over for many round trips. Eventually the light will leave the resonator, by the same coupling mechanism, to rejoin its original path and proceed on towards the output once again.

The material which makes up the resonator itself is extremely important in determining how the circulating light field is affected during its propagation. In this thesis we focus on Kerr media (described in detail momentarily), which are named as thus for their capacity in displaying the Kerr, or quadratic electro-optic (QEO), effect on propagating light [3,4]. Other types of materials can be used in the creation of ring resonators, such as a quadratic nonlinear media [34], but these are not studied here.

Physical manifestation of Fig. 2.1 can be achieved in a number of ways. Figure 2.2 shows some variations of microring resonators, such as microrod (a) or microtoroid (b) setups. Various nonlinear materials can also be used to make up the resonator, such as silica (a,b) and silicon nitride (c) [35,36]. Microring resonators, as their name suggests, are typically micrometres to millimetres in size. Similarly Fig. 2.1 may be realised using fiber-loops. For example, in Ref. [20] fiber loops made from single-mode silica fiber were used to observe temporal cavity solitons [19]. Contrary to the micrometres to millimetres size of microring resonators, these fiber cavities are often much larger: 380 m in length in Ref. [20], 10.5 m in Ref. [37] for example. The relative small size of microring resonators, in comparison to fiber loops, is of tremendous advantage when its comes to applications requiring a large free spectral range [38] or which seek to minimise the required physical space of components - such as in the generation of frequency combs for use on satellites [39].
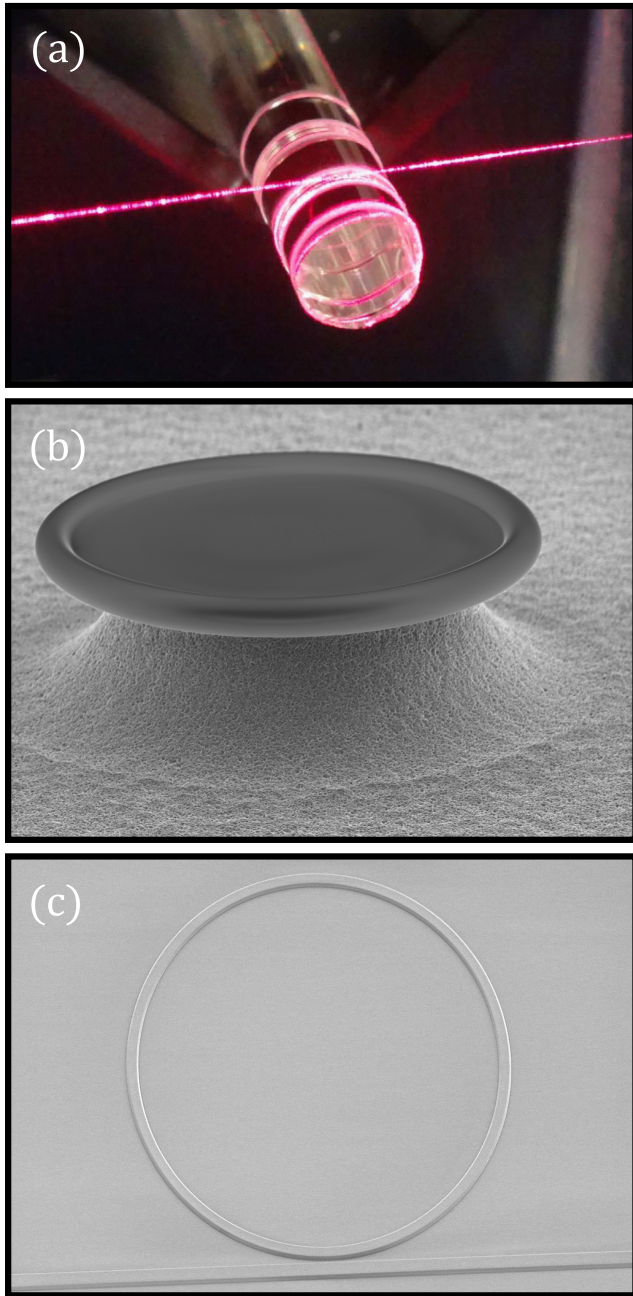
Figure 2.2: Three physical realisations of passive Kerr ring resonators. (a) shows a 2.7 mm diameter high-Q whispering-gallery-mode fused silica micro-rod resonator with a tapered fibre (highlighted with red laser light) [35]. (b) shows a silica micro-toroid resonator with diameter of approximately 200 µm. [36] Finally, (c) shows a Si_3N_4 resonator with a diameter of approximately 450 µm. [36]

2.3   Modeling Passive Kerr Ring Resonators

In this subsection we first introduce two important factors for consideration when modeling the propagation of light in Kerr materials, with the first being the Kerr nonlinearity and the second being chromatic dispersion. Following these introductions we will work through the derivation of the highly successful (purely temporal) Lugiato-Lefever equation from the Nonlinear Schrödinger equation with appropriate boundary conditions, introducing other important considerations, such as cavity detuning and other losses, as we go.

2.3.1   The Kerr Nonlinearity

Nonlinear optics in general is the study of effects whose origins lie in a material's response to an optical field, with the strength of this response depending in a nonlinear manner on the strength of said field.

The Kerr nonlinearity arises from a change in the refractive index of a material in response to an applied electric field; an effect which was discovered in 1875 by John Kerr, a Scottish physicist [3, 4], whom the effect was later named after. This nonlinearity can be observed when considering the polarisation field of a material, $P(t)$, in response to an optical field $E(t)$, described by

$$P(t) = \epsilon_0 \left[\chi^{(1)} + \chi^{(2)} E(t) + \chi^{(3)} |E(t)|^2 \right] E(t) , \qquad (2.1)$$

where ϵ_0 is the permittivity of free space, χ is the the susceptibility tensor specific to the medium, with $\chi^{(1-3)}$ being the linear, second- and third-order nonlinear optical susceptibilities respectively, and where we have stopped at the Kerr nonlinearity under the assumption that higher order terms are negligible for the materials we study here. We also assume in this thesis that the resonator materials of choice display inversion symmetry, such that $\chi^{(2)}$ vanishes [1], and further that the polarisation field in Eq. (2.1) changes instantaneously in response to the field strength.

In this manner we may express the polarisation field of the propagated material by splitting the total polarisation field into linear and nonlinear parts

$$P(t) = P_L + P_{NL} = \epsilon_0 \left[\chi^{(1)} + \chi^{(3)} |E(t)|^2 \right] E(t) , \qquad (2.2)$$

This is used later as a key component of the Nonlinear Schrödinger equation.

2.3.2 Chromatic Dispersion for Slowly Varying Envelopes

Chromatic dispersion causes an angular frequency, ω, dependence in the refractive index of a medium, $\eta(\omega)$. It often occurs during the interaction between an electromagnetic wave and the electronic cloud of a dielectric medium, such as silica. The effect amounts to implying that different spectral components of a propagating field profile, such as a pulse, will not travel at the same velocity, leading to chirping [40, 41].

We may vastly simplify discussions on chromatic dispersion if we limit ourselves to situations where we can validly make the slowly varying envelope approximation (SVEA), which amounts to assuming that the envelope of a field varies much slower, in space and time, compared to the carrier wave [42, 43], that is to say

$$\left|\frac{\partial \mathbf{E}}{\partial z}\right| \leq k_0 \left|\mathbf{E}\right| \;, \quad \left|\frac{\partial \mathbf{E}}{\partial t}\right| \leq \omega_0 \left|\mathbf{E}\right| \;. \tag{2.3}$$

When determining the influence of dispersive effects, the SVEA allows us to neglect higher-order terms in the Taylor expansion of the mode-propagation constant $k(\omega)$ around the carrier frequency, ω_0, such that it is given by

$$k(\omega) \approx k_0 + k_0'(\omega - \omega_0) + \frac{1}{2}k_0''(\omega - \omega_0)^2 \tag{2.4}$$

with

$$k_0 = k\left(\omega_0\right) \;, \quad k_0' = \frac{\partial k_0}{\partial \omega} \;, \quad k_0'' = \frac{\partial^2 k_0}{\partial \omega^2} \;, \tag{2.5}$$

where $k_0' = 1/v_g$ and k_0'' are known as the inverse of the group velocity v_g and the group velocity dispersion parameter, respectively.

Focusing on only the last two terms of Eq. (2.4) and applying the inverse Fourier transform returns

$$\mathcal{F}^{-1}\left(k_0'(\omega - \omega_0) + \frac{1}{2}k_0''(\omega - \omega_0)^2\right) = ik_0'\frac{\partial \mathbf{E}}{\partial t} - \frac{k_0''}{2}\frac{\partial^2 \mathbf{E}}{\partial t^2} \;, \tag{2.6}$$

which is used in combination with Eq. (2.2), details in Ref. [42], to derive the well known Nonlinear Schrödinger equation, Eq. (2.7).

2.3.3 The Purely Temporal Lugiato-Lefever Equation

The model which forms the basis of the more complex models later used in this thesis, and which would later be described as the purely temporal version

of the Lugiato-Lefever equation, was first derived by Halterman, Trillo and Wabnitz in their 1992 publication "Dissipative modulation instability in a nonlinear dispersive ring cavity" [44]. At its core, this model builds upon the Nonlinear Schrödinger equation [42,45], which combines the Kerr nonlinearity and chromatic dispersion by

$$\frac{\partial E_n}{\partial z} = -i\frac{k_0''}{2}\frac{\partial^2 E_n}{\partial \tau^2} + i\gamma|E_n|^2 E_n, \tag{2.7}$$

where, in the context of Fig. 2.1, $E_n(z,\tau)$ describes the envelope of the circulating field at some distance z from the coupling mechanism (placed at $z = 0$) around the resonator, on its nth round trip. τ is measured in a frame of reference traveling at the group velocity of the carrier wave, such that $\tau = t - z/v_g$ (which collapses Eq. (2.6)), and γ is the self-phase modulation coefficient (see section 5.1.1). In fibers for example, γ is given by $\gamma = \omega_0 n_2/cA_{\text{eff}}$, where n_2 is the nonlinear index coefficient of the medium, A_{eff} is the effective area of the medium's core, c is the speed of light in a vacuum and ω_0 is the central frequency of the spectrum.

Equation (2.7) is combined with the following longitudinal boundary conditions

$$E_{n+1}\left(z = 0, \tau\right) \approx \sqrt{T}E_{in} + \sqrt{R}e^{-i\theta}G_L E_n\left(z = 0, \tau\right), \quad n = 0,\ 1,\ 2,\ \dots\ , \tag{2.8}$$

which amount to stating that the field just after the coupling mechanism is equal to the transmitted input field, E_{in}, plus the intracavity field which has just propagated one round trip. Within Eq. (2.8), T, R are the transmission and reflection coefficients of the coupling mechanism respectively, with $T+R = 1$, θ is the cavity detuning (the difference between the carrier frequency, ω_0, and the closest cavity resonant frequency) and we define the operator G_L to account for the propagation of E_n through the nonlinear medium over some distance L, which here we assume to be the length of the ring resonator, i.e.

$$G_L E_n(z = 0, \tau) = \int_0^L \left(\frac{\partial E_n}{\partial z}\right)dz, \tag{2.9}$$

which amounts to the integration of the Nonlinear Schrödinger equation, Eq. (2.7) over the longitudinal range $z = (0 \to L)$.

Equations (2.7) and (2.8) together describe an infinite-dimensional Ikeda map [46] which completely describes the dynamics of the system, however under the assumption that we are dealing with high finesse (low-loss) resonators, such that $T << 1$, we can, via the following method, combine Eq. (2.7) and (2.8) into a single partial differential equation.

The limits described under the assumption of low-loss resonators imply that the length of time that a single photon may be expected to stay within the cavity, before exiting via the coupling mechanism, is very high in comparison to the roundtrip time t_R. The low entry and exit rates to the cavity of photons means that it is reasonable to assume that the intracavity field has very little variation over one round trip, known as the mean-field approximation, and hence we may perform the integration of Eq. (2.9) trivially by the first-order Euler method [19], resulting in

$$
\begin{aligned}
G_L E_n(0, \tau) = \int_0^L \left(\frac{\partial E_n}{\partial z} \right) dz, \\
\approx E_n(0, \tau) + L \frac{\partial E_n(0, \tau)}{\partial z} \\
\approx E_n(0, \tau) - iL \frac{k_0''}{2} \frac{\partial^2 E_n(0, \tau)}{\partial \tau^2} + iL\gamma |E_n(0, \tau)|^2 E_n(0, \tau).
\end{aligned}
\tag{2.10}
$$

This assumption, that the round trip variation of the field is very small, also allows to to define new temporal variable t, known as the 'slow'-time, which describes the field on each pass of the coupling mechanism at $z = 0$ such that $E(t, \tau)$ is defined as

$$
E(t = nt_R, \tau) = E_n(z = 0, \tau), \quad n = 1, 2, ...
\tag{2.11}
$$

with its derivative defined in a similar manner by

$$
\frac{\partial E(t = nt_R, \tau)}{\partial t} = \frac{E_{n+1}(z = 0, \tau) - E_n(z = 0, \tau)}{t_R}, \quad n = 1, 2, ...
\tag{2.12}
$$

Returning attention to Eq. (2.8), we proceed by making the substitutions $e^{-i\theta} \approx 1 - i\theta$ and $R = 1 - T$ to obtain

$$
\begin{aligned}
E_{n+1}(z = 0, \tau) &\approx \sqrt{T} E_{in} + \sqrt{1 - T}(1 - i\theta) G_L E_n(0, \tau) \\
&\approx \sqrt{T} E_{in} + \left[\left(1 - \frac{T}{2} \right) (1 - i\theta) \right] G_L E_n(0, \tau) \\
&\approx \sqrt{T} E_{in} + \left[1 - \frac{T}{2} - i\theta + i\frac{T\theta}{2} \right] G_L E_n(0, \tau).
\end{aligned}
\tag{2.13}
$$

By the slowly varying envelope and low-loss assumptions stated earlier, with the latter further amounting to assuming that both the cavity detuning

and self-phase modulation are small $\theta \ll 1$, $L\gamma|E| \ll 1$ [44], we may assume that T, θ and the latter two terms of Eq. (2.10) are of first order smallness and proceeding to drop higher order terms from Eq. (2.13), one arrives at

$$
\begin{aligned}
E_{n+1}\left(z=0, \tau\right) &\approx \sqrt{T} E_{in} + E_n(0, \tau) - \frac{T}{2} E_n(0, \tau) - i\theta E_n(0, \tau) \\
&\quad - iL\frac{k_0''}{2}\frac{\partial^2 E_n(0, \tau)}{\partial \tau^2} + iL\gamma|E_n(0, \tau)|^2 E_n(0, \tau) \\
&\approx \sqrt{T} E_{in} + \left(1 - \frac{T}{2} - i\theta - iL\frac{k_0''}{2}\frac{\partial^2}{\partial \tau^2} + iL\gamma|E_n(0, \tau)|^2\right) E_n(0, \tau) .
\end{aligned}
$$
(2.14)

Making use of Eq. (2.12) and (2.14) then gives the result:

$$
t_R \frac{\partial E(t, \tau)}{\partial t} \approx \sqrt{T} E_{in} + \left[-\frac{T}{2} - i\theta - iL\frac{k_0''}{2}\frac{\partial^2}{\partial \tau^2} + iL\gamma|E_n(t, \tau)|^2\right] E_n(t, \tau) ,
$$
(2.15)

which, by the following definitions

$$
\alpha = \frac{T}{2} , \quad \bar{\theta} = \frac{\theta}{\alpha} , \quad \bar{E} = \sqrt{\frac{L\gamma}{\alpha}} E , \quad \bar{E}_{in} = \sqrt{\frac{\alpha^3}{T^2 L\gamma}} E_{in} ,
$$
(2.16)

and transformations

$$
t \to \frac{t_R}{\alpha} \bar{t} , \quad \tau \to \sqrt{\frac{L\left|k_0''\right|}{2\alpha}} \bar{\tau} ,
$$
(2.17)

can be expressed in its dimensionless form as:

$$
\frac{\partial E(t, \tau)}{\partial t} = E_{in} + \left[-1 - i\theta - i\eta\frac{\partial^2}{\partial \tau^2} + i|E|^2\right] E ,
$$
(2.18)

where, for ease of notation, we have dropped all bar notation and have also introduced $\eta = \pm 1$, which depends on the sign of k_0'' and indicates normal and anomalous dispersion respectively. Note that the term α defined here generally refers to the total cavity losses studied within the system, such that, if one wishes to account for further factors, such as internal cavity loss in fibers, splice loss or intracavity component losses, these can also be included, or excluded, as required [19].

The fully temporal LLE is in fact equivalent to the spatio-temporal LLE in one dimension [19, 42]. The spatio-temporal LLE takes into account the

diffraction of the field and has its origins in the Maxwell-Bloch equations for a two-level system with assumptions introduced by the mean-field limit [31, 42]. An extension to this model that we do not consider here is the inclusion of thermal effects which may arise in micro-resonator devices . These thermal effects can lead to further changes in the refractive index of the resonator as a function of the pump power [6].

2.3.4 Solving the Lugiato-Lefever Equation

Homogeneous Stationary States and Optical Bistability

Homogeneous solutions are here defined as solutions where the circulating field, $E(t, \tau)$ remains constant during a round-trip i.e. $E(t, \tau) = E(t)$, and implies that $\partial^2 E/\partial \tau^2 = 0$ in the LLE (2.18). Stationary solutions on the other hand are here defined as solutions within which the field profile over a full round trip repeats exactly on subsequent circulations, i.e $E(t, \tau) = E(\tau)$, and defines $\partial E/\partial t = 0$ in the Eq. (2.18).

The set of homogeneous stationary solutions to the LLE (2.18) is therefore given by:

$$0 = E_{in} + \left[-1 - i\theta + i|E|^2 \right] E \; , \tag{2.19}$$

and we may multiply Eq. (2.19) by its complex conjugate and simplify to obtain the following equation

$$|E|^2 = \frac{E_{in}^2}{1 + \left(\theta - |E|^2\right)^2} \; , \tag{2.20}$$

which describes the set of homogeneous and stationary field intensities $|E|^2$ and amounts to a cubic equation of the form

$$y^3 - 2\theta y^2 + \left(1 + \theta^2\right) y = I \; , \tag{2.21}$$

where we define $y = |E|^2$ and $E_{in}^2 = I$. This equation, as shown in Fig. 2.3, may display a phenomena known as optical bistability [30, 47, 48], defined in general as a range of x-axis (here I or θ) values for which there are multiple possible y-axis values ($|E|^2$).

In Fig. 2.3 (a) the input intensity is scanned for various cavity detuning parameters. A bistability is not always seen since it is dependent on, here, the cavity detuning. The red, blue and green lines show input intensity scans for three different cavity detunings, but only the green line displays the bistability. This is because input intensity bistability of Eq. (2.20) is limited by a minimum detuning value of $\theta = \sqrt{3}$ (blue line).
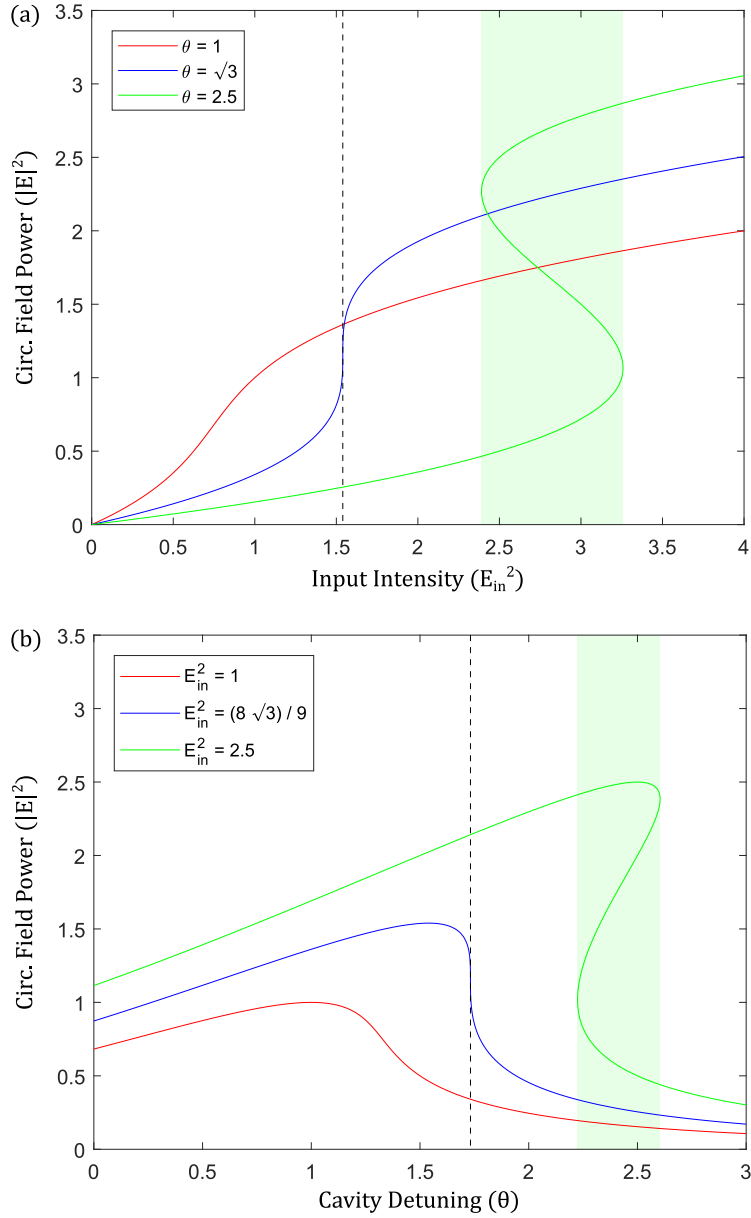
Figure 2.3: Input intensity, (a), and cavity detuning, (b), scans of Eq. (2.20) for three values of the cavity detuning, (a), or input intensity (b). In (a,b) the red line gives an example of a scan which is below the respective threshold for bistability, the blue line is a scan for the limit value where the possibility for optical bistability begins and finally the green line gives an example of a scan above the limit value, with the bistable region shaded with a green background.

18

Similarly, in Fig. 2.3 (b) the cavity detuning is scanned for various input intensity parameters. Again a bistability is not always seen since it is dependent on, now, the input intensity. The red, blue and green lines now show cavity detuning scans for three different input intensities, and again only the green line displays the bistability. This is because input cavity detuning bistability of Eq. (2.20) is limited by a minimum input intensity of $E_{in} = 8\sqrt{3}/9$ (blue).

To observe physically the effect of the nonlinearity in Eq. (2.20), we plot in Fig. 2.4 the normalised circulating field power, $|E|^2/E_{in}^2$, against the cavity detuning, θ. It can be seen that as the input intensity is increased the required cavity detuning to maximise the circulating power shifts away from 0, that is to say the nonlinearity causes a resonance shift.
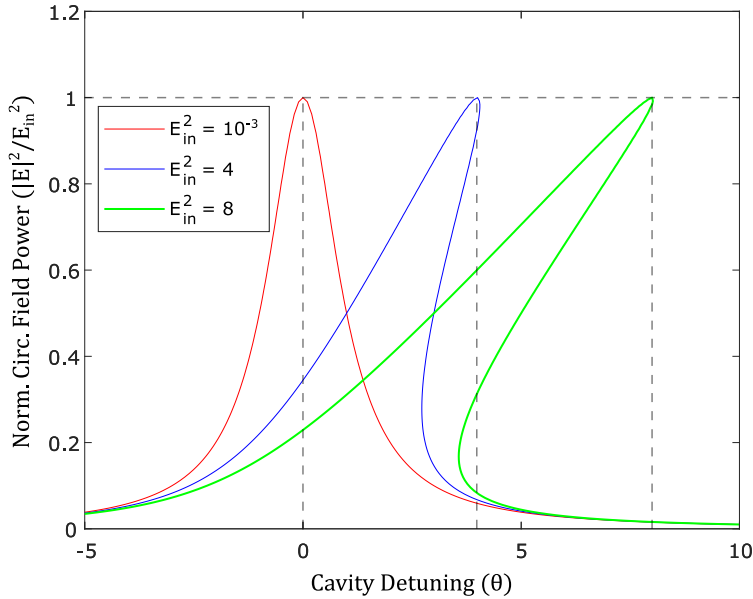
Figure 2.4: Tilted resonance curves. For various input intensities the normalised power $|E|^2/E_{in}^2$ is plotted using a recasting of Eq. (2.20). The vertical dashed lines indicate the resonant cavity detuning, θ_R, which maximises the normalised power for each given input intensity, E_{in}^2, – note how this resonant detuning is shifted away from 0 as the input intensity is increased.

Dynamical Solutions

When it comes to accessing the solutions to dynamical equations the homogeneous or stationary solutions of the system are but one aspect to consider. For example, in the system of a simple pendulum, the system state where the pendulum is perfectly inverted is a stationary state of the system. That is to say, unless the system is perturbed in some way, it will not change over time. Once such perturbations are taken into account however, even the slightest nudge to the inverted pendulum will cause it to begin to swing away from the perfectly inverted state - the state is unstable to perturbations.

The stability of a solution is thus an important indication of the dynamics of the system (where derivative components are not forced to 0). Our system can become unstable in two ways. The first occurs when $dE/dt \neq 0$ and is characterised by the emergence of Hopf bifurcations, see section 3.3 for more information. This instability amounts to the circulating field slowly varying over multiple round trips. The second occurs when $d^2E/d\tau^2 \neq 0$, which is caused by a Turing instability and leads to Turing patterns [49–51]. This type of instability amounts to the circulating field varying within a round trip.

Using an appropriate technique for integrating Eq. (2.20), such as the combination of the split-step Fourier and Runge-Kutta methods, appendix A, one can study the full dynamics of the equation and observe, for example, some of these Turing pattern states. In Fig. 2.5(a) we show again the solutions of Eq. (2.20) for a scan of the input intensity for $\theta = 1$, in the anomalous dispersion regime and with self-focusing media. The previously discussed HSS of the equation are shown in black, only now the stability of the solution is also shown, solid black - stable, dashed black - unstable. We show in (b) a possible pattern solution which occurs in the fast-time profile when the HSS becomes unstable to in-homogeneous perturbations; the blue curve in (a) tracks the maxima and minima of this pattern state.

Temporal Cavity Solitons

Connected to the pattern states of the previous section is the topic of Temporal Cavity Solitons (TCS). To avoid repeated similar content, the main discussions on TCS are left to their own dedicated chapter later in this thesis, Chapter 6, however this may suffice as a suitable place to provide a brief introduction.

To give a basic description, TCS are locally inhomogeneous solutions which propagate without changing their shape due to their ability to counter effects such as losses, and self-reinforce [19]. The reason we briefly introduce them here is due to the capacity of the LLE to sustain them through the use of
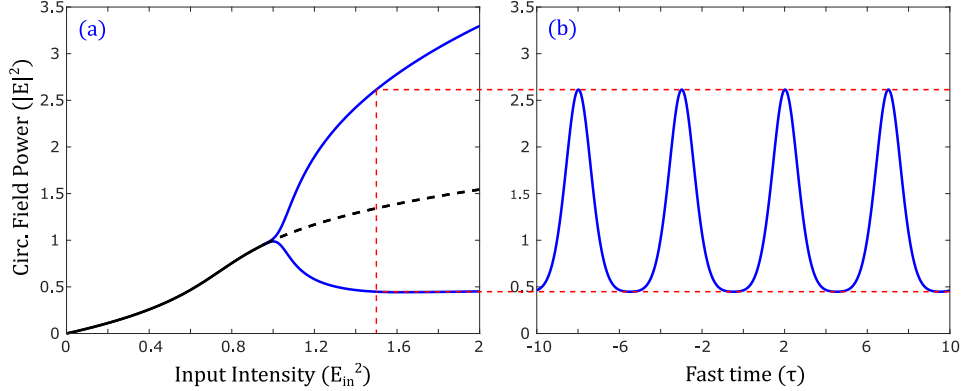
Figure 2.5: (a) An intensity scan of Eq. (2.18) for $\theta = 1$ and $\eta = -1$, with the homogeneous stationary states, given by Eq. (2.20), shown in black (solid - stable states, dashed - unstable states) and the maxima and minima of simulated pattern states shown in blue. Scan in (a) runs right to left. Note that there may be multiple possible pattern states - only one state is tracked here. (b) shows the profile of the tracked pattern state for $E_{in}^2 = 1.5$.
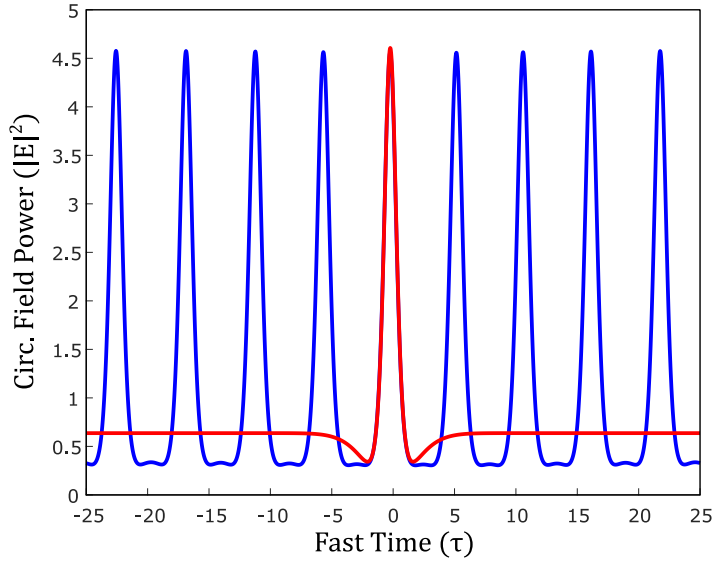
Figure 2.6: Soliton and pattern states of Eq. (2.18) for $E_{in} = \sqrt{2}$, $\theta = 2.1$ and $\eta = -1$ (anomalous dispersion). It can be seen that the TCS (red) locally locks to the pattern state (blue). The base of the TCS 'sits' on the lower branch of the HSS optical bistability.

21

pattern states. Figure 2.6 shows how the previously described Turing pattern states can provide a mechanism for the HSS to locally become inhomogeneous yet remain a stable solution.

In Fig. 2.6, the majority of the circulating field's fast time profile constitutes the HSS solution which forms the lower branch of the optical bistability however it can be seen that for a small region the profile can locally 'lock' to one of the peaks of the Turing pattern - resulting in a solitary wave or soliton.

2.4 Chapter Summary

In this preliminary chapter we strived to introduce the reader to the basic concepts surrounding light propagation in passive Kerr ring resonators. To do this we began by presenting and explaining the basic schematic of a passive Kerr ring resonator, followed up with a few examples of their physical realisation.

The next section of the chapter concerned itself primarily with the physics involved within the resonator setup, notably the Kerr nonlinearity and chromatic dispersion, and how these phenomena are modeled mathematically. By making the slowly varying envelope approximation the Kerr nonlinearity and chromatic dispersion were combined to form the well known Nonlinear Schrödinger equation.

Using the Nonlinear Schrödinger equation as a base, we proceeded to work through the derivation of the highly successful (fully temporal) Lugiato-Lefever equation (LLE). The derivation involved combining the Nonlinear Schrödinger equation with boundary conditions imposed by the resonator itself (leading to an infinite-dimensional Ikeda map), applying the mean-field approximations and neglecting high order terms.

We then went on to describe the various methods for solving the LLE. The homogeneous stationary states (HSS) of the equation could be derived exactly, and these were presented in various manners, such as input intensity and cavity detuning scans. Both scans were shown to display a phenomena known as optical bistability, which occurs when there are multiple possible states available to the system for a given scanned parameter. It was further shown how the presence of the nonlinearity in the system resulted in a resonance shift in the cavity detuning.

Finally, in this chapter we began discussions on possible dynamical solutions to the LLE, showing how it was possible for HSS to become unstable to perturbations. This instability would occur unconditionally on the middle branch of the bistability but could also occur else wear when inhomogeneous perturbations were used - leading to pattern states. It was then shown how

temporal cavity solitons could emerge within the system by locking to said pattern states while 'sitting' on the lower branch of the HSS bistability.

With the fully temporal LLE introduced, in subsequent chapters we will begin to introduce more complex models which use the LLE as their base and show how these models can display incredibly interesting and useful behaviours such as the umbrella behaviour of this thesis: the spontaneous symmetry breaking of light.

"There's nothing more exciting than science. You get all the fun of sitting still, being quiet, writing down numbers, paying attention. Science has it all."

– Seymour Skinner, The Simpsons

Chapter 3

Spontaneous Symmetry Breaking

Contents

3.1   Chapter Introduction

Most people will have some general interpretation of what is meant by symmetry and, by extension, symmetry breaking. The first explanations to a child on the subject usually involve some image printed on a piece of paper where they are shown that upon placing a mirror along some certain line, or axis, the image they see in the mirror's reflection is the same as the unaltered picture. This simple type of symmetry is known as 'reflection' (or 'mirror') symmetry.

More broadly defined, symmetry can be used to describe any common characteristic shared between two defined objects which happens to be equal, with spontaneous symmetry breaking describing the point in some parameter space at which that equality suddenly ceases to hold.

Spontaneous symmetry breaking is fundamental to the description of many physical phenomena; from the modelling of magnetism and superconductivity [52] and the generation of mass via the Higgs mechanism [53] in the case
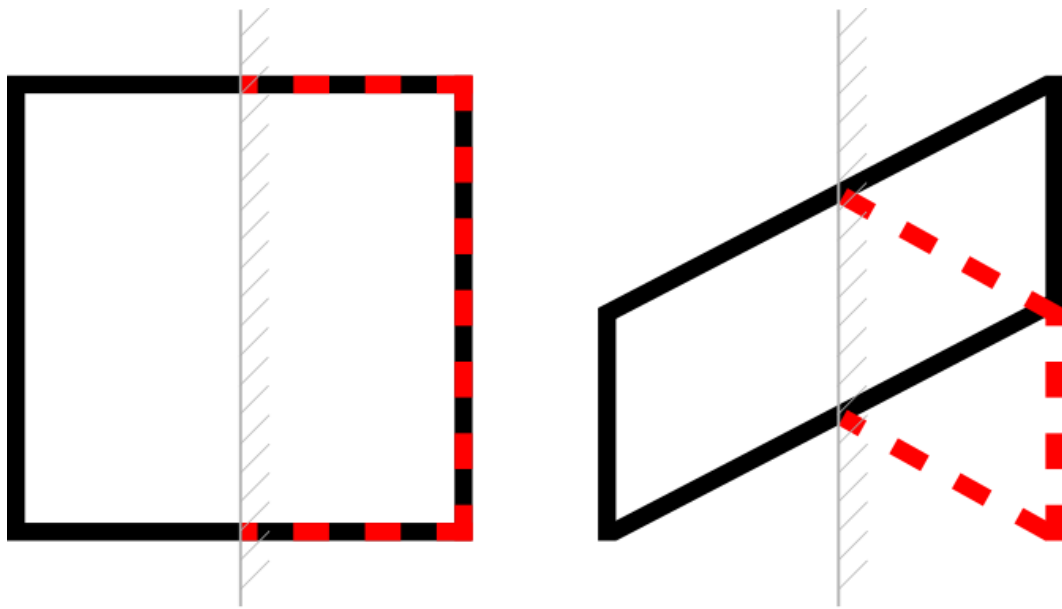
Figure 3.1: Examples of a mirror symmetry and asymmetry. Left: Placing a mirror down the central axis of a square, as illustrated by the grey line with dashing, will result in the reflection seen in the mirror appearing to overlay the non-reflected part of the square. Right: Placing a mirror again in the position of the grey line with dashing will now result in the reflection looking different to the unaltered image. Thus, in this case there is not mirror symmetry, but asymmetry.

of continuous symmetries, to many areas in optics which exhibit discrete symmetries; such as time-reversal [54,55] and parity-time symmetries [56] and the interplay between two types of symmetry breaking [57].

Spontaneous symmetry breaking has been studied recently in photonic lattices [58–60], and in spin-orbit interactions in metasurfaces [61], with chirality symmetry breaking [62] studied in metamaterials [63], during crystalisation processes [64], and in nonlinear microresonators [65]. The breaking of mirror symmetry in coupled photonic-crystal nanolasers [66] and rotational symmetry breaking in photonic spin Hall effect in dielectric metasurfaces [67] have also recently been studied. More generally, symmetry breaking has been observed in many other nonlinear systems such as in symmetric plasmonic oligomers [68], Aharonov-Bohm cages [69], double-well structures [70], and photometamaterials [71].

This chapter will describe a type of spontaneous symmetry breaking which occurs between coupled light components circulating ring resonators - a symmetry breaking which is highly applicable in communications, meteorology and integrated photonic circuits.

3.1.1   Coupled Equations

In the previous chapter it was described how a single light field component circulating a ring resonator may have its envelope described by a LLE, but what if multiple components circulate simultaneously? How do you model their interactions with each other, and does this affect the possible solutions and dynamics which are possible? This subsection will go into detail on the theoretical modelling of two situations in ring resonators: where a linearly polarised component is split into its left- and right-circularly-polarised components, and where two components circulate simultaneously counter-propagating with respect to one another.

Left- and Right-circularly-polarised Components

A linearly polarised field can be split into two components, one with its polarisation rotating in a direction to the right and the other with its polarisation rotating to the left, see Fig. 3.2. This is the first situation that we will introduce.

J. B. Geddes et al. derive in Ref. [33] what can be described as coupled LLE(s), which take into account the polarisation of a field circulating within a ring resonator. Whereas in the case of the single LLE the third-order nonlinear polarisation was given by $P^{(3)} = 3\epsilon_0 \chi^{(3)}_{1111}|E|^2E$, it is now given by
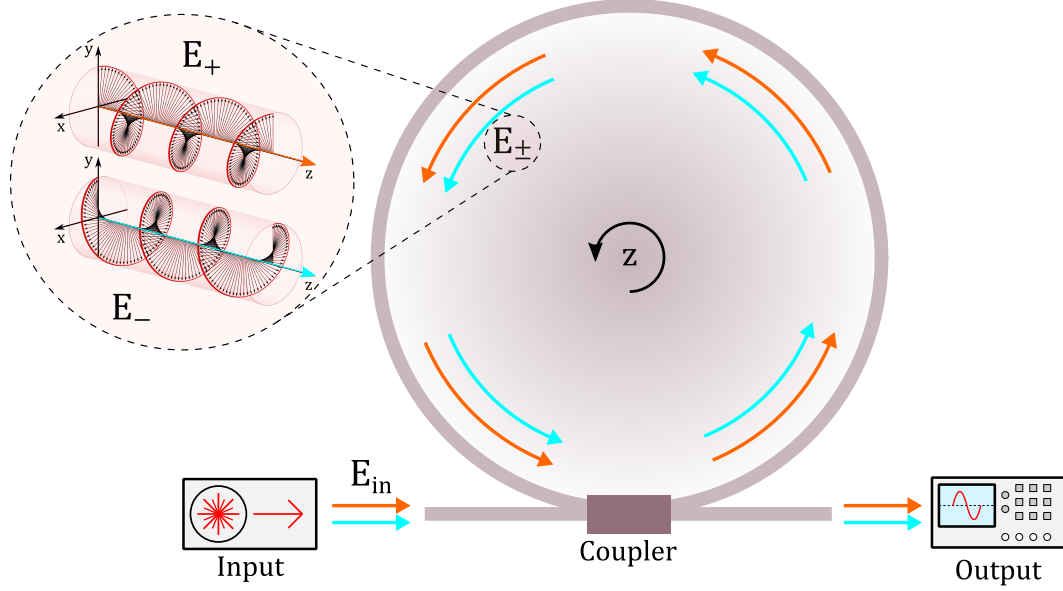
Figure 3.2: A linearly polarised field can be split into its left- and right-circularly-polarised components. This separation results in observing two, co-propagating, field envelopes circulating the resonator simultaneously.

$$\boldsymbol{P}^{(3)} = 3\epsilon_0 \chi_{1111}^{(3)} \left(A \left(\boldsymbol{E} \boldsymbol{\cdot} \boldsymbol{E}^* \right) \boldsymbol{E} + \frac{B}{2} \left(\boldsymbol{E} \boldsymbol{\cdot} \boldsymbol{E} \right) \boldsymbol{E}^* \right), \tag{3.1}$$

with

$$A = \left(\chi_{1122}^{(3)} + \chi_{1212}^{(3)} \right) / \chi_{1111}^{(3)}, \qquad B = 2\chi_{1221}^{(3)} / \chi_{1111}^{(3)} \tag{3.2}$$

where $\chi^{(3)}$ is the third order susceptibility tensor, with $\chi_{nmlj}^{(3)}$ being its elements. Applying Eq. (3.1) to the purely temporal LLE gives:

$$\frac{\partial \boldsymbol{E}}{\partial t} = \boldsymbol{E_{in}} - \boldsymbol{E} - i\theta \boldsymbol{E} - i\eta \frac{\partial^2 \boldsymbol{E}}{\partial \tau^2} + i \left(A \left(\boldsymbol{E} \boldsymbol{\cdot} \boldsymbol{E}^* \right) \boldsymbol{E} + \frac{B}{2} \left(\boldsymbol{E} \boldsymbol{\cdot} \boldsymbol{E} \right) \boldsymbol{E}^* \right) \tag{3.3}$$

where $\boldsymbol{E} = E_x \hat{\boldsymbol{x}} + E_y \hat{\boldsymbol{y}}$.

Proceeding to follow the method of Geddes et al., a transformation to a cirularly polarised basis defined by $E_{\pm} = \frac{1}{\sqrt{2}} \left(E_x \pm i E_y \right)$ is made on Eq.(3.3), which sends it to its final form:

$$\frac{\partial E_{\pm}}{\partial t} = E_{in} - E_{\pm} - i\theta E_{\pm} - i\eta \frac{\partial^2 E_{\pm}}{\partial \tau^2} + i \left(A|E_{\pm}|^2 + (A+B)|E_{\mp}|^2 \right) E_{\pm} \tag{3.4}$$

where we assume that that input field is linearly polarised along the x-direction such that $\boldsymbol{E_{in}} = \sqrt{2}E_{in}\boldsymbol{\hat{x}}$. There are many mathematical advantages of choosing this basis for study, mostly owed to removal of the complex conjugate term within the nonlinearity of Eq. (3.3). This ensures a simple method of calculating the homogeneous stationary states of the system and their stability, both discussed momentarily.

Eq. (3.4) should be readily identifiable as being of the same form as two standard LLEs, up to the inclusion of the second field within the nonlinearity. The constants A and $(A+B)$ are known as the self- and cross-phase modulation constants respectively and loosely they describe how strongly the two fields interact with each other. The exact values that these constants can take and a more in-depth explanation of their physical meaning will be left to Chapter 5 to describe.

Counter-propagating Fields

Turning our attention to the second situation for study; in the previous setup there is one input beam which enters the resonator in a set direction and proceeds to circulate, again, in one set direction. If two input beams are used however, two fields counter-propagating within the resonator can be easily achieved – one circulating in a 'forward' direction and one in a 'backwards' direction, see Fig. 3.3.

This system was first studied theoretically in the 1980s by A. E. Kaplan, P. Meystre and others [14, 32, 72]. Here they modelled the total field at some position z within the resonator as $E(z) = E_+(z)e^{ikz} + E_-(z)e^{-ikz}$ where $E_\pm$ are the envelopes of the fields circulating in the clockwise or anticlockwise directions respectively. Similar to the polarisation model, this additional field has an effect on the nonlinearity which becomes dependent upon the direction being observed. The nonlinear terms $P^{(3)}$ for each field respectively are given by

$$P^{(3)} = \gamma_2(|E_\pm|^2 + 2|E_\mp|^2).$$ (3.5)

where γ_2 describes the strength of the nonlinear susceptibility.

Utilising Eq. (3.5), steady state equations describing the envelope amplitudes of the two counter-propagating fields are given in Ref. [14, 32], which may be normalised to:

$$E_\pm = \frac{E_{in}}{1 + i(|E_\pm|^2 + 2|E_\mp|^2 - \theta)} \ .$$ (3.6)
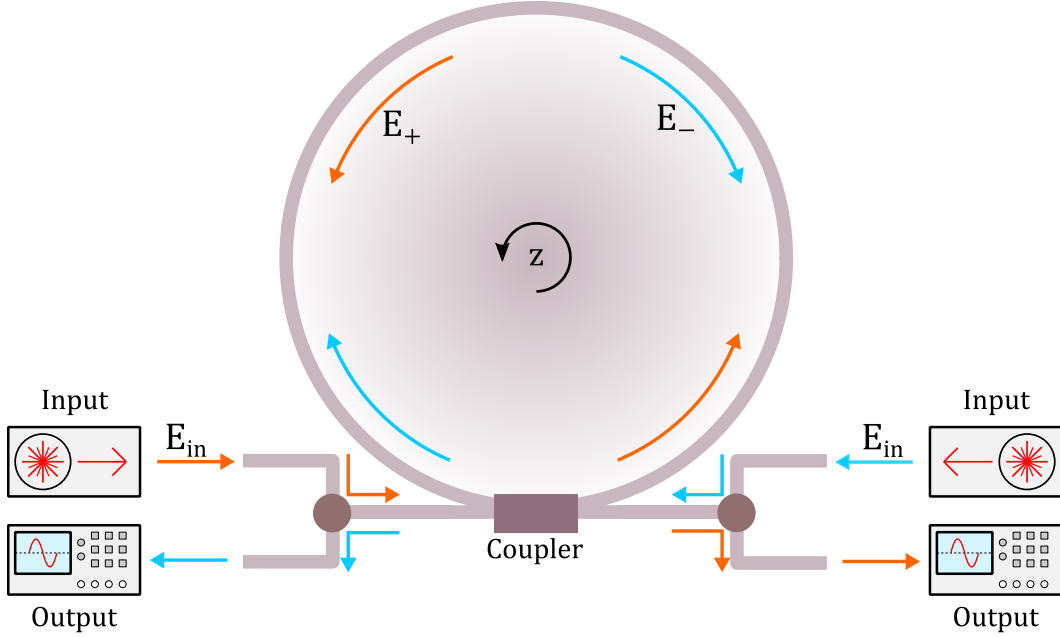
Figure 3.3: Counter-propagating fields circulating a ring resonator. Two identical input beams enter the resonator in opposing directions. Both beams circulate simultaneously but in counter-propagating directions.

3.1.2   Homogeneous Stationary States

Returning momentarily to the polarisation system and subjecting the field envelopes $E_\pm$ in Eq. (3.4) to the constraints of being both stationary and homogeneous, and multiplying by respective complex conjugates yields the steady state equation for the intensities of the envelopes of the coupled field components:

$$P_{1,2} = \frac{I}{1 + (\theta - AP_{1,2} - (A+B)P_{2,1})^2}, \tag{3.7}$$

which corresponds to two coupled Lorentzian equations, with $P_{1,2} = |E_\pm|^2$ and $I = E_{in}^2$ denoting the field envelope intensities and input intensity respectively.

Similarly for Eq. (3.6), multiplying by complex conjugates one obtains

$$P_{1,2} = \frac{I}{1 + (\theta - P_{1,2} - 2P_{2,1})^2} \ , \tag{3.8}$$

where now $I = E_{in}^2$ is the intensity of the two input pumps, one in each direction. Note that although the inputs act in opposite directions, they are

otherwise identical. This equation should be easily recognised as being in the exact same mathematical form, up until the self- and cross-phase modulation constants, as Eq. (3.7). This is an extremely important observation since it means that although the polarisation system and the counter-propagating system are physically very different, mathematically the homogeneous stationary states (HSS) are described by the same type of equations. For the rest of this section therefore we focus on the following general equation which should be understood to be applicable to both separate systems:

$$P_{1,2} = \frac{I}{1 + (\theta - AP_{1,2} - BP_{2,1})^2} \ . \tag{3.9}$$

where A and B are now new dummy variables representing the self- and cross-phase modulation constants respectively.

3.2 Spontaneous Symmetry Breaking

With much of the preamble now complete, finally the first discussions of symmetry breaking within ring resonators can begin. Our focus for now remains with the HSS equations, Eq. (3.9) and how these can be manipulated to show symmetry breaking in various ways. The easiest way, of four that we discuss here, to visualise symmetric and asymmetric solutions is by solving a variation of Eq. (3.9) with one field intensity, P_2, plotted against the other, P_1.

Method 1: A Simple Bubble
  Since Eq. (3.9) can be expressed as

$$
\begin{aligned}
I &= \left[1 + (\theta - AP_1 - BP_2)^2\right] P_1 \\
  &= \left[1 + (\theta - AP_2 - BP_1)^2\right] P_2,
\end{aligned}
\tag{3.10}
$$

one can solve these equations simultaneously, by eliminating I to obtain:

$$\left[1 + (\theta - AP_1 - BP_2)^2\right] P_1 = \left[1 + (\theta - AP_2 - BP_1)^2\right] P_2, \tag{3.11}$$

which, for $A = 1$, $B = 2$ and $\theta = 2$, is plotted in Fig. 3.4a.
  These plots can be interpreted as a simultaneous mapping of the stationary solutions of P_1 and P_2 for variations in the value of I and some constant detuning value θ. They may be considered to be the simplest way of visualising symmetric and asymmetric solutions since the solutions where $P_1 = P_2$, the

symmetric solutions, form a very obvious diagonal line with the asymmetric solutions forming an intercepting ellipse.

The points at which the asymmetric solutions occur indicate that a spontaneous symmetry breaking is possible, but whether this physically occurs, or not, is down to the stability of the system - which is left to Section 3.3.

Method 2: "The Stingray"

While the above method generates an input intensity mapping, it is also possible to obverse the circulating intensities' variation with the other independent input variable, the cavity detuning. These maps again utilise Eq. (3.9), but now one proceeds to eliminate the cavity detuning. Rearranging Eq. (3.9) one may obtain:
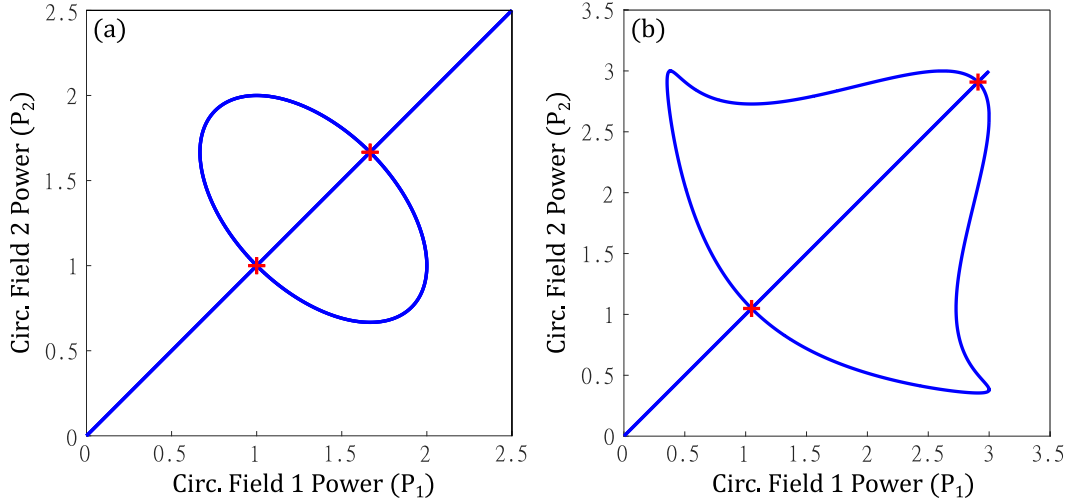
Figure 3.4: Spontaneous symmetry breaking of coupled powers P_1 and P_2. (a), the solution sets of Eq. (3.11) for $A = 1$, $B = 2$ and $\theta = 2$. Note the symmetric solutions, where $P_1 = P_2$, form an infinite diagonal line, while the asymmetric solutions form an ellipse which crosses this diagonal line in two places, or bifurcation points (red crosses). (b), the solution sets of Eq. (3.13) for $A = 1$, $B = 2$ and $I = 3$. Note the now finite diagonal line holding the symmetric solutions and how the asymmetric solutions takes the form similar to that of a stingray. The fins of the stingray shape imply a bistability is possible within the asymmetric curve itself.

$$\theta = +AP_{1,2} + BP_{2,1} \pm \sqrt{\frac{I}{P_{1,2}} - 1}$$
$$= AP_{2,1} + BP_{1,2} \pm \sqrt{\frac{I}{P_{2,1}} - 1}. \tag{3.12}$$

Which can then be solved for θ:

$$AP_{1,2} + BP_{2,1} \pm \sqrt{\frac{I}{P_{1,2}} - 1} = AP_{2,1} + BP_{1,2} \pm \sqrt{\frac{I}{P_{2,1}} - 1} \tag{3.13}$$

A plot of this equation, for $A = 1$, $B = 2$ and $I = 3$, can be seen in Fig. 3.4b. The symmetric solutions can be seen as a finite diagonal line while, for intensities above a threshold required for symmetry breaking, the asymmetric bubble forms a warped ellipse. Interesting above a second threshold the bubble bends back on itself, showing a bistability, to form a shape similar to a stingray.

Method 3: True Intensity and Detuning Scans

While the plots produced under methods 1 and 2 can be described as maps showing the effects of varying the input intensity and cavity detuning respectively, to obtain scans of these variables closer to experiments it is required to plot the independent variable along the horizontal axis, with the stationary states of the circulating field powers along the vertical axis. To do this requires much more complex equations than those given above, but it also highlights that the simplicity of the symmetry breakings shown in Fig. 3.4(a,b) hide many of the interesting results underlying within the system.

In order to plot either the input intensity or cavity detuning along the x-axis the objective is to once again eliminate one of the variables from Eq. (3.9), but rather than choosing one of the independent variables, the elimination of a dependent variable is sought, P_1 or P_2.

Taking one equation of Eq. (3.9) and rearranging to make P_1 or P_2 the subject yields:

$$P_{1,2} = \frac{AP_{2,1} - \theta \pm \sqrt{\frac{I}{P_{2,1}} - 1}}{-B}, \tag{3.14}$$

which in turn can be substituted into the remaining equation of Eq. (3.9), giving:
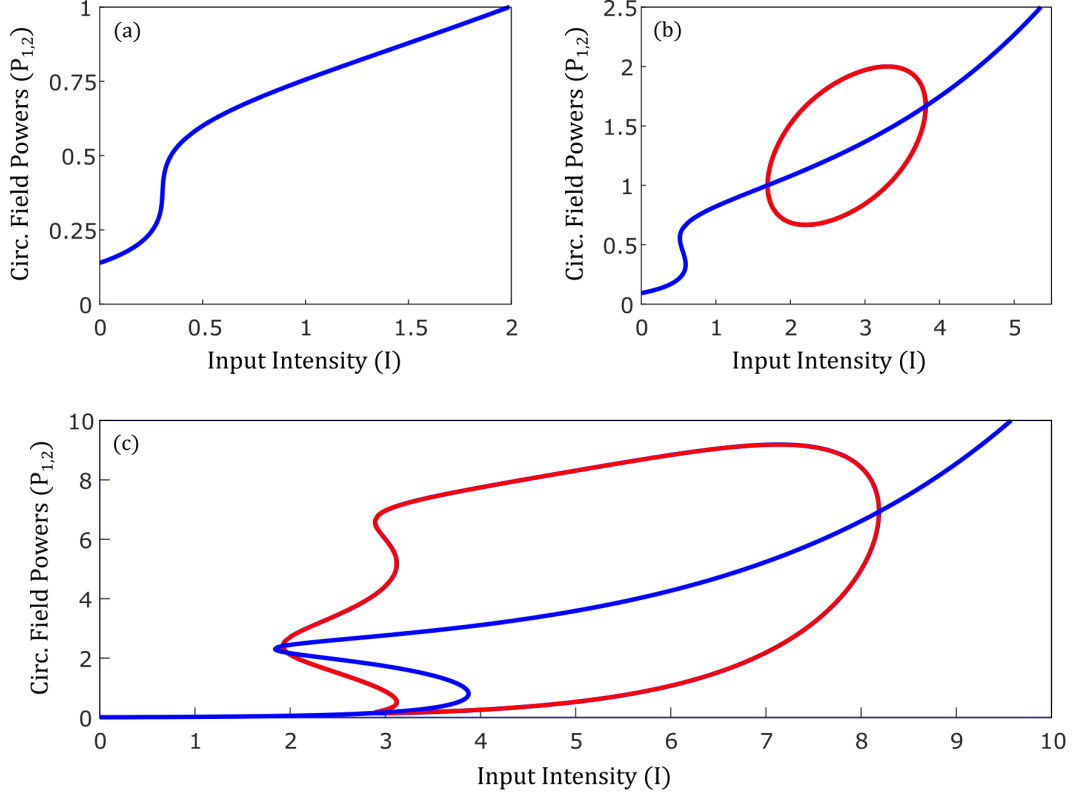
Figure 3.5: Intensity scans for low and high values of the cavity detuning. (a) for $A = 1$, $B = 2$ and $\theta = 1.7$ – with this sub-threshold detuning neither the bistability of the symmetric solution line, or asymmetric solutions are possible, there is no spontaneous symmetry breaking. (b) for $A = 1$, $B = 2$ and $\theta = 2$ we are now above the threshold for symmetry breaking, with asymmetric solutions shown in red. (c) for $A = 1$, $B = 2$ and $\theta = 7$. For this well-above-threshold value of the input intensity one can see that the asymmetric solution bubble folds in on itself, creating a bistability in the asymmetric powers.

$$\frac{AP_{1,2} - \theta \pm \sqrt{\frac{I}{P_{1,2}} - 1}}{-B} = \frac{I}{1 + \left[\theta - A\left(\frac{AP_{1,2} - \theta \pm \sqrt{\frac{I}{P_{1,2}} - 1}}{-B}\right) - BP_{1,2}\right]^2}. \quad (3.15)$$

This equation is then readily usable to produce the required scans of either the cavity detuning or the input intensity.

The solution set of Eq. (3.15) for $A = 1$ and $B = 2$ is shown in Fig. 3.5 with the circulating intensities, $P_{1,2}$ plotted against the input intensity, I, for
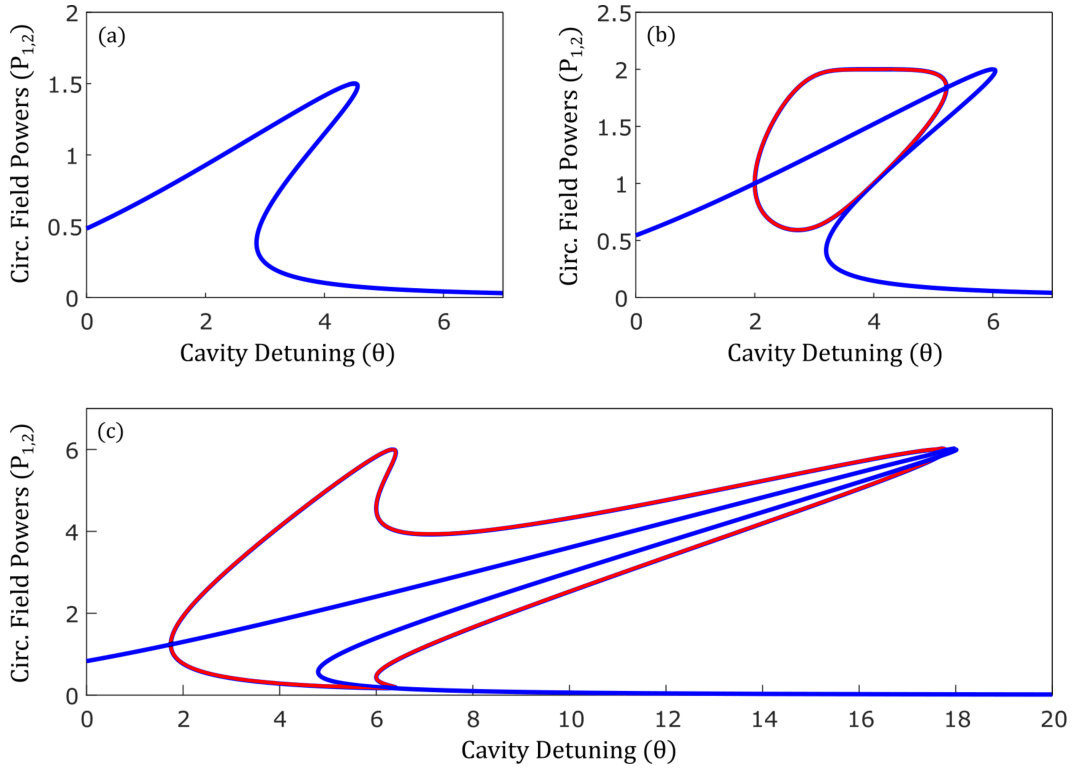
Figure 3.6: Detuning scans for various values of the input intensity. (a): $A = 1$, $B = 2$ and $I = 1.5$. This input intensity is below the threshold for asymmetric solutions, but there is a bistability on the symmetric solution line. (b): $A = 1$, $B = 2$ and $I = 2$. This input is above the threshold for both symmetric solution bistability and symmetry breaking, with asymmetric solutions shown in red. (c): $A = 1$, $B = 2$ and $I = 6$. For this well-above-threshold value of input intensity one can see that the asymmetric solution bubble (red) folds in on itself, creating a bistability in the symmetry broken powers.

various values of the cavity detuning. This reveals the true complexity, and interest, of the system described by Eq. (3.9). The symmetric solution line now takes on, what often appears to be, an elongated 'S' shape, Fig. 3.5 (a), while the asymmetric 'bubble' forms a slightly warped ellipse, Fig. 3.5 (b). As with the emergence of asymmetric solutions in Fig. 3.4 (a), the asymmetric solution bubble, and s-shaped bistability are reliant on the cavity detuning being above some limit value, i.e. note no asymmetry for Fig. 3.5 (a). Above a second detuning limit the asymmetric bubble can fold in on itself, creating a further region of bistability only this time in the asymmetric solution set, see Fig.3.5(c).

Equation (3.15) is also usable to yield a scan of the cavity detuning, where the coupled powers are now plotted against the detuning along the x-axis. Figure 3.6 shows Eq. (3.15) for a variety of input intensities. Panel (a) shows a scan for an input intensity which is below the threshold for symmetry breaking, and shows only the symmetric tilted Lorentzian solution line. The scan for an increased input intensity, this time one above the threshold for symmetry breaking, is shown in panel (b). One should be able to note the asymmetric bubble which appears on the upper path of the symmetric solution line. Increasing the input intensity further causes the folding-over of the bubble to occur once more, showing a bistability of the asymmetric solutions.

3.3 Time-dependent Model and its Stability Analysis

Returning focus momentarily to only the system of two counter-propagating fields, in Ref. [73] we described the time-dependent coupled equations which return the coupled Lorentzians of Eq.(3.6):

$$\frac{\partial E_\pm}{\partial t} = E_{in} - \left[1 + i(|E_\pm|^2 + 2|E_\mp|^2 - \theta)\right]E_\pm, \qquad (3.16)$$

where the introduced time variable t has been normalised by the photon lifetime in the cavity.

Small perturbations on the field envelopes, $E_\pm$, were then used to assess the stability of the system. By defining $E_+ = E_{+S} + \epsilon_1$ and $E_- = E_{-S} + \epsilon_2$, where $\epsilon_{1,2}$ were the small perturbations on the steady-state solutions, $E_{\pm S}$, Eq. (3.16) becomes:

$$\frac{\partial E_\pm}{\partial t} = E_{in} - \left[1 + i(|E_{\pm S} + \epsilon_{1,2}|^2 + 2|E_{\mp S} + \epsilon_{2,1}|^2 - \theta)\right](E_{\pm S} + \epsilon_{1,2}). \quad (3.17)$$

The steady state solutions, $E_{\pm S}$, occur when $\partial E_\pm/\partial t = 0$ hence Eq. (3.16) may be used to find the following expression of E_{in}

$$E_{in} = \left[1 + i(|E_{\pm S}|^2 + 2|E_{\mp S}|^2 - \theta)\right]E_{\pm S}. \qquad (3.18)$$

Inserting Eq. (3.18) into Eq. (3.17), expanding the resultant and simplifying then yields the following set of coupled equations

$$\frac{\partial E_\pm}{\partial t} = \frac{\partial \epsilon_{1,2}}{\partial t} = -[1 + i(2|E_{\pm S}|^2 + 2|E_{\mp S}|^2 - \theta)]\epsilon_{1,2}$$
$$- iE_{\pm S}^2\epsilon_{1,2}^* - 2iE_{\pm S}E_{\mp S}\epsilon_{2,1}^* - 2iE_{\pm S}E_{\mp S}^*\epsilon_{2,1}. \qquad (3.19)$$

Without loss of generality, the phase of the input E_{in} was adjusted such that $E_{\pm S}$ were real which then allows us to split $\epsilon_{1,2}$ into real and complex components, $x_{1,2}$ and $y_{1,2}$ respectively, such that $\epsilon_{1,2} = x_{1,2} + iy_{1,2}$

$$\frac{\partial(x_{1,2} + iy_{1,2})}{\partial t} = -[1 + i(2E_{\pm S}^2 + 2E_{\mp S}^2 - \theta)](x_{1,2} + iy_{1,2}) - iE_{\pm S}^2(x_{1,2} - iy_{1,2})$$
$$- 2iE_{\pm S}E_{\mp S}(x_{2,1} - iy_{2,1}) - 2iE_{\pm S}E_{\mp S}^*(x_{2,1} + iy_{2,1}).$$
$$(3.20)$$

which, expanded and simplified, is equivalent to the following:

$$\frac{\partial}{\partial t}\begin{pmatrix} x_1 \\ y_1 \\ x_2 \\ y_2 \end{pmatrix} = \begin{pmatrix} -1 & A_1 & 0 & 0 \\ -B_1 & -1 & -C & 0 \\ 0 & 0 & -1 & A_2 \\ -C & 0 & -B_2 & -1 \end{pmatrix}\begin{pmatrix} x_1 \\ y_1 \\ x_2 \\ y_2 \end{pmatrix} = \mathbf{J}\begin{pmatrix} x_1 \\ y_1 \\ x_2 \\ y_2 \end{pmatrix} \qquad (3.21)$$

with

$$A_{1,2} = E_{\pm S}^2 + 2E_{\mp S}^2 - \theta,$$
$$B_{1,2} = 3E_{\pm S}^2 + 2E_{\mp S}^2 - \theta, \qquad (3.22)$$
$$C = 4E_{+S}E_{-S}.$$

The eigenvalues of $\mathbf{J}$, calculated by solving $\det|\mathbf{J} - \lambda\mathbf{1}| = 0$, where $\mathbf{1}$ is the identity matrix, are given by:

$$\lambda_{1\to4} = -1 \pm \sqrt{\frac{-A_1B_1 - A_2B_2 \pm S}{2}}, \qquad (3.23)$$

with

$$S = \sqrt{(A_1B_1 - A_2B_2)^2 + 4A_1A_2C^2}, \qquad (3.24)$$

where the $\pm$ signs are independent, giving four distinct eigenvalues, $\lambda_{1\to4}$. These eigenvalues then define the stability of the system state. If ALL the eigenvalues have a negative real part then the system will decay to the stationary state; the state is thus defined as 'stable'. If any of the eigenvalues have a positive real part then the system will immediately evolve away from the stationary state; the state is defined as being 'unstable'. If there is a complex component to the eigenvalue then the system is susceptible to either growing or decaying oscillations, depending on the value of the real component, during its evolution. A summary of how the eigenvalues of a linear stability analysis give insight into the response of a system to small perturbations is given in

Eigenvalue Condition	Stability Implication
All real components are negative	Stable
At least one real component is positive	Unstable
At least one real component is positive and this eigenvalue has an imaginary component	Unstable to oscillations

Table 3.1: Stability conditions based upon the eigenvalues of a linear stability analysis. The onset of instability to oscillations is known as a Hopf bifurcation.
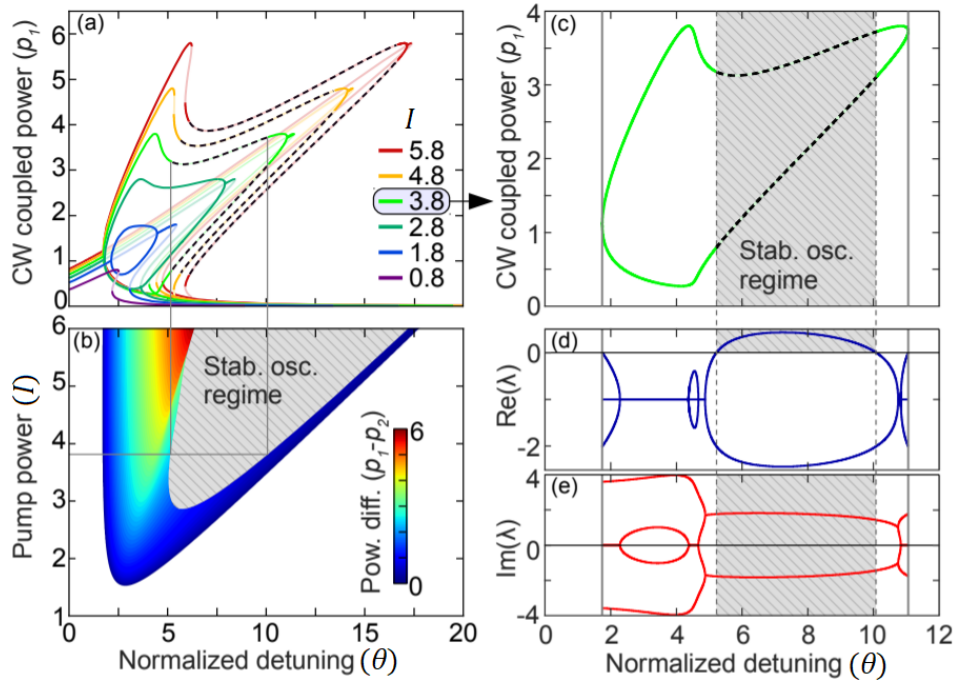
Figure 3.7: (a) Tilted resonances for various pump powers, showing the symmetry-broken region. Dark solid curves indicate stable solutions, faint curves show unstable solutions, and dashed curves correspond to oscillatory behaviour. (b) Amplitude of the difference in the coupled powers. The grey area corresponds to time-oscillating solutions (white denotes symmetric states). (c) Isolated asymmetric solution curve for I = 3.8, from (a). (d) Real part of the stability eigenvalue, λ, of (c). (e) Imaginary part of the stability eigenvalue of (c). Note that there always exists at least one eigenvalue with non-zero imaginary part, implying strong susceptibility to oscillations.

table 3.1. Figure 3.7 shows the eigenvalues, $\lambda_{1 \to 4}$, and conditions being used to calculate the local stability of Eq. (3.6) for detuning scans at various input intensities.

The first result here worthy of discussion is the verification of a claim made in Ref. [32]; that part of the symmetric solution line which exists between the symmetry breaking and restoring bifurcation points is unstable. This is a very important result since it means that in an imperfect version of the system, one which contains random noise, where possible the two fields will evolve over time away from the symmetric solution line towards the asymmetric solution line - one field will become dominant while the second field is suppressed, explaining the some experimental observations of Refs [35, 37].

Figure 3.7(a) shows the detuning scans of Eq. (3.9) for $A = 1$, $B = 2$ and for various input intensities. It can be seen that there exists a critical value of the input pump for the system to be susceptible to oscillations, this value was calculated to be $I = 2.87$. Panel (b) shows the difference between the two asymmetric fields and panels (c-e) show the eigenvalue analysis for a selected intensity of $I = 3.8$. (c) shows the isolated asymmetric bubble with panels (d) and (e) showing the calculated eigenvalues of these asymmetric coupled powers. Recalling table 3.1, for the majority of the values shown for the normalised cavity detuning the real part of the eigenvalues is negative, i.e $\mathrm{Re}\left(\lambda_{1 \to 4}\right) < 0$, implying that the asymmetric solutions are stable. However, this is not true for all detuning values. Note in Fig. 3.7(d) that between detuning values of approx. 4.5 and 10 the real part of two of the eigenvalues is greater than 0, implying that even the asymmetric solutions in this region are unstable. There also exist imaginary components to these eigenvalues implying the solutions are unstable to growing oscillations. These oscillations will be studied in subsequent chapters.

3.4   Chapter Summary

In this chapter the coupled Lorentzian equations, Eq. (3.9), which form the homogeneous stationary states of two different nonlinear optical systems were introduced. Both systems at their core involve the propagation of light in Kerr ring resonators, but while in the first system one input beam is used to induce two circularly polarised co-propagating light components, in the second two input beams are used, which in turn leads to two counter-propagating light fields circulating within the resonator.

It was shown how the two coupled Lorentzian equations can exhibit a spontaneous symmetry breaking, and restoration, in the intensities of the two circulating components for a multitude of variable scans provided one is operating in a specific region of the input pump and cavity detuning parameter space.

Restoring a temporal derivative to the Lorentzian system, Eq. (3.16), a stability analysis of the system was completed and this confirmed that the asymmetric solutions which become possible following the system symmetry breaking are dynamically favoured over the unstable symmetric solution. The stability analysis also revealed that within some regions of the parameter space even the asymmetric solutions can also become unstable, unstable to growing oscillations.

———————————————————

——————————————————————

———————————————————

*"Absorb what is useful, discard what is useless
and add what is specifically your own"*

– Bruce Lee

Chapter 4

Simple and Complex Oscillations; Chaotic and Periodic Self-switching Dynamics

Contents

4.1   Introduction

The Logistic map [74], Eq.(4.1), is often used as an example of how simple
nonlinear dynamical equations can lead to very complex behaviours. This
mapping is mathematically expressed by:

$$x_{n+1} = rx_n \left(1 - x_n\right), \tag{4.1}$$

where $0 < x_n < 1$, which originally described the ratio of some existing popula-
tion to the maximum possible population, and, to ensure nontrivial solutions,
$1 < r < 4$. By seeking the fixed points of Eq.(4.1), where $x_{n+1} = x_n$, it is
possible to build up a diagram of the successive iterations in finding these fixed
points against the value of r, Fig. 4.1. It can be seen on such a diagram how
initially the employed algorithm successfully finds a fixed point however, at
$r = 3$, successive iterations begin to alternate between two non-fixed points,
further increases of r lead to successive iterations alternating between now 4
non-fixed points. The number of points which successive iterations cyclically
alternate between increases further with r leading, eventually, to resemble
chaos. The values of r at which the number of alternating points change are
know as bifurcations, $r = 3$ for example is known as a bifurcation point, and
hence Fig. 4.1 is often referred to as a bifurcation diagram.
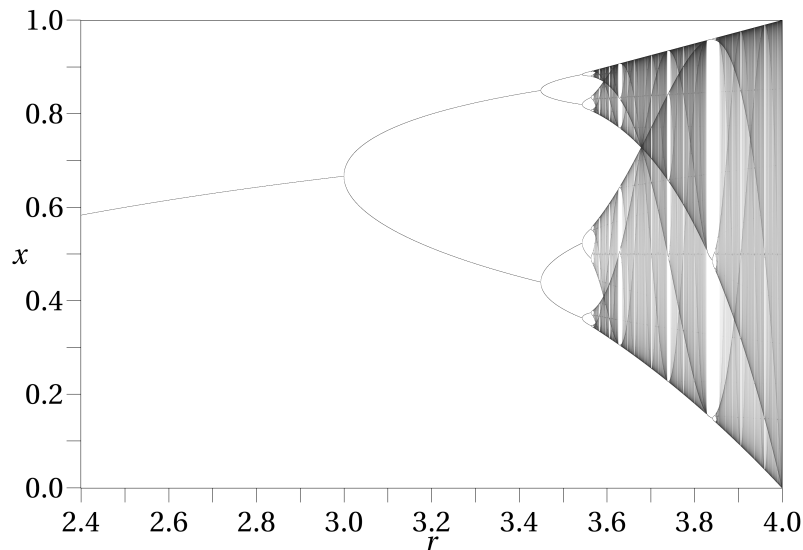
Figure 4.1: Bifurcation diagram of the late iterations of seeking the fixed
points, where $x_{n+1} = x_n$, for Eq.(4.1) against the value of r. *Image taken from
the public domain* [75]

The previous chapter's prediction, that the system of coupled equations (3.16) describing the counter-propagating setup was locally susceptible to oscillations, prompted the dynamics of the system to be explored in more depth. This study was spurred on since oscillations due to the Kerr nonlinearity have been previously noted to occur in other systems of microcavities, including those with multiple coupled resonators [76–78], in a single resonator due to: linear coupling which is achieved between the two cavity modes via Rayleigh backscattering [79], thermal instabilities [80] and external forcing [81]. In this chapter we specifically report on how the growth of the predicted local oscillations is eventually suppressed and how the dynamics of the resulting oscillations can become extremely complex and may even lead to apparent chaos and the interesting dynamic of self-switching.

In addition to passive systems, the results of this chapter may be of consequence for the gain dynamics of ring lasers [82,83], and for systems that host Kerr solitons [84–88] especially those with counterpropagating modes [89].

From a practical perspective, self-switching periodicity of the counterpropagating modes can be applied in the controlled generation of twin waveforms and signal encoding, while the chaotic states that we imminently report could be potentially be employed in the generation of chaotic-cryptographic algorithms [90] as well as chaos-induced stochastic resonance [91].

In photonics, noisy [92] and chaotic [93] switching between two polarization states, as well as in-phase and antiphase frequency combs [94], have been described in semiconductor lasers. Recently, similar effects have also been described in the simulation of driven dissipative dimers of Bose-Einstein condensates [95].

4.2 Simple Temporal Evolutions and Oscillations

As mentioned in Chapter 3, the onset of the system of Eq. (3.16) becoming susceptible to growing oscillations (a Holf bifurcation) is described by the set of eigenvalues, $\lambda_{1 \to 4}$, Eq. (3.23), where for at least one eigenvalue, λ, $\mathbb{R}(\lambda) > 0$ and $Im(\lambda) \neq 0$. However, this eigenvalue analysis only describes the local susceptibility of the state to said oscillations. To obtain the full picture of the resulting temporal dynamics one must complete direct numerical integrations of Eq. (3.16). In this instance this was completed using the Runge-Kutta method of integration, as outlined in the appendix on numerical methods.

Early results of the numerical integrations of the system of Eq. (3.16), with $A = 1$, $B = 2$, $I = 3.8$ and initial conditions $E_+ = 2.0000 + 0i$ and

$E_- = 2.0001 + 0i$, are displayed in Fig. 4.2. The imposed 0.0001 difference
in the initial conditions and programmed random noise at each iteration is
to create a very small imbalance in the two fields and avoid the situation of
Buridan's principle [96]. This figure is complementary to the depiction of the
eigenvalue analysis for this system in Fig. 3.7.

The first two panels of Fig. 4.2, (a)-(b), occur with $\theta = 1.5$, where for all
eigenvalues of the stationary symmetric solution $\mathbb{R}(\lambda) < 0$, i.e the condition
for it being stable is satisfied, and further the detuning value is below the
$\sqrt{3}$ requirement for symmetry breaking to occur. In (a), one can see how the
system therefore spirals away from the initial conditions onto the attractor
of the stable stationary solution. This can be seen also in (b) as the system
relaxes to a stable, symmetric, intensity.

In panels (c)-(d) $\theta = 5$. This higher detuning value now allows for at least
one eigenvalue of the symmetric stationary state to have a real component
greater than 0, i.e the state is unstable. This detuning value however is also
above the threshold for symmetry breaking, see Fig. 3.7 (c). Fig. 4.2 (c)
shows how the system once again evolves away from the initial conditions to
the initially attractive symmetric solution, however, as is expected since this
solution is unstable, upon the system getting suitably close to the symmetric
attractor, the system rapidly jumps away, before spiraling in on the two stable
attractors of the asymmetric stationary state. This can also be seen in (d)
where the two fields' intensities initially evolve together before separating into
two unequal constant intensities.

Finally, in panels (e)-(f), there is an example of how the system evolves
in the parameter space where both the symmetric and asymmetric stationary
states are unstable. Here $\theta = 5.5$, and one can observe in (e) how the system
again spirals towards the unstable symmetric attractor before jumping away, as
before, to spiral towards the asymmetric attractors, however this time, rather
than crashing in on the asymmetric stationary state, as in (c), the system
now settles to periodically orbit around the two asymmetric states, leading
to a sinusoidal variation in the two circulating intensities (f), with a single
characteristic frequency.

It may be odd to note that the system's oscillations in Fig. 4.2(e,f) eventu-
ally stop growing and become regular. The prediction of growing oscillations
made by the linear stability analysis only holds true for a small area surround-
ing the stationary solution, when the oscillations become so large that they
fall out of this region of validity other effects can occur. I.e. the system can
become saturated, imposing a limit on the magnitude of the oscillations.
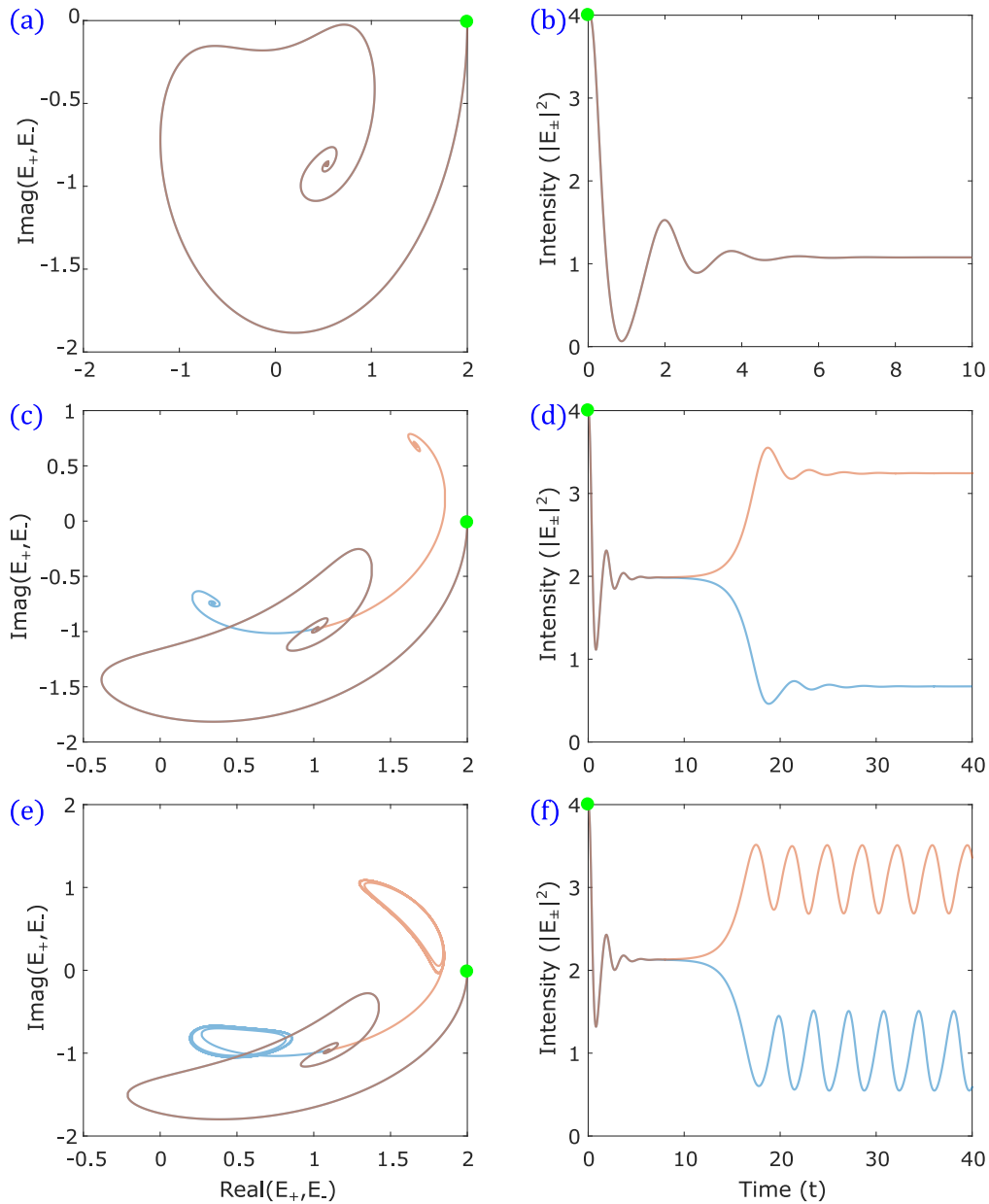
Figure 4.2: Temporal evolutions of E_+, in red, and E_-, in blue, (with brown implying an overlap) using Eq.(3.16), from initial conditions of $E_+ = (2.000, 0)$ and $E_- = (2.0001, 0)$ with $A = 1$, $B = 2$, $I = 3.8$ and a time step of $dt = 0.001$. LHS panels show the temporal evolutions through the complex phase space, while the RHS panels show how the coupled field intensities vary over the same evolution. For (a,b) $\theta = 1.5$, for (c,d) $\theta = 5$, and for (e,f) $\theta = 5.5$.

4.3 Periodic Doubling Bifurcations, Cascades, Chaos and Crises

When analysing the region of Fig. 3.7 which is susceptible to growing oscillations, it was noted that the system would not always settle on some regular temporal oscillation. Instead at times the system would appear to evolve chaotically. This prompted an investigation into the types of oscillation which may be possible for Eq. (3.16).

By the numerical integration of Eq. (3.16) for many iterations it is possible to begin to build up a picture of how the oscillations themselves evolve over time, i.e. whether or not they establish a stable singular characteristic frequency of oscillation or if they in fact have some other second, or many, frequency components. Tracking the circulating field intensities $P_{1,2}$ and recording their local maxima, where the first derivative is zero and the second derivative is negative, it was possible to evaluate a Poincaré section for a variation in the cavity detuning. Figure 4.3, shows an example of this, with forward scans of detuning changing θ from 5 to 11 at $I = 3.4$ for (a) and $I = 3.8$ for (b), and a reverse scan: θ from 11 to 5 at $I = 3.4$ for (a) and $I = 3.8$ for (c). Note that this figure does not show the early iterations, only the late, i.e. once the system has been given suitable time to evolve and potentially settle.

The points on Fig. 4.3 begin (end) with Hopf (inverse-)bifurcations which occur when the real part of one or more of the eigenvalues, Eq. (3.23), become positive (negative) and rather than the system settling on focused points it instead follows some closed curve [97, 98]. The Hopf bifurcation indicates the start of oscillations, initially with one local maxima which is repeatedly plotted, but, upon suitably increasing the detuning, eventually the system may then also be susceptible to a period doubling bifurcation [99] - leading to a second local maxima being present on the Poincaré section, as seen in Fig. 4.3 (a).

Increasing the input pump power can lead to increases in the complexity of the Poincaré sections. Below some input limit the period doubling bifurcation does not occur for any value of the cavity detuning, whereas increasing it can lead to the simple situation of (a) or increasing it further, to many subsequent (or a cascade of) period doubling bifurcations, as seen in the column of points marked for some detunings in Fig. 4.3 (b,c). An example of a complex oscillation in this region is given in Fig. 4.4.

This sequence of many period doubling bifurcations can lead to the system exhibiting deterministic chaos, collision of Feigenbaum cascades [100], and
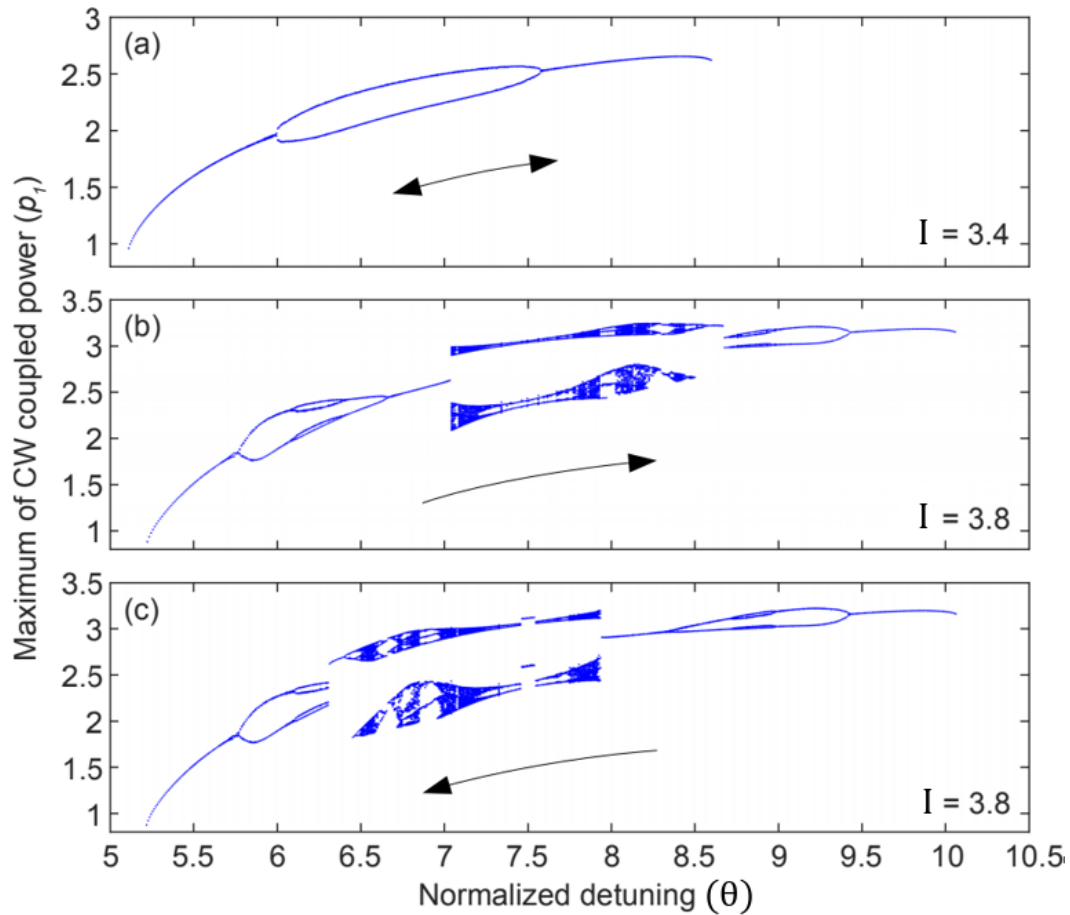
Figure 4.3: Detuning scans of the oscillatory regimes of Eq.(3.16) between two
Hopf bifurcations. The field intensity is sampled at its maximum during the
oscillation. A single value of P_1 for a given θ means that only one (maximal)
value of P_1 intersects the Poincaré section during its trajectory with a single
periodicity. In contrast, two values of P_1 for a specified θ means that the
maximum of P_1 is cycling between two distinct values with an overall period
that has doubled. Further period-doublings are observed for larger values of
θ, which eventually transition into chaos. The arrows indicate the direction
of scanning the detuning. (a) Scan for $I = 3.4$ (showing no dependence on
direction). Forward (b) and backward (c) scans for $I = 3.8$.
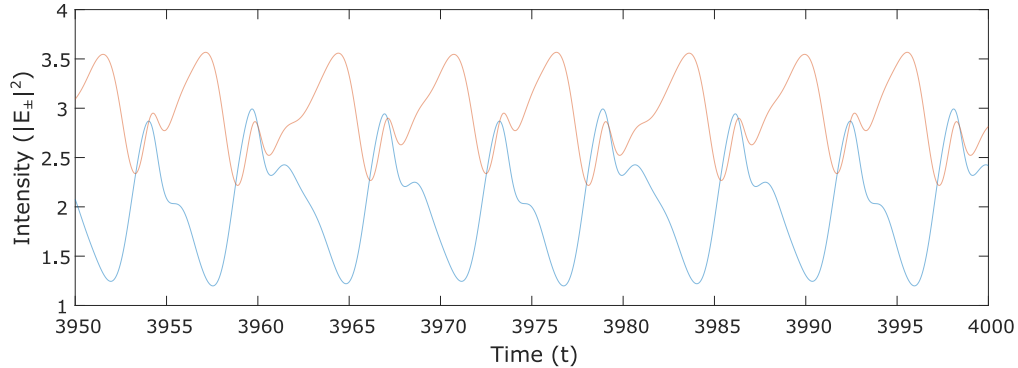
Figure 4.4: Complex temporal evolutions of $|E_+|^2$, red, and $|E_-|^2$, blue, using
Eq. (3.16) with $A = 1$, $B = 2$, $I = 3.8$ and $\theta = 7$. Note the more complex
nature of the intensity oscillation, when in comparison with Fig. 4.2, with the
apparently random fluctuations in the heights of the local peak intensities of
the two circulating fields, further note the small overlap of the fields' intensities.

crises. It is interesting to note that a bistability is also observed between these
dynamical regimes, as shown in Fig. 4.3(b,c), i.e. when the direction of the
detuning scan is reversed, leading to an alternate Poincaré section.

4.4 Self-switching Dynamics

As can be seen in the relatively complex oscillations of Fig. 4.4, given an
appropriate set of input conditions the size, or range, of the oscillatory paths
which the two fields take can partially overlap. The obvious question for
investigation therefore was whether the system could be fed input conditions
suitable enough to force the range of the oscillatory paths to overlap entirely,
and to see if this could produce yet further complex or novel behaviours.

Figure 4.5 is a similar Poincaré section to Fig. 4.3 only now both the local
maxima and minima of the two circulating fields are plotted in red. The full
range of the oscillations can also be seen, shaded in semi-transparent blue
and yellow. The semi-transparent shading has the nice effect of showing a
green colour where the two intensity oscillations begin to overlap. To show
the relationship, the Poincaré and shading are overlaid atop the HSS. With a
higher input intensity, $I = 4.0$, it can easily be seen in this figure that one may
classify three distinct regions of the intensity oscillations. In region (1) the two
circulating fields have intensities which oscillate with no overlap, such as with
Fig. 4.2 (e,f), contrary to region (2) where there is partial overlap, such as
Fig. 4.4, but the dominant and submissive fields maintain their respective
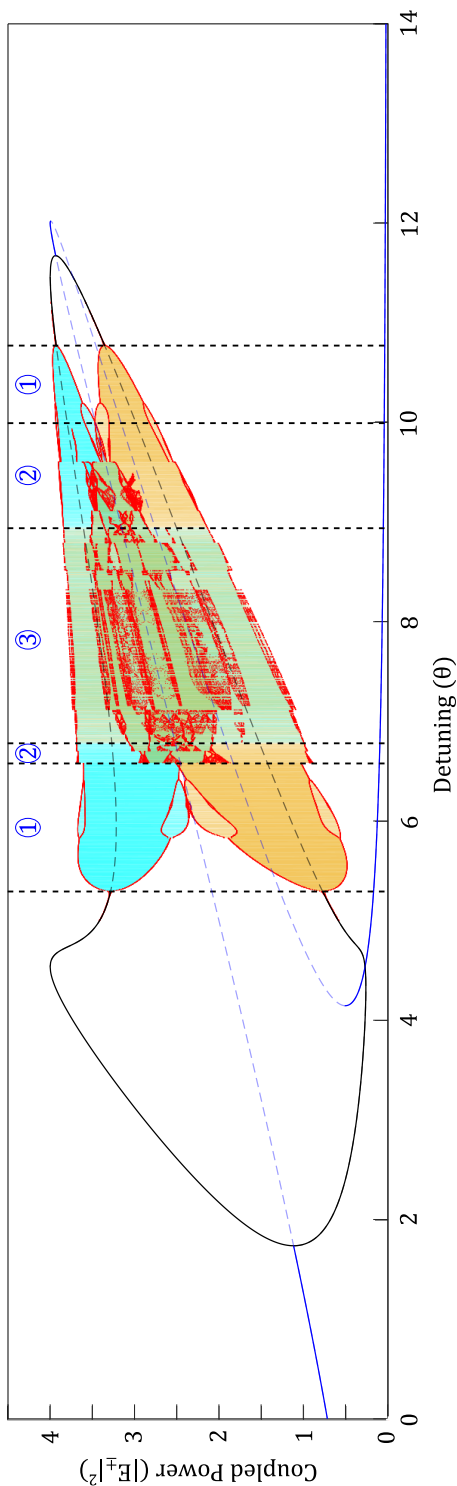
Figure 4.5: Stationary and oscillatory intensities, described by Eq. (3.16), under a forward detuning scan, with $I = 4.0$. The blue and black lines indicate the symmetric and symmetry-broken stationary solutions, respectively, with solid lines indicating stable states and pale dashed lines indicating unstable states. The red dots denote Poincaré sections, where a red dot is placed at each local minimum and maximum of an oscillation. Also shown, in semitransparent yellow and blue, are the full ranges of the oscillations. The yellow and blue shading results in a green colouring where the oscillations overlap. One observes three distinct regions: In zones (1), the oscillations in intensity do not overlap. In zones (2), they partially overlap, but this does not cause switching. In zone (3), switching occurs between the intensities of the two counter-propagating modes.

roles, and finally there is a third region, where the overlap of the two fields
becomes the entire range of the intensity variation, and the dominant role is
often exchanged between the two fields.

An alternative method of observing this region (3), where there is complete
overlap, is by plotting the averages of the two fields over an extended period of
time. Figure 4.6 shows the same simulation as Fig. 4.5 but now, in green and
red respectively, the mean field intensity is plotted. Outside of the highlighted
yellow region lies regions (1,2) of Fig. 4.5, and one observes that although the
two fields oscillate, and even partially overlap, one of the two fields can always
be described as being dominant. Within the yellow highlighted region however
the averages intensities of the two fields over a long time scale become equal
and now neither field can be singled out as being consistently dominant over
the other, this is an example of a symmetry restoration crisis [101].
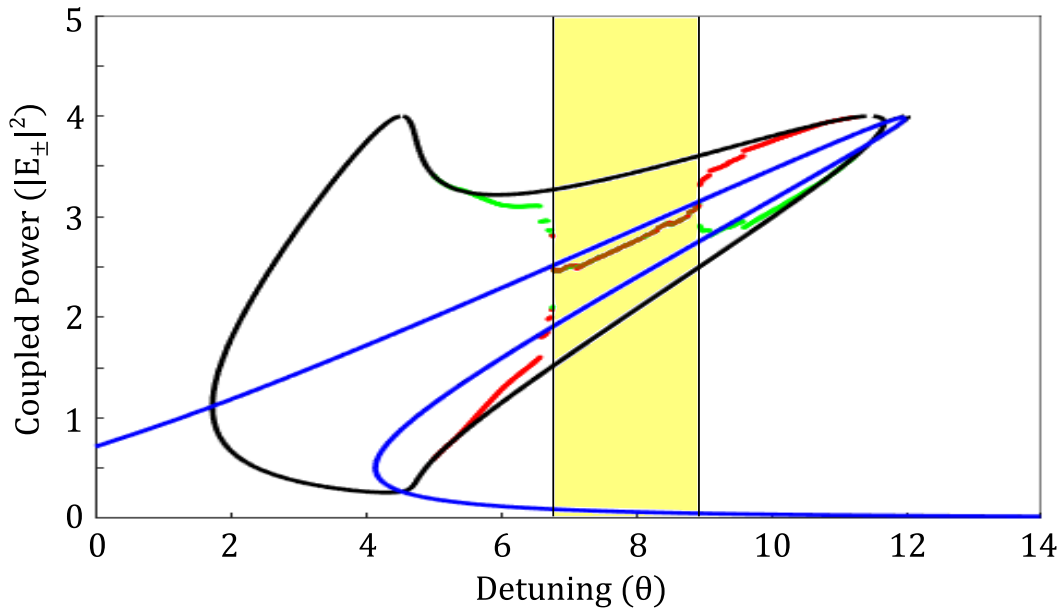
Figure 4.6: Similar to Fig. 4.5, only now the average intensities of the field's
oscillations are shown in green and red. The highlighted region indicates (3) of
Fig. 4.5, where one can observe the symmetry restoration of the average field
intensities when observed over long time scales. Black and blue line are the
asymmetric and symmetric HSS solutions respectively, shown for comparison.

It is also interesting to note in Fig. 4.5, and Fig. 4.3 for that matter, that, similar to the logistic map of Fig. 4.1, there are very thin regions within the chaotic columns where spontaneously a very thin gap appears with only a couple of dots, implying a switch from complex to relatively simple dynamics. Shown in Fig. 4.7, this spontaneous emergence of order from apparent chaos is caused by the momentary merging of two attractors.

Similar to Fig. 4.2, Fig. 4.7 shows the evolutionary paths carved out by the two circulating fields. The panels on the left hand side show the movement through the complex plane whereas those in the middle show the intensity evolutions. The right column shows the power spectra. In panels (a-c) one initially observes two separate attractors for $\theta = 6$ with no overlap of the oscillatory intensities. These panels have reletivly simple dynamics with relatively few (asymmetric) frequency components. Increasing the detuning to $\theta = 6.5$, panels (d-f), the two field's phase space paths begin to overlap with each other and this interactions begins to cause complex and non-repeating dynamics, leading to some variation in the circulating intensities and the emergence of many small frequency components in the spectra. Panels (g-i) show the evolutions for $\theta = 7$ which causes a much closer overlap of the two evolution paths, note that the overlap is still imperfect. This can lead to very complex dynamics and is indicated by a column of points on the various Poincaré sections and is also shown by the large number of significant frequency components. Finally, in panels (j-l) we show the case when $\theta = 8.8$. One can now see that the two attractors have completely merged leading to the two fields taking the exact same paths, but out of phase to one another, characterised by the periodic switching of the dominant and suppressed field roles. This periodic switching thus restores on average over a short time scale the symmetry of the system and one can see that this leads to a very well structured, and symmetric, spectra.

The existence of these switching dynamics was experimentally observed by collaborators in Ref. [102], reproduced in Fig. 4.8. Although not perfect periodic switching, due to experimental difficulties in obtaining perfectly balanced input conditions, Fig. 4.8 shows close replication of the periodic interchange of the dominant and suppressed fields. In the next chapter methods of increasing the robustness of the perfectly periodic interchange are discussed which should alleviate some of these experimental difficulties for future study.
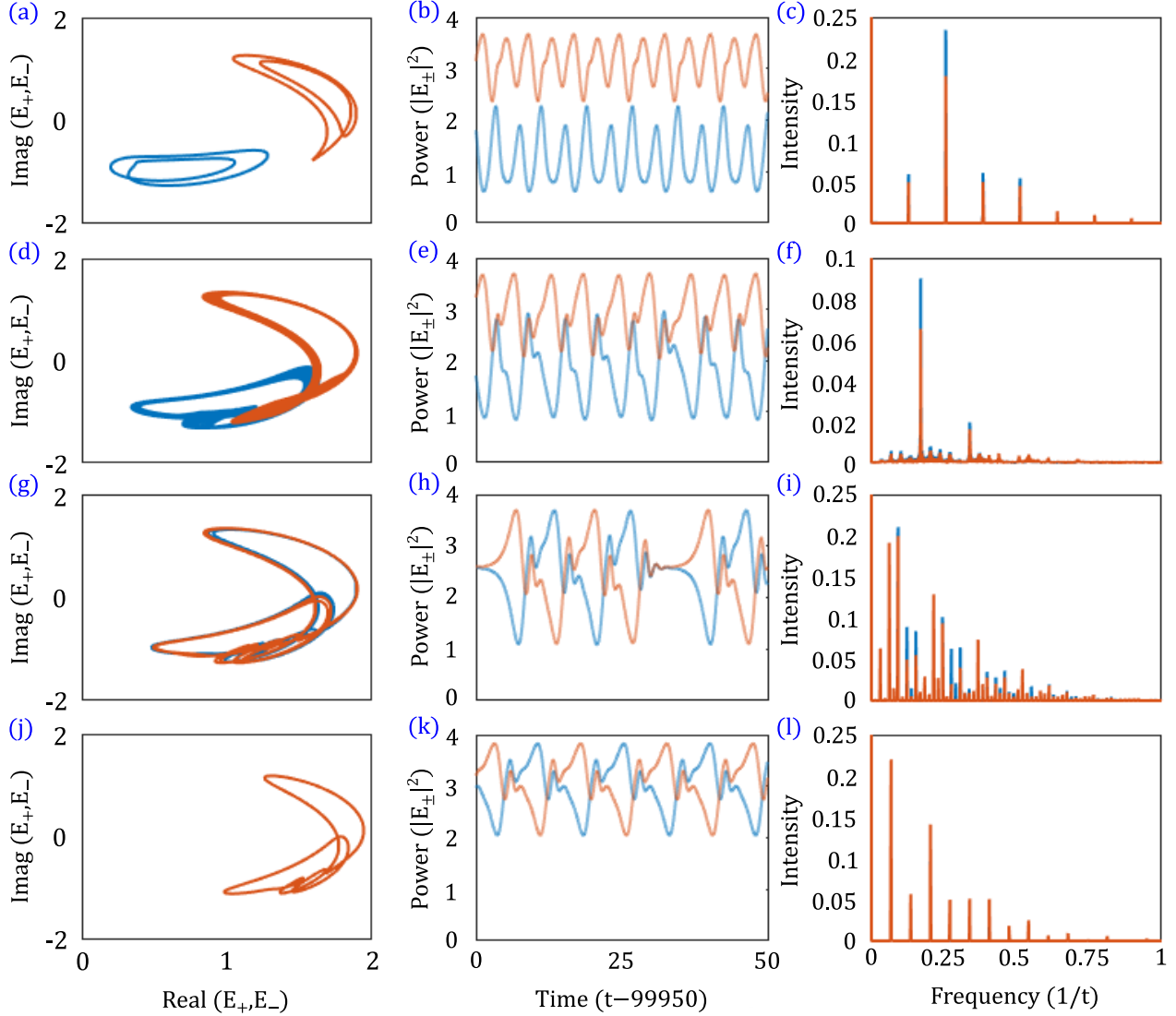
Figure 4.7: Temporal evolutions and spectra of the circulating fields for $A = 1$, $B = 2$, $I = 3.8$ and $\theta = 6$, 6.5, 7, 8.8 for panels (a-c), (d-f), (g-i) and (j-l) respectively. The left column shows the evolutions of $E_\pm$ in complex phase space. The middle column of panels shows the intensities $|E_\pm|^2$ over a late time period, and finally the right column shows the frequency components of the intensity evolutions of the two fields $|E_\pm|^2$. It can be seen how the system initially orbits two separate attractors yet, as the cavity detuning is increased through the rows, the two attractors begin to increasingly overlap, furthering the complexity of the oscillations, before overlapping completely, leading to the ordered periodic switching of the two fields. For all panels the red line refers to the E_+ field and the blue refers to E_- field.
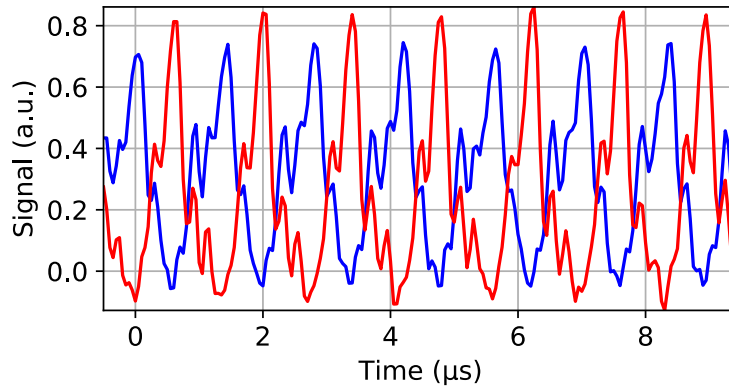
Figure 4.8: Experimental verification of the possibility for near perfect periodic switching. The evolution paths are not perfect mirrors of each other, note differing maxima, due to experimental imbalances. Details on the experimental conditions can be found in Ref. [102]. Results and figure supplied by L. Del Bino. Red and blue lines refer each to one of the two modelled fields $E_{\pm}$.

4.5 Chapter Summary

In this chapter we investigated the non-local temporal dynamics of the counter-propagating system, where $A = 1$ and $B = 2$, for a variety of cavity detunings. It was shown, in agreement with the eigenvalue analysis of the previous chapter, that the system is susceptible to leaving unstable symmetric states in the presence of noise in favour of the stable asymmetric states and that when the asymmetric states themselves are unstable, to growing oscillations. The resultant oscillations at low detunings and input intensities were found to eventually cease their growth and settle to a stable path with consistent maximum amplitudes.

In the cases where higher intensities and detunings were analysed, the dynamics could become much more complex - with single (or multiple) period-doubling bifurcations occurring, causing the system's oscillations to repeatedly alternate between two (or more) different maximums. Many sequential period-doubling bifurcations could also occur, which led to very complex and even apparent chaotic oscillations. Within this chaos small regions of order were found, leading to the periodic switching of the dominant and suppressed field roles.

This sporadic behaviour was found to be caused by a global bifurcation brought about by the the merging of two chaotic attractors. This merging partially restored symmetry to the system with the average field intensities on

relatively short time scales becoming equal. Experimental results confirmed the existence of this phenomena, even in the presence of imbalanced input conditions, implying that the general switching dynamic is quite robust, this said, in the next chapter it will be shown that this robustness can be increased further.
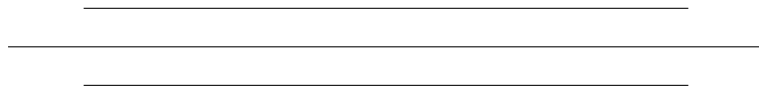
*"Take nothing on its looks; take everything on evidence.
There's no better rule."*

– Charles Dickens, Great Expectations

Chapter 5

The Effects of Self- and Cross-phase Modulation

Contents

5.1   Introduction

Self- and Cross-phase modulation (SPM and XPM) are important nonlinear
effects which induce a phase shift in light traveling through a medium. The
effects are caused by the optical Kerr effect which makes the refractive index of
a medium become light-intensity dependent. SPM and XPM are not only very
important in optical telecommunications [103] but also feature prominently in
the coupled system Eq. (3.8).

5.1.1   What is Self- and Cross-phase Modulation?

Self-phase Modulation (SPM) amounts to a nonlinear phase delay of a field
which is brought about by its own intensity and was first observed by Shimizu
in 1967 [104, 105]. It is a consequence of the optical Kerr effect which, recall,
occurs when high intensity light travels in an appropriate media and causes a
change in the refractive index, $\Delta n = n_2 I$, where I is the light intensity and
n_2 is the nonlinear index of the medium.

In systems where the light field which is propagating is non-homogeneous,
for example with a 'pulse' of light, the temporal structure of the varying in-
tensity leads to a temporal structure of the refractive index, in turn changing
the propagation velocity of the light field and hence also a phase change inside
the pulse.

SPM is present due to effects of the field in question itself, but what if there
exists a second field within the system, such as with Eq. (3.8)? Surely this
second field will induce a similar effect on the refractive index and, in turn,
this should also have an effect on the initial field. This is indeed exactly what
happens in refractive media [106], but the strength of this XPM is, more often
than not, different to that of the SPM. The total phase change is therefore not
only due to the primary field being observed, but also due to the other fields
in the system.

In the previous chapters the constants A and B which appeared in the
coupled Lorentzian Equations, restated below, were left unexplained. These
constants are in fact the SPM and XPM coefficients, with the particular values
that these constants can take very much depending on the physical system,
counter-propagating or circularly-polarised, which is being studied. We begin
the chapter by describing the possible values of the SPM and XPM within
each of our systems and then go on to describe the effects that this has on the
symmetry breaking and other phenomena.

5.2 Self- and Cross-phase Modulation Constant Values

Restating Eq. (3.9), the HSS for the field intensities of both studied systems are given by:

$$P_{1,2} = \frac{I}{1 + (\theta - AP_{1,2} - BP_{2,1})^2},\tag{5.1}$$

The values that the constants A and B can take in the system of Eq. (5.1) very much depends on the physical system being studied.

5.2.1 Counter-propagating fields

In the previous chapter the equations describing a ring resonator with two counter-propagating fields were always given with the SPM and XPM: $A = 1$ and $B = 2$ respectively, as is stated in [14, 32]. However it should be noted that this is only true for specific types of resonators. The general form of the equation is given with:

$$A = 1 , \quad B = 1 + h ,\tag{5.2}$$

with $0 \leq h \leq 1$. Here, the XPM is due to the standing-wave interference of the two fields resulting in an index grating within the medium [107–110].

In a highly diffusive Kerr medium, such as with some liquids or gases, this index grating can quickly be 'washed out', and so, its XPM effect is relatively weak, $h \to 0$. In a medium with little to no diffusive effects, leading to a robust index grating, the XPM is maximised with $h \to 1$. Under this effect therefore the XPM can range from $1 \leq B \leq 2$. Gases and liquids could be used, for example, in hollow fibres [111] to create appropriate ring resonators showing these differing XPM strengths.

Two counter-propagating fields	A	B
Solids (without diffusion)	1	2
General diffusive effects	1	$1 + h,$
		$(0 < h \leq 1)$
Gases (high rates of diffusion)	1	$\to 1$

Table 5.1: Table of values that the SPM and XPM coefficients, A and B respectively, may take in Eq. (5.1) for the counter-propagation system.

5.2.2   Orthogonally polarised fields

Whilst there is a spectrum of values that the XPM can take in the "counter-propagating" system, it is still limited to values from $1 \leq B \leq 2$. In the case of two co-propagating orthogonally polarised fields however, the values which both the SPM and the XPM can take has much more variety, but once again, these possible values are often dependent on the material making up the resonator.

In this setup the SPM and XPM are related to the third order susceptibility tensor, $\chi^{(3)}$, by

$$A = \frac{\chi^{(3)}_{1122} + \chi^{(3)}_{1212}}{\chi^{(3)}_{1111}}, \qquad B = \frac{\chi^{(3)}_{1122} + \chi^{(3)}_{1212} + 2\chi^{(3)}_{1221}}{\chi^{(3)}_{1111}} \tag{5.3}$$

(adapted for our A, B from Ref. [33]) with the constraint that, for CW pumps, $A + B = 2$ for an isotropic medium with neglected dispersion [33].

The other cases are: a nonresonant electronic response, $A = 2/3, B = 4/3$; liquids or molecular orientation, $A = 1/4, B = 7/4$; and electrostriction, $A = 1, B = 1$ [1].

Atomic vapours, deviating momentarily from Kerr media, are predicted to show phenomena offering a wide range of possible magnitudes of A and B [33, 112], experimentally shown in Ref. [113] . Again, these atomic vapours could be used, for example, in hollow fibres [111] to create appropriate ring resonators.

Modification of an effective $\chi^{(3)}$ nonlinearity has been demonstrated in periodically-poled lithium niobate (PPLN) [114, 115] and bismuth borate [116]; cascaded quadratic nonlinearities have also been used to realise a negative effective nonlinear coefficient in the context of self-phase modulation [117–119]. We also speculated in Ref [120] that it may be possible to generate $B/A < 0$ through appropriate material engineering - as considered, for example, in Ref. [119]. In a side note to this section, self- and cross-phase modulation coeffcients with opposite sign are used in spin-orbit-coupled Bose-Einstein condensates (BEC) [121].

Two copropagating polarisations	A	B
Isotropic media	$A + B = 2$	
Non-resonant electronic response	2/3	4/3
Liquids, or molecular orientation	1/4	7/4
Electrostriction	1	1
$\chi^{(2)}$ media with effective $\chi^{(3)}$	Wide range of values of B/A	
Atomic vapours	Wide range of values of B/A	
Bose-Einstein condensates		
Spin-orbit-coupled BEC	Wide range of values of B/A	

Table 5.2: Table of values that the SPM and XPM coefficients, A and B respectively, may take in Eq. (5.1) with regards to the resonator medium when applied to two co-propagating, circularly polarised, fields. Appropriate engineering of other phenomena may allow for further values of SPM and XPM coefficients.

5.3 Effects of SPM and XPM on Optical Bistability and SSB Phenomena

5.3.1 Bistability of Symmetric Field Intensities

The purely symmetric set of HSSs to the coupled LLE/Lorentzian systems, where $|E_+|^2 = |E_-|^2$, causes the system to degenerate to a single equation:

$$P_{1,2} = \frac{I}{1 + [\theta - (A + B)P_{1,2}]^2},\tag{5.4}$$

or, in cubic polynomial form:

$$I = (1 + \theta^2)P_{1,2} - 2(A + B)\theta P_{1,2}^2 + (A + B)^2 P_{1,2}^3,\tag{5.5}$$

As explained in Section 2.3.4, equations of this form are known to have the potential to exhibit a bistability when changing the input pump, see Fig. 5.1. Since Eq. (5.5) depends in key places on the self- and cross-phase modulation constants, this potential bistability also depends on such constants.

The range of input pump intensities where the bistable region emerges can be determined through finding the stationary points of Eq. (5.5), i.e where:

$$\frac{\partial I}{\partial P_{1,2}} = (1 + \theta^2) - 4(A + B)\theta P_{1,2} + 3(A + B)^2 P_{1,2}^2 = 0,\tag{5.6}$$

which is solved by:

$$P_{1,2} = \frac{2\theta \pm \sqrt{\theta^2 - 3}}{2(A + B)}, \qquad (5.7)$$

and substituting these values back into Eq. (5.5), yielding:

$$I = \frac{-2(2\theta \pm \sqrt{\theta^2 - 3})(-\theta^2 \pm \theta\sqrt{\theta^2 - 3} - 3)}{27(A + B)}. \qquad (5.8)$$

These results are visualised in Fig. 5.1.

Equation (5.8) reveals useful insight on the bistable region. Firstly, with absolutely no dependence on the strength of the self- and cross-phase modulation within the system, the cavity detuning must always be greater than $\sqrt{3}$ for bistability to be possible, and secondly with the possibility of bistability established through appropriate detuning, the value of $(A + B)$ affects the range of input intensity for which this bistability occurs.
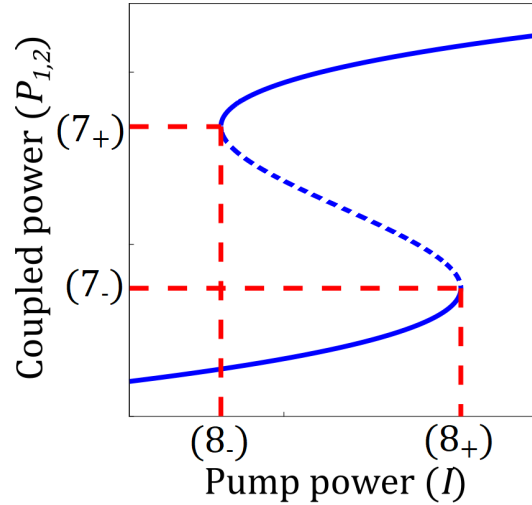
Figure 5.1: An arbitrary example plot of Eq. (5.5). It should be used as a point of reference for the equations (5.7) - (5.8), with $(7_\pm)$ indicating Eq. (5.7) with $\pm$ signs respectively and similar for $(8_\pm)$ with Eq. (5.8).

5.3.2   Analysis of Symmetry-broken Solutions

We turn our attention now to the purely asymmetric solutions of Eq. (5.1), specifically as to how they are affected by variations in the self- and cross-phase modulation.

We begin analysing the input intensity 'scans'. To aid in a mathematical
analysis, we add symmetries to Eq. (5.1), which yields the bubble of Fig. 3.4
(a) Recall this equation:

$$\left[1 + (\theta - AP_1 - BP_2)^2\right] P_1 = \left[1 + (\theta - AP_2 - BP_1)^2\right] P_2. \qquad (5.9)$$

To observe the purely asymmetric solutions to this equation requires some
further manipulation. The purely asymmetric set of solutions can be found
by taking the full Eq. (5.9) and dividing it by the symmetric counterpart
equation, Eq. (5.9) with the enforcement that $P1 = P2$. It is not advisable
to complete this simplification by hand, but such a simplification yields an
equation mapping only the asymmetric solutions and is given by:

$$[\theta - A(P_1 + P_2)]^2 - P_1 P_2 (B - A)^2 = -1, \qquad (5.10)$$

With the set of asymmetric solutions now reduced to this much simpler form,
further manipulations may be completed with relative ease to obtain the key
points of the asymmetric solutions, notably the opening and closing of the
solution set (the symmetry breaking and restoring bifurcations) and the point
of maximum difference between circulating fields.

Symmetry-breaking Bifurcation and Inverse-bifurcation Points

The point at which asymmetric solutions spontaneously begin to (not) exist is
known as the symmetry-breaking (inverse-) bifurcation point, and for visual
aid, these points have been denoted a and b respectively on Fig. 5.2. This
is where the use of the additional symmetry of Eq. (5.10) and the earlier
removal of nearly all symmetric solutions becomes helpful, now the symmetry
breaking bifurcation and inverse bifurcation points are the only places where
there remains a solution where $P_1 = P_2$. Thus in setting $P_1 = P_2$ in Eq. (5.10)
one obtains:

$$[\theta - 2AP_1]^2 - P_1^2 (B - A)^2 = -1, \qquad (5.11)$$

or

$$(3A - B)(A + B)P_1^2 - 4A\theta P_1 + (\theta^2 + 1) = 0 \qquad (5.12)$$

and through the use of the quadratic formula:

$$P_{1,2} = \frac{-4A\theta \pm \sqrt{(-4A\theta)^2 - 4(3A - B)(A + B)(\theta^2 + 1)}}{2(3A - B)(A + B)}, \qquad (5.13)$$

and simplification this yields the two sought bifurcation points and their dependence on self- and cross-phase modulation strength:

$$P_{1,2} = C \pm \frac{D}{(3A - B)(A + B)}, \tag{5.14}$$

where

$$C = \frac{2A\theta}{(3A - B)(A + B)}, \tag{5.15}$$

and

$$D = \sqrt{-3A^2 + \theta^2(A - B)^2 - 2AB + B^2}. \tag{5.16}$$

Equations are presented in such a manner since Eq. (5.15) corresponds to the mid-point of the elliptic asymmetric bubble, as shown visually under point c in Fig. 5.2. Substitution of these coupled powers, $P_{1,2}$, into Eq. (5.4) can then yield the input pump intensity, I, if required.

Points of Maximum Difference

For many of the applications of the symmetry broken phenomenon it is beneficial to maximise the difference between the two circulating fields. The points of maximum difference are visually shown in Fig. 5.2 as points d and e. To calculate these points Eq. (5.10) was once again employed due to its simplicity. It was recognised that the points of maximum difference occur where $\partial P_1 / \partial P_2 = 1$. This partial derivative of Eq. (5.10) is given by:

$$\frac{\partial P_2}{\partial P_1} = -\frac{(b - a)^2 P_2 - 2A^2 P_2 - 2A^2 P_1 + 2A\theta}{(b - a)^2 P_1 - 2A^2 P_1 - 2A^2 P_2 + 2A\theta}, \tag{5.17}$$

which, when set equal to 1, yields:

$$P_2 = -P_1 + \frac{4A\theta}{(3A - B)(A + B)}. \tag{5.18}$$

inserting Eq. (5.18) into Eq. (5.10), simplifying, solving the resultant quadratic and finally simplifying again, yields the points of maximum difference:

$$P_{1,2} = C \pm \frac{1}{B - A} \frac{D}{\sqrt{(3A - B)(A + B)}} \tag{5.19}$$

Where, once again, substitution of these coupled powers, $P_{1,2}$, into Eq. (5.4) can then yield the required input pump intensity, I, if required.

67

The root within Eq. (5.19) provides a very interesting further result, it identifies a 'bursting ratio' for the bubble. Observe that within said root, if $B/A < -1$ or $3 < B/A$ then the roots become imaginary and hence no real solutions of $P_{1,2}$ exist for Eq. (5.19). That is to say, the difference between the two circulating fields may grow indefinitely, the 'bubble' of asymmetric solutions opens, but never closes - it has burst. In more mathematical language, the ellipse becomes a parabola, see Fig. 5.3.
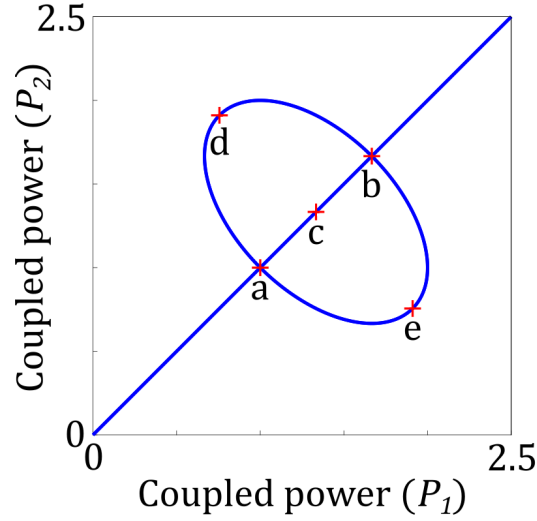
Figure 5.2: A restating of Fig. 3.4 (a) with appropriate points of interest marked for visual aid. Points a and b are the symmetry breaking bifurcation and inverse bifurcation points respectively, c denotes the midpoint of the elliptical bubble of asymmetric solutions and finally d and e show the points with maximum difference between the two circulating fields.

The Cavity Detuning Limit

Within the analysis of the root component of Eq. (5.13) a further useful result is yielded, a minimum requirement on the cavity detuning, θ, for symmetry breaking to be possible. For real solutions to exist in Eq. (5.13), $P_{1,2} \in \mathbb{R}$, the root component must be real, ie.:

$$\sqrt{(-4A\theta)^2 - 4(3A - B)(A + B)(\theta^2 + 1)} \in \mathbb{R}, \qquad (5.20)$$

which thus requires that:

$$(-4A\theta)^2 - 4(3A - B)(A + B)(\theta^2 + 1) \geq 0, \qquad (5.21)$$
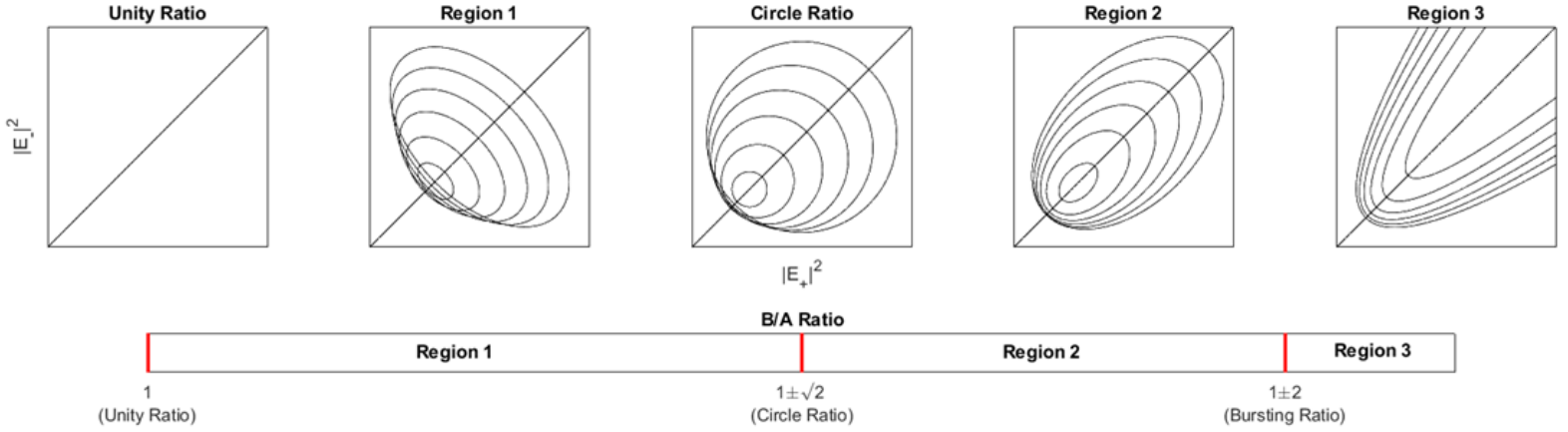
Figure 5.3: Variations in the ratio of the cross- to the self-phase modulation constants affect the 'shape' of the set of asymmetric solutions. Although this 'shape' is some what arbitrarily a form of an ellipse, outside of $-1 < B/A < 3$ the ellipse bursts into a parabola - meaning that the set of asymmetric solutions opens but never closes, leading to an infinite region of asymmetric solutions.

or, simplified, that the cavity detuning must obey the restriction:

$$|\theta| > \frac{Re\left[\sqrt{(3A - B)(A + B)}\right]}{|B - A|} \tag{5.22}$$

in order for asymmetric solutions, for some input intensity, to be at all possible. On the contrary, if this restriction is not satisfied asymmetric solutions will never occur for any input intensity.

The cavity detuning limit of Eq. (5.22), while an interesting and useful result even in itself, yields further insight into the system. The first result which is apparent arises from the necessity to avoid a division by 0. This may occur if $B = A$ and thus when $B/A = 1$, but at least here there is physical meaning to the undefined mathematics. It implies that when the self- and cross-phase modulation constants are equal, symmetry breaking is not possible for any cavity detuning, indeed the cavity detuning would need to be infinitely high to satisfy Eq. (5.22). A second result which can easily be seen from this equation is that when the ratio B/A falls outside of the region: $-1 \leq B/A \leq 3$, then the minimum detuning limit falls to 0, that is to say, that for some value of the input pump intensity, symmetry breaking is always possible.
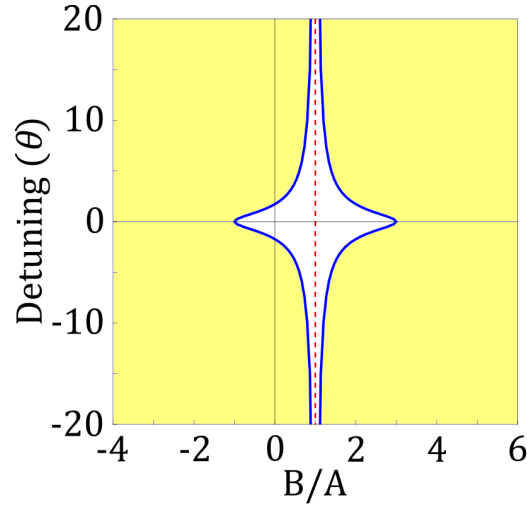
Figure 5.4: Minimum detuning, θ, required to observe symmetry breaking
when changing the ratio of the coupling constants B/A. The yellow regions
indicate where symmetry breaking is possible, for some range of input pump
intensity, with the blue lines indicating the limits where symmetry breaking
becomes impossible. In the white region symmetry breaking is not possible
for any range of input pump intensity.

Position of 'the bubble' relative to the 'S-shaped' bistabilty

In closing this section, note that the value of B/A also affects where the
symmetry-broken solution line appears with respect to the bistable symmetric
solution line. It is known that, for A = 1 and B = 2, when observing an
intensity scan, like that of Fig. 3.5, the symmetry-broken 'bubble' always
appears with a bistability on the symmetric solution line [32]. This is because,
for this B/A ratio, Eq. (5.22) dictates that symmetry-broken solutions are
only possible for $\theta \leq \sqrt{3}$, with $\theta = \sqrt{3}$ being the condition where optical
bistability emerges. This holds true for any $1 < B/A < 2$. Above ratios of
2 however, the minimum detuning for symmetry breaking falls below that for
optical bistability. This means that it is now possible to observe the symmetry-
broken solutions without bistability, Fig. 5.5(a). More interesting is the region
$B/A < 1$. For $0 < B/A < 1$, symmetry breaking is again only possible for
detunings above the $\sqrt{3}$ value for optical bistability, but now the symmetry-
broken bubble appears on the middle branch of the bistable region, as shown
in Fig. 5.5(b). Progressing further, for $B/A < 0$, it is once again possible to
observe the symmetry-broken solutions for detunings lower than the minimum
required for symmetric solution line optical bistability.

70
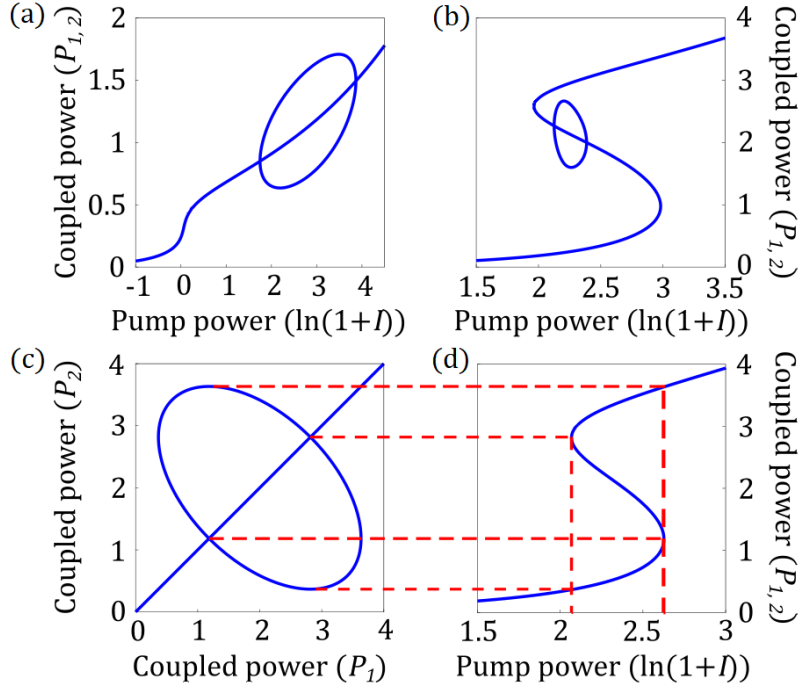
Figure 5.5: (a), (b) Plots of the input power scans for $B/A = 2.2$, $\theta = 1.5$ and $B/A = 0.5$, $\theta = 4$ respectively. (c), (d) show the special case of $B = 0, A \in \mathbb{R}$, with $A = 1$, $\theta = 3$. (c) shows the possibility for symmetry-broken solutions, while (d) shows how their origin is due to the bistable region of the Lorentzian equation.

We note that when plotting in the style of Fig. 5.2 for B $= 0$, it would appear that symmetry broken solutions are, interestingly, still possible, as shown in Fig. 5.5(c) even in the absence of any cross-phase modulation. This explains the continuous nature of all equations described previously, and Fig. 5.4, about $B/A = 0$. However in this case the appearance of the apparently symmetry-broken solutions is due to the imposed constraint that both θ and I are equal for both equations. This results in the two, now uncoupled, Lorentzian equations being identical. The 'symmetry-broken' solutions arise physically from the possibility of one field being on the top branch of the optical bistability while, simultaneously, the other is on the bottom, or vice versa, see Fig. 5.5(d), i.e it is not a symmetry breaking of coupled fields.

5.4 Effects of SPM and XPM on System Stability and the Corresponding Temporal Dynamics

5.4.1 Generalised Stability Analysis

This section reports on the generalisation of the stability analysis preformed in Section 3.3. Here we analyse the stability of the homogeneous solutions described by the equations:

$$\frac{\partial E_\pm}{\partial t} = E_{in} - \left[1 + i\left(A|E_\pm|^2 + B|E_\mp|^2 - \theta\right)\right]E_\pm, \qquad (5.23)$$

Following the procedure set out in Section 3.3, we add small perturbations to the steady state solution, calculate the eigenvalues of the matrix that results, and assess the stability of this system. The eigenvalues of the linear stability of Eq. (5.23) have the same form as those provided in Section 3.3:

$$\lambda = -1 \pm \sqrt{\frac{-\alpha_1\beta_1 - \alpha_2\beta_2 \pm S}{2}}, \qquad (5.24)$$

with

$$S = \sqrt{(\alpha_1\beta_1 - \alpha_2\beta_2)^2 + 4\alpha_1\alpha_2\gamma^2}, \qquad (5.25)$$

however now the quantities $\alpha_{1,2}$, $\beta_{1,2}$ and γ^2 take on forms generalised to arbitrary self- and cross-phase modulation coefficients: $\alpha_{1,2} = (AP_{1,2} + BP_{2,1} - \theta)$, $\beta_{1,2} = (3AP_{1,2} + BP_{2,1} - \theta)$, and $\gamma^2 = 4B^2P_1P_2$.

Note that again in Eq. (5.24) one $\pm$ choice enforces no restrictions on the other $\pm$, giving a total of four eigenvalues. The quantity S plays an essential role in establishing the stability of the system. If S is real, and the quantity under the square root in Eq. (5.24) is negative for both $\pm S$, i.e, $S < \alpha_1\beta_1 + \alpha_2\beta_2$, then all the eigenvalues are complex numbers with real part equal to -1, leading to full stability of the corresponding stationary states. On the other hand, if S is real, and the quantity under the square root in Eq. (5.24) is positive, then one real eigenvalue can be positive (meaning a non-oscillatory instability) if

$$S > 2 + \alpha_1\beta_1 + \alpha_2\beta_2, \qquad (5.26)$$

with the maximum of two real eigenvalues being positive when

$$S < - (2 + \alpha_1\beta_1 + \alpha_2\beta_2), \tag{5.27}$$

is also satisfied. Note that this condition for a second unstable eigenvalue is only possible when $2 + \alpha_1\beta_1 + \alpha_2\beta_2 < 0$.

Under the condition of S being purely imaginary, the eigenvalues, Eq. (5.24), are complex with the real (R) and imaginary (Ω) parts, corresponding to the growth rate and the angular frequency respectively.

The instabilities are then obtained by finding the conditions for which $R > 0$, and correspond to

$$|S^2| > 8 \left(2 + \alpha_1\beta_1 + \alpha_2\beta_2 \right). \tag{5.28}$$

This birth of a stable limit cycle implies a Hopf bifurcation. Note that, for this system, if we have a pair of oscillatory eigenvalues with positive real part, then the real part of the remaining two must necessarily be negative. Interestingly, oscillatory instabilities can only appear in the symmetry-broken branches of the stationary solutions, regardless of B/A; no oscillatory instability can be found on the symmetric branches, since, in this case, S is always a real number.

Real eigenvalue instabilities can be found on the symmetric branches of the stationary solutions, where $\alpha = \alpha_1 = \alpha_2$ and $\beta = \beta_1 = \beta_2$. Here, real S means $S = 2|\gamma\alpha|$ and the conditions Eq. (5.26)-(5.27) reduce to

$$|\gamma\alpha| > 1 + \alpha\beta, \quad \text{and} \quad |\gamma\alpha| < - (1 + \alpha\beta). \tag{5.29}$$

On the symmetric branches, the bifurcations corresponding to conditions given by Eq. (5.29) are either the saddle-node bifurcations of the S-shaped stationary curves or the pitchfork bifurcations leading to symmetry-breaking solutions.

To illustrate the effect of the cross-phase modulation coefficient on the stability of the system, we report here about two cases of large and small cross-phase to self-phase modulation ratio, B/A, with $A = 1$.

For larger values of B/A such as $B = 7$, $A = 1$, Fig 5.7 is not only consistent with a prediction made by Eq. (5.22), that symmetry-broken solutions are possible at zero detuning, but also shows that there are now large parameter regions where stationary states are susceptible to oscillations. On the contrary however Fig 5.8 illustrates stable, unstable, and oscillatory unstable regimes for a variety of choices of parameters for a small value of $B = 0.9$, with $A = 1$. Now the self-phase modulation is stronger than the cross-phase modulation. In this regime, the system is not strongly susceptible to either symmetry breaking or the onset of growing oscillations, and so the power
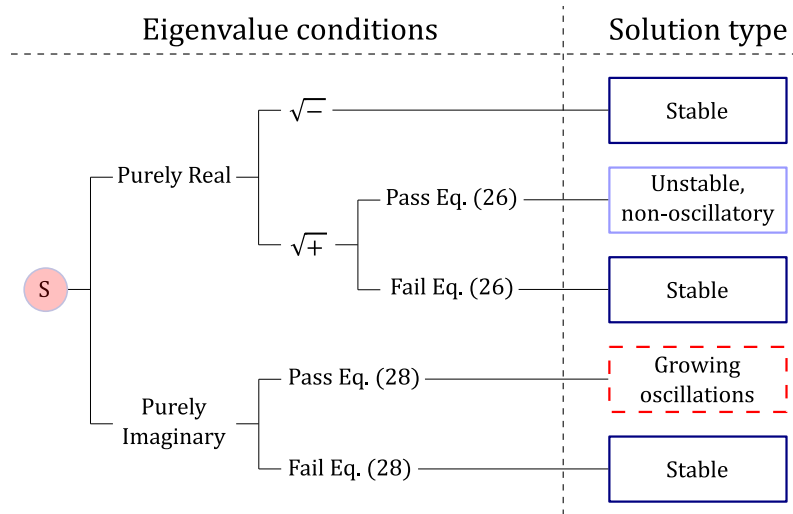
Figure 5.6: Reference chart showing eigenvalue conditions, beginning from
S, required to obtain solutions with various stability outcomes. This diagram
should be used in reference to section 5.4.1 for ease of understanding. Solution
types are colour coded to match that of figs. 5.8 and 5.7
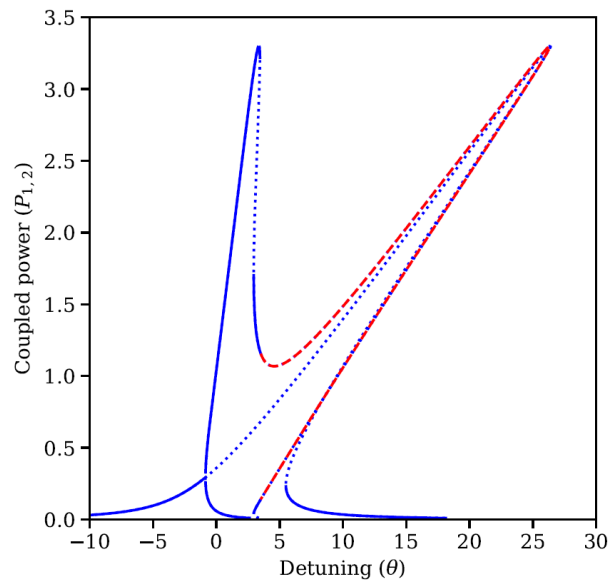
Figure 5.7: Coupled power $P_{1,2}$, against the detuning parameter, θ for $A = 1, B = 7$ and $I = 3.3$. Stable and non-oscillatory unstable solutions are shown
in solid and dotted blue, respectively, whilst oscillatory instabilities are shown
in dashed red.
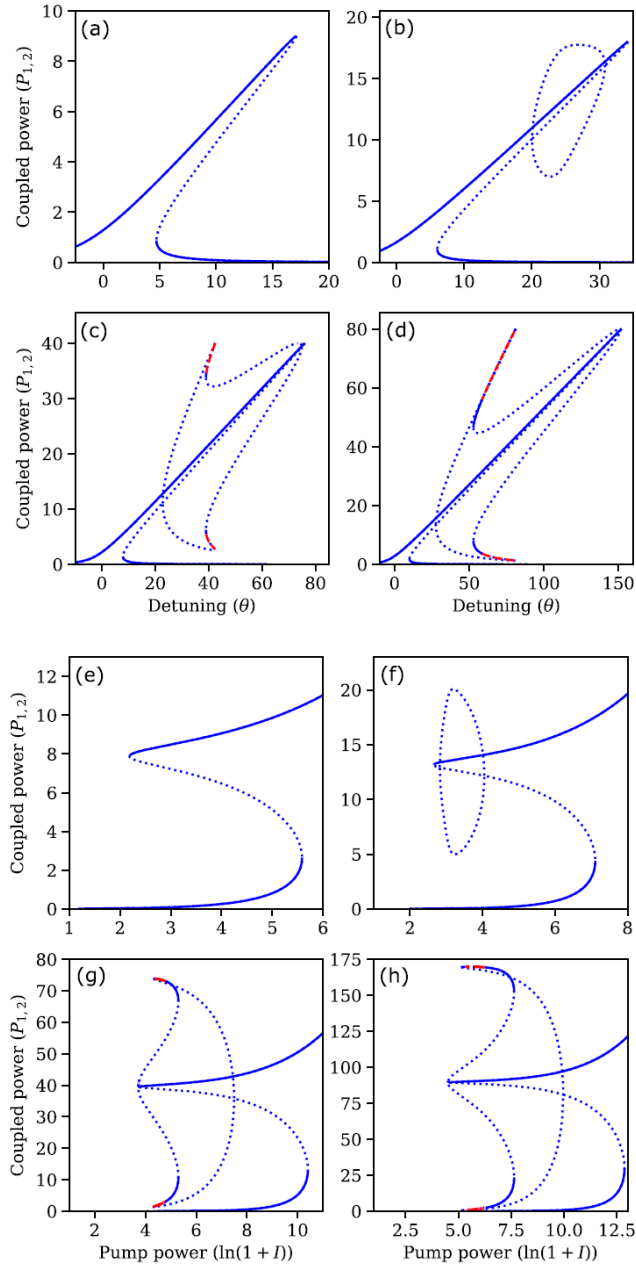
Figure 5.8: (a)-(d) illustrate the coupled power $P_{1,2}$, against the detuning parameter, θ for $A = 1$ and $B = 0.9$. (a) $I = 9$. (b) $I = 18$. (c) $I = 40$. (d) $I = 80$. The lower collection of plots illustrate the coupled power, $P_{1,2}$, against the input power, I. (e) $\theta = 15$. (f) $\theta = 25$. (g) $\theta = 75$. (h) $\theta = 170$. Stable and non-oscillatory unstable solutions are shown in solid and dotted blue, respectively, whilst oscillatory instabilities are shown in dashed red.

thresholds for accessing these phenomena are very high. When increasing
the input power, I, symmetry-broken solutions occur in the middle branch of
the bistable S-shaped curves. Some of these solutions later gain stability, and
others exhibit growing oscillations; the system begins to display multi-stability
of symmetric and asymmetric solutions; the fact that the growing oscillations
are always accompanied by a stable solution means that these oscillations may
be difficult to experimentally observable.

5.4.2 Temporal Dynamics

The stability analysis of the previous section described how the system re-
sponds to small, noise-like, perturbations with respect to changes of the ratio
B/A. In this section, we investigate the full temporal evolutions and oscilla-
tions by numerical integrating of Eq. (5.23) in a manner similar to Section
4.3. The temporal dynamics of optical systems can lead to a range of appli-
cations, such as polarization scramblers or devices with periodic switching of
polarisation state or direction. In Fig. 5.9 numerical integrations illustrate the
consequences of modifying the relative strengths of self- and cross-phase mod-
ulation for the onset and extent of deterministic chaos. Figure 5.9(a) shows
the maxima of the coupled power P_1 during oscillations when changing B from
1.5 to 7, for $A = 1$, $\theta = 5$, and $I = 3.3$. The power ranges spanned by the
oscillations clearly increase with the cross-phase modulation magnitude.

To illustrate the susceptibility of the system to temporal oscillations at
large values of B/A, we show in Fig. 5.9(b) the Poincaré sections for a de-
tuning scan for $B = 7, A = 1$ and $I = 3.3$. These are the same parameters
of the stationary solution curves displayed in Fig. 5.7. Note that at these
high detunings the regions where chaotic attractors merge to give the physical
behaviour of the periodic switching between dominant and suppressed field
roles become quite large and sustained, for example a continuous region of
this behaviour can be seen from $\theta = 4.65 \rightarrow 4.95$. Applications looking to
utilise this behaviour with a large degree of robustness should therefore use
appropriate ring resonators with high XPM.
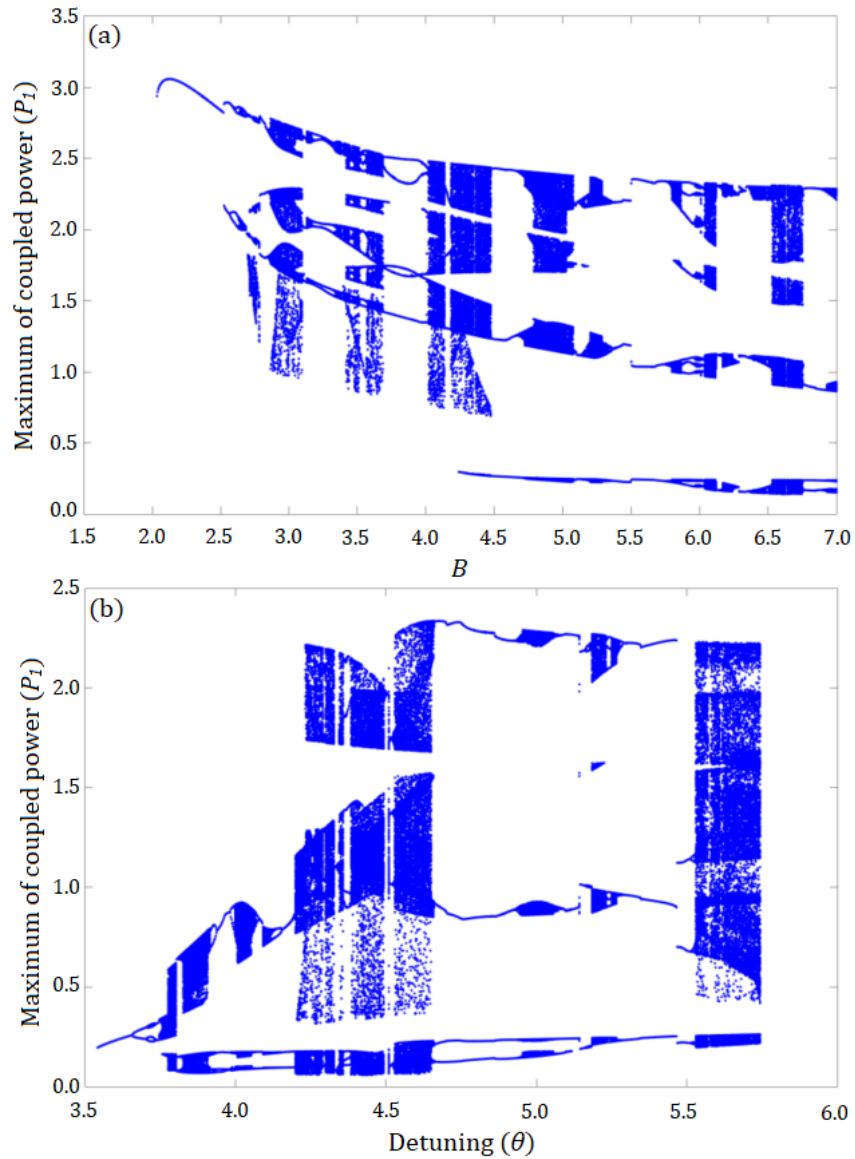
Figure 5.9: (a) Poincaré sections of the maxima of oscillating coupled power
P_1, versus the cross-phase modulation coefficient, B, for constant $A = 1$. These
points corresponds to constant values of the detuning $\theta = 5$ and input power
$I = 3.3$. (b) Illustration of periodic oscillations and deterministic chaos in the
Poincaré sections of the maxima of P_1 when varying the detuning parameter,
θ for a large cross- to self-phase modulation ratio. In this case, $A = 1, B = 7$
and the input power is $I = 3.3$. Note the dense columns of chaos with large
windows of order indicative of periodic switching. Both scans run from left to
right.

5.5   Chapter Summary

In this chapter we presented a theoretical model for the spontaneous symmetry breaking of light in ring resonators, generalised to arbitrary strengths of self- and cross-phase modulation, and describing the coupling of either two circularly-polarised or two counter-propagating fields. This was motivated by the recognition that these SPM and XPM strengths could vary extensively between experimental settings, particularly those featuring different nonlinear media, including Kerr liquids and atomic vapours.

We proceeded to present the characteristics of the steady-state symmetry-broken region of the system, such as the minimum input criteria for its observation, its opening and closing bifurcation points and the conditions for maximum difference in the coupled intensities in ways generalised to arbitrary strengths of SPM and XPM. One of the most useful results to emerge here was the bursting of the asymmetric bubble beyond certain SPM and XPM values, leading to a theoretically infinite symmetry broken region with no upper bound.

Later, it was described how the position of the symmetry-broken region varies with respect to the symmetric optical bistability, with the possibility of the asymmetric bubble forming on the middle branch of the S-shaped symmetric solution line and for the possibility of observing spontaneous symmetry breaking without the symmetric curve becoming at all bistable. This may be extremely useful for application requiring the asymmetric solutions but where one may wish to avoid the additional, at times stable, symmetric solutions.

Finally, we described the existence of a dependence of the oscillatory regime on the value of B/A. This could not only be useful in avoiding the oscillatory regime, when stationary asymmetric solutions are required at certain intensities, but could also be used to conversely promote the oscillatory regime and allow for the regions of periodic switching or chaos to become more robust with regards to the input parameters.

"Home is behind, the world ahead"

– J.R.R. Tolkein, The Lord of the Rings

Chapter 6

Symmetry Broken Temporal Cavity Solitons and Their Breathing Dynamics in Kerr Ring Resonators

Contents

6.1 Introduction

In 2019 we applied for, and were awarded, two travel scholarships. The combination of these two awards covered the planned costs of a ten week research visit to the University of Auckland, New Zealand. For this chapter's results, thanks must therefore be given to both the Mac Robertson Trust, who awarded the largest of the two scholarships, and to the Dodd-Walls Centre. We would also like to express our enormous gratitude to the University of Auckland for our hosting, with a special mention of the group of researchers we worked with, primarily Gang Xu, Julien Fatome, Stuart Murdoch, Miro Erkintalo and Stéphane Coen.

To those who know the history of the soliton, it may seem ironic that the majority of our work on the topic did not take place until we left our base in Glasgow, Scotland, to visit the other side of the world. This irony arises because the first recognition of the soliton actually occurred in Scotland, described in 1834 by the Victorian Engineer John Scott Russell [122–124].

Following these initial observations, many studied the mathematics behind solitary waves in the 19th century [125–127] resulting in the first known equation [123] describing a soliton's form, which came from solving the Korteweg–de Vries equation [128, 129]; this equation is given by:

$$\eta(x,t) = a\ sech^2\left[\beta\left(x - Ut\right)\right],\tag{6.1}$$

where $\eta(x,t)$ describes the solitary wave profile and a is the maximum amplitude of the formation above the free surface of liquid, depth h. β is defined by $\beta^2 = 3a/(4h^2(h+a))$ and the speed of the solitary wave is given by $U = \sqrt{g(h+a)}$ for gravitational acceleration g.

As one may expect, the area of study surrounding solitons has expanded greatly since these early 19th century studies. Solitons have now been found in many different systems and areas of physics; most relevant to this thesis are cavity solitons (CS) in the Lugiato-Lefever equation, which have been very impactful, with transverse CS in the LLE first detected by Scroggie and Firth at Strathclyde in 1996 [130, 131] and longitudinal or temporal CS (TCS) in the LLE being observed in 2010 [19, 20]. Here specifically we investigate TCS.

TCSs are the dissipative optical solitons [132–134] of coherently-driven nonlinear resonators [135]. In contrary to conservative solitons, where the only required system balance is that of the diffraction (or dispersion) with nonlinear effects, dissipative solitons require an additional balance. This is due to the inherent losses within a dissipative system; in order for a soliton to maintain its shape and velocity, an input pump of some kind is required to

exactly balance any losses the system exhibits [19].

TCSs have revealed themselves as ideal entities for the systematic investigation of fundamental dissipative soliton physics, permitting controlled experimental insights into a range of nonlinear dynamical phenomena [21, 87, 136–139]. Further to this, they have also enabled – particularly through their key role in the generation of coherent microresonator Kerr frequency combs [6, 84, 140] – ground breaking advances across numerous applications, including all-optical information processing [141, 142], telecommunications [143, 144], optical frequency synthesis [145], detection of extra-solar planets [146, 147], spectroscopy [148, 149] and ultrafast optical ranging [150–152].

TCSs have so far predominantly been studied in the context of single-component (scalar) systems involving a single (spatial and polarization) transverse mode family of the resonator. It is only very recently that researchers have begun to explore the novel realm of multi-mode (vectorial) systems [153–157]. In particular, asymmetric excitation of two distinct mode families has been shown to allow for the simultaneous emergence of two non-identical CSs [154, 156], enabling a novel route for the generation of multiple frequency combs from a single device [154]. However, solitons supported under strongly asymmetric conditions are still effectively scalar, being (almost) entirely associated with one of the modes excited. Whilst vectorial solitons that rely on a symbiotic combination between two orthogonal components have been extensively studied in single-pass waveguide propagation [158–160] and fibre lasers [161–163], there has so far been only a handful of theoretical studies on such structures in the context of temporal cavity solitons in passive resonators [153, 157].

In this chapter we describe how the spontaneous symmetry breaking phenomenon described in previous chapters may be combined with TCS to produce novel field behaviours, both stable and dynamic, such as mirror-like vectorial CSs and breathers. To the best of our knowledge, the experimental results which followed the theory outlined here comprised the first experimental observations of spontaneous symmetry breaking of TCSs (and non-homogeneous states in general) in a two-component Kerr resonator. Moreover, whilst SSB has been previously identified and observed for vectorial solitons of conservative systems [164, 165], and studied theoretically in the context of various dissipative systems [166–168], the results presented in our paper, on which this chapter is based, [88] represent the first direct experimental observation of SSB of dissipative solitons in any two-component physical system. As such, our work provides fundamental insights at the intersection of two widely investigated nonlinear phenomena, linking together the rich physics of (vectorial) dissipative solitons [169–172] and spontaneous symmetry breaking.

6.2 The Symmetry Breaking of Temporal Cavity Solitons

While many of the results described in previous chapters were applicable to both the situations of two counter-propagating linearly polarised fields and to that of two co-propagating orthogonally polarized light fields, the results in this chapter are purely limited to the latter. This is because we seek to observe the temporal evolutions of $E_\pm$ on the time scale of one round trip of the resonator. Whereas it was shown previously that both the counter-propagating and the orthogonally polarized systems are described by the same set of equations, Eq. (5.23), when assuming no variation of $E_\pm$ during a round trip, if there is considerable change during the round trip then the systems may differ. Here we study therefore only the orthogonally polarised case with self-focusing media (anomalous dispersion) which is described by the following restated equation [33]:

$$\partial_t E_\pm = E_{\text{in}} - E_\pm - i\theta E_\pm + i\partial_{\tau\tau} E_\pm + i\left(A|E_\pm|^2 + B|E_\mp|^2\right)E_\pm . \qquad (6.2)$$

One of the main inspirations for our studies of fast time temporal structures came from the single LLE and its predicted [173], and verified experimentally [174], ability to exhibit an instability which can lead to the viability of pattern and soliton solutions [42]. To first verify this claim it was required to code a suitable method of integrating Eq. (6.2), such as the split-step Fourier method combined with the Runge-Kutta method, as outlined in appendix A.

With such a suitable method of integration coded, the next step was to verify the existence of the predicted (symmetric, $E_+ = E_-$) TCS [173, 174], which may naturally emerge from the integration of Eq. (6.2) for a range of initial conditions containing adequately large non-homogeneous random perturbations. Figure 6.1 shows such an evolution, panel (a), and the final stage of the integration, panel (b), of such initial conditions, where we have also momentarily fixed $E_+ = E_-$. One can clearly see the emergence of the predicted TCS, or to be more accurate the emergence of a pair of symmetric TCS - one soliton in each field $E_\pm$. Here SPM and XPM constants were used which were similar to the experimental setup which would later be used to clarify our predictions [88]. The TCS of Fig. 6.1 and others of the type discussed in Refs [173, 174] can be described as 'sitting' on the bottom branch of the HSS, with the soliton itself locally locking to the pattern state [88].

Having verified the existence of TCS in our system we proceeded to remove the constraint that fixed $E_+ = E_-$ in order to begin the investigations into if a
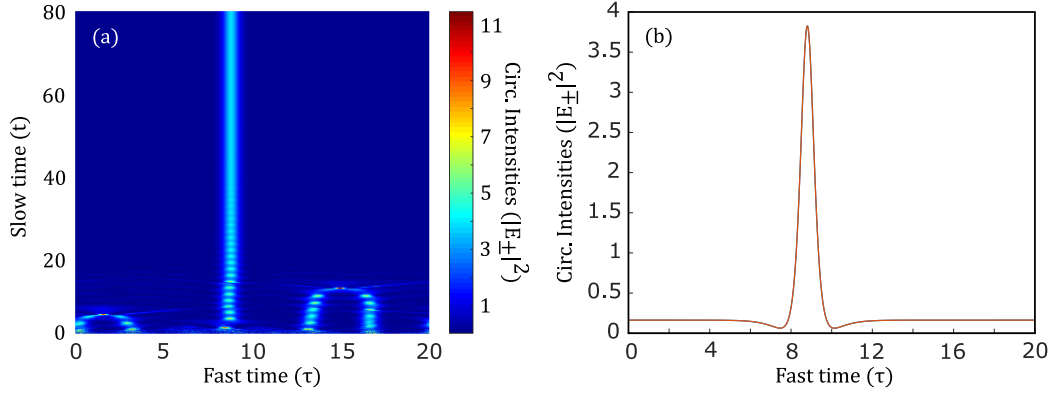
Figure 6.1: Results of the numerical integration of Eq. (6.2) from initial
conditions with adequately large non-homogeneous random perturbations with
$A = 1$, $B = 1.58$, $E_{in} = 1.5$ and $\theta = 4$, where we have forced symmetry on
the system by imposing the condition that $E_+ = E_-$. (a) shows the slow time
evolution of the two field profiles. (b) shows the final fast time profile of the
two field components which in this case happens to be a single soliton sitting
on the HSS solution.

symmetry breaking of symmetric TCS would occur. Figure 6.2 shows one such
simulation for the same set of input parameters as Fig. 6.1 . Panels (a) and (b)
show the fast time intensity profile evolutions for both circulating components
respectively and one can see how once again from the initial conditions, con-
taining adequately large non-homogeneous random perturbations, solitons can
naturally emerge without further engineering; the final profiles are shown in
panel (c) in red and blue respectively. (a,b) show that the symmetric solitons
which initially emerged from the initial conditions eventually split into two
asymmetric profiles with one soliton becoming dominant while the second is
suppressed, (c). Panel (d) shows the difference between the two fast-temporal
profiles and it is clear to see that initially the two field components evolve al-
most perfectly symmetrically to the attractive but unstable symmetric soliton
profile before, similar to the homogeneous case in Fig. 4.2(c,d), evolving away
from the unstable symmetric solution to the attractive and stable asymmetric
profiles. Results for similar parameters were later experimentally verified by
collaborators in Ref. [88].
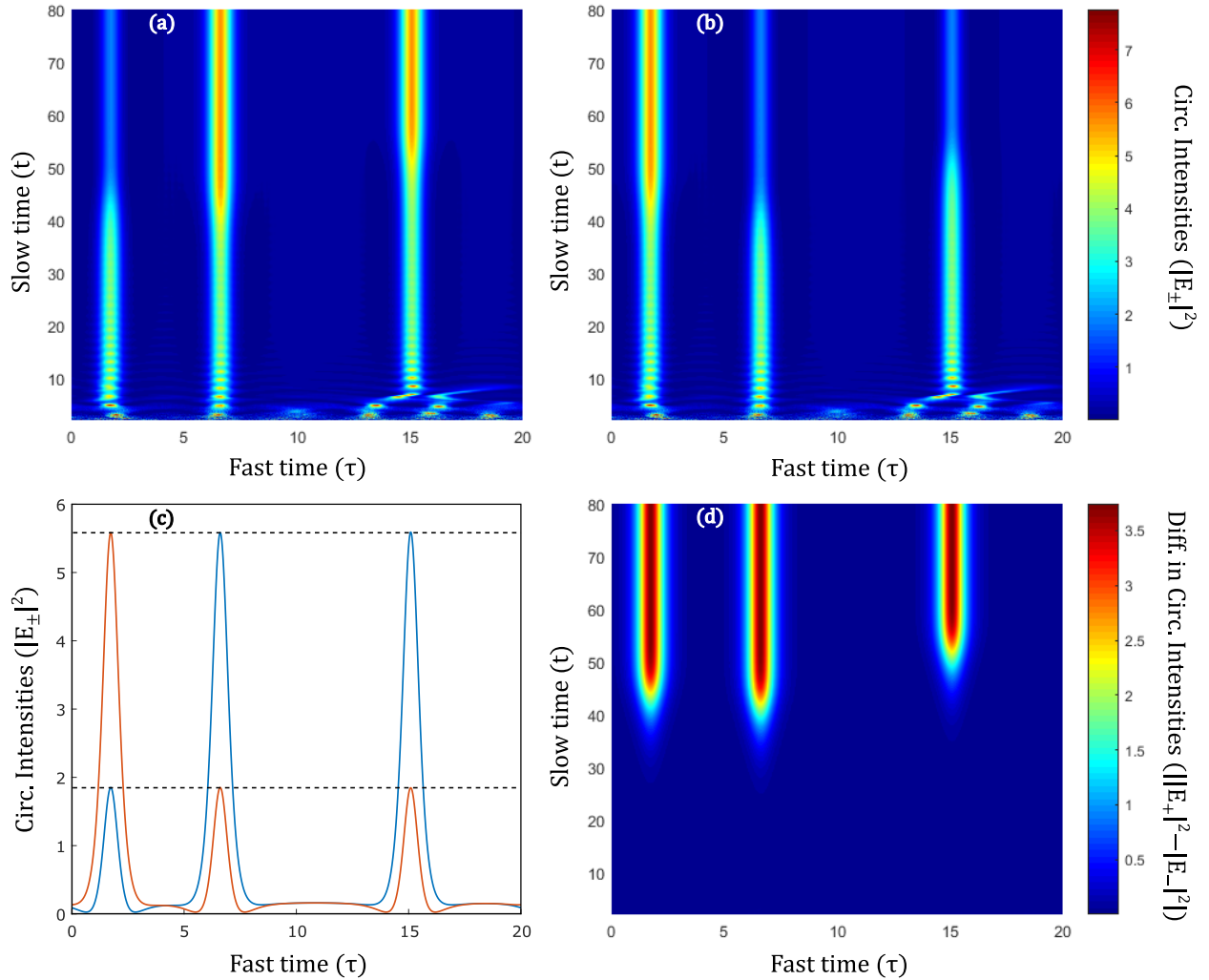
Figure 6.2: Symmetry broken TCS for $A = 1, B = 1.58, \theta = 4$ and $E_{in} = 1.5$.
(a,b) slow time the evolution of the two field components $|E_\pm|^2$ over 40,000 iterations starting from initial conditions with adequately large non-homogeneous random perturbations, with (c) showing the final fast-time profiles. (d) Differences observed between the two field component intensities over the evolution.

With asymmetric TCS observed for a single detuning value the question
was raised as to whether we could observe the actual bifurcation point of spon-
taneous symmetry breaking, the transition point from symmetric to asymmet-
ric solitons. To best fit with the experimental methods, numerical integra-
tions were preformed which scanned the cavity detuning parameter. Figure
6.3 shows, again with parameters which were chosen to mimic those used in
the later experiments of Ref. [88], a scan from low, $\theta = 2$, to high, $\theta = 8$,
cavity detuning, where the final stage of the previous cavity detuning is used
as the initial condition for the next cavity detuning value integration. As
in scalar systems, the intracavity fields initially, $\theta < 3.1$, are unstable to a
Turing-like modulation instability that results in the formation of dissipative
patterns that fill the entire system. Despite their complex dynamics, we find
that the patterned states are (predominantly) identical across the two modes,
$|E_+|^2 = |E_-|^2$ see panel (c), although this symmetry later begins to break at
$\theta = 2.6$, dashed line (1). When the detuning increases beyond $\theta > 3.1$, dashed
line (2), localised CSs emerge from the patterned state. (c) shows that at this
point the profiles of the TCS have a very strong asymmetry and thus corre-
spond to mirror-like polarization states. As the detuning increases further,
beyond $\theta > 6.5$, dashed line (3), the symmetry of the solitons is recovered,
thus observing the SSB bifurcation point, which continue until the symmetric
solitons become unstable at around $\theta = 7.16$, dashed line (4).

Similarly, we may produce a clearer observation of the bifurcation point by
tracking only the peak of a TCS. Figure 6.4 starts from the initial conditions of
a symmetric TCS, produced from some earlier scan, at the high detuning limit
of the soliton's stability, $\theta = 7.16$. The detuning was then gradually reduced
in steps of 0.01, where at each stage the system was given time to stabilise
before the peaks of the two TCSs were recorded. One can see that at around
$\theta = 6.5$, the two symmetric solitons spontaneously break their symmetry and
suddenly one soliton peak becomes dominant over the other.

The spontaneous symmetry breaking of the TCS may be claimed to be
analogous to that of the HSS, with the pitchfork bifurcation clearly shown; once
again with the branch of the symmetric TCSs becoming unstable (generated by
the same method as above but with $E_+ = E_-$ enforced), but in this context,
we must emphasise that the soliton symmetry breaking does not require a
simultaneous breaking of the (corresponding) symmetry of the homogeneous
state. Results in Fig. 6.4 were in fact obtained using a driving power that is
below the threshold of SSB of the homogeneous state [57,120]. This is because
the local peak of the soliton operates with intensities higher than that which
are experienced by the HSS.

There may have been some surprise with observation of Fig. 6.4 at the
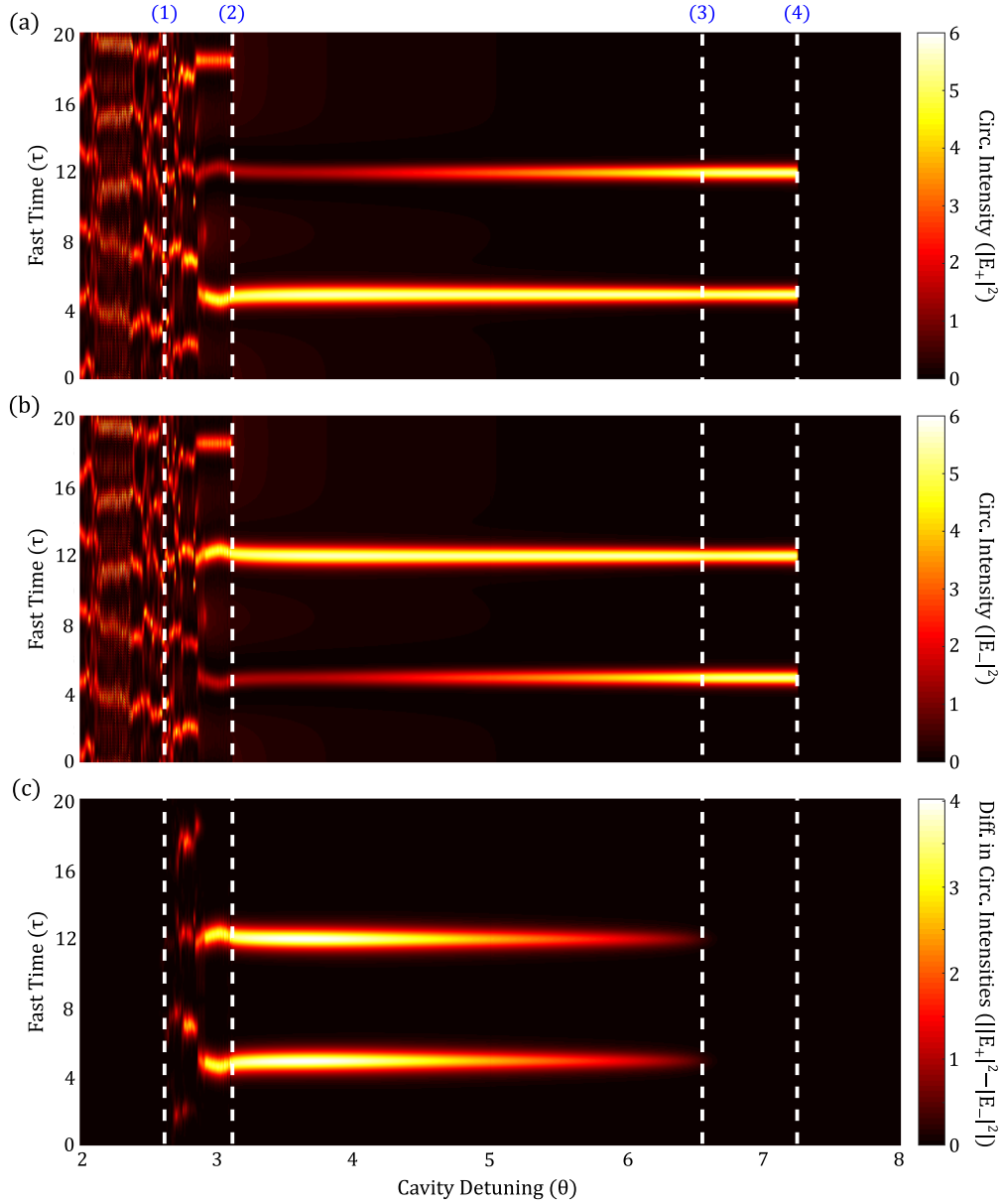
Figure 6.3: Fast time intensity profiles for the two field components $E_{\pm}$, (a) and (b) respectively, are plotted for a scan of the cavity detuning for $A = 1, B = 1.58$, and $E_{in} = 1.5$. (c) Difference between the fast time intensity profiles. Dashed line (1) shows the point at which symmetric MI becomes asymmetric, (2) shows the point where asymmetric solitons emerge from the pattern state, (3) shows the symmetry restoring bifurcation leading to symmetric TCS and (4) shows the point where these TCS become unstable.
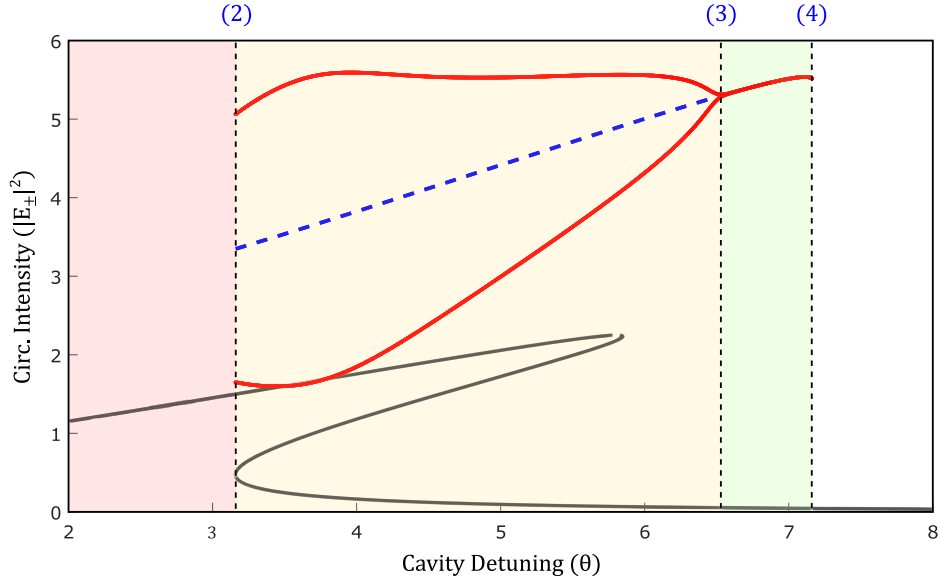
Figure 6.4: A scan of the cavity detuning while tracking the peaks of the TCS structures present in each of the field intensities $|E_\pm|^2$. For $A = 1$, $B = 1.58$, $E_{in} = 1.5$. The scan starts from $\theta = 7.16$ with a pregenerated symmetric TCS which is allowed to evolve until stable, at which point the detuning is gradually reduced, at each stage allowing for the system to re-stabilise. The red line tracks the peaks of the two TCS with no forced symmetry where as the dashed blue line tracks the system with a forced $E_+ = E_-$ symmetry. HSS in black. Green background shows the region with symmetric TCS, yellow with asymmetric TCS and red shows the system falling to MI. Dashed lines (2-4) are defined the same as defined in Fig. 6.3

abrupt end of the dashed blue and red curves which track the peaks of the (symmetric and asymmetric) TCS peaks. This ending is explained by the recollection that the soliton base sits on the lower branch of the HSS. The HSS for the relevant parameters is also plotted on Fig. 6.4 and it is clear to see that the point at which the solitons become unviable coincides exactly with the HSS's turning point, where the bistability ends and of course there is no longer a bottom branch for the soliton to sit, $\theta = 3.16$. In Ref. [88] it is shown that the solitons lock to a particular modulation instability pattern, patterns that are, as seen in Fig. 6.3, continuous past the HSS bistability cut off. This cut off prevents the full 'bubble' of asymmetric solitons being plotted, however one sees in Ref. [88] that the inclusion of pattern states, generated using a Newton-Raphson relaxation algorithm [175] allows for both the symmetry breaking and symmetry-restoring bifurcations to be seen.

Many further, experimental, results on symmetry broken solitons are reported in [88], such as their manipulation in switching the dominant and suppressed soliton states.

6.3 Breathing Dynamics of Symmetry Broken TCS

The previous section of this chapter verified that the SSB phenomenon was indeed applicable to pattern and soliton solutions. This realisation then opened up many questions as to whether the other results and discussions outlined in Chapters 3-4 were also relevant to TCS and if these could be used to create novel behaviours. For example, with the knowledge that there are regions of some symmetry broken bubbles of the homogeneous solutions where the system is susceptible to oscillations, could similar oscillations occur with the new symmetry broken TCS? Solitons with an oscillating peak are described as 'breathing', and an investigation into possible breathing symmetry broken TCS was further encouraged since breathing dissipative solitons in optical microresonators have already been observed in Ref. [138].

Utilizing the findings from Section 3.3, primarily the understanding that the homogeneous states of Eq. (6.2) have a stronger susceptibility to growing oscillations as the input intensity is increased, a scan similar to Fig. 6.4 was completed at the higher input pump of $E_{in} = 2.1$, this is shown in Fig. 6.5.

Figure 6.5 once again tracks the peaks of the solitons in each of the fields $E_\pm$, now with red and blue lines respectively, but now under the condition that if the peak of the soliton is unstable, i.e. it is oscillating in some manner, then the red and the blue lines plot the edges of the range of these oscillations, their maxima and minima intensities. The scan again started with the initial conditions of a pre-simulated stable symmetric soliton at the high detuning limit of soliton stability, at approx. $\theta = 14$ in this case, and in a step-wise fashion the detuning is decreased, at each stage allowing the system time to adapt to this new detuning value. With an appropriate relaxation period allowed, the peaks are then tracked for an appropriate time in order to build up a picture of their behaviour.

It can be seen in the results of Fig. 6.5 that such a scan can result in four distinct regions of soliton behaviour, which is indicated by various background shading. Two of these regions are known from the previous section: green shading shows the region where the symmetric TCSs reside, and the pink shading shows the stable asymmetric TCSs. The two new regions of Fig. 6.5 are shaded in blue and purple, and while both these regions indicate breathing
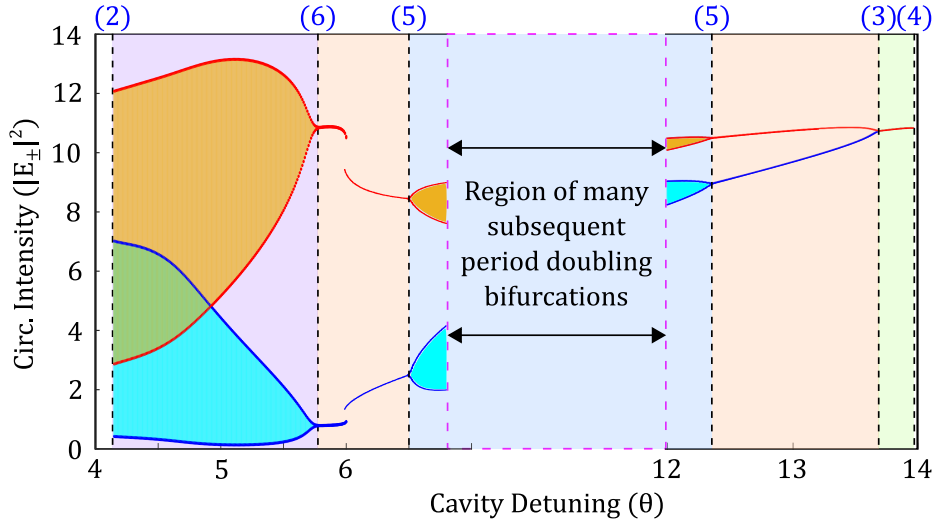
Figure 6.5: Range of TCS peak power levels of the two polarisation components of numerically simulated TCSs versus cavity detuning θ for $E_{\mathrm{in}} = 2.1$ and $B = 1.6$. Blue and red curves indicate the limits of peak breathing with the full range in gold and cyan, green for overlap. Background colour: green – symmetric TCSs; Pink – stable SB TCSs; Purple – in-phase SB breathers; Blue – out of phase SB breathers. Within the blue region, 'deep' breathers exist, which can lead to periodic or chaotic switching of the dominant and suppressed fields. Dashed lines (2-4) are the same as defined in Fig. 6.3 where as (5,6) define the limits of anti-phase and in-phase breathing respectively.

solitons, they differ since in the blue region the breathing dynamics favour being out of phase with each other, while in the purple region the breathing dynamics occur in phase. These regions have their boundaries defined by Hopf bifurcations which indicate the start of peak oscillations, dashed lines (5) and (6). Examples of the soliton peak oscillatory evolutions are shown in Fig. 6.6, with some early experimental verification of these symmetry broken breathing dynamics for fiber loops being shown in Fig. 6.7, as reported in Ref. [176].

Within the blue region of Fig. 6.5 there is an internal region, which is computationally intensive to model, where, similar to the dynamics of the homogeneous fields, many subsequent period doubling bifurcations occur leading to very complex and even chaotic breathing dynamics. Due to the sizeable interruptions at time of writing caused by the COVID-19 pandemic both theoretical and experimental research into this region is ongoing, but Fig. 6.6 (c) provides an example of 'deep' breathing solitons, where the range of the breathing dynamics of the two fields completely over lap, reminiscent of the
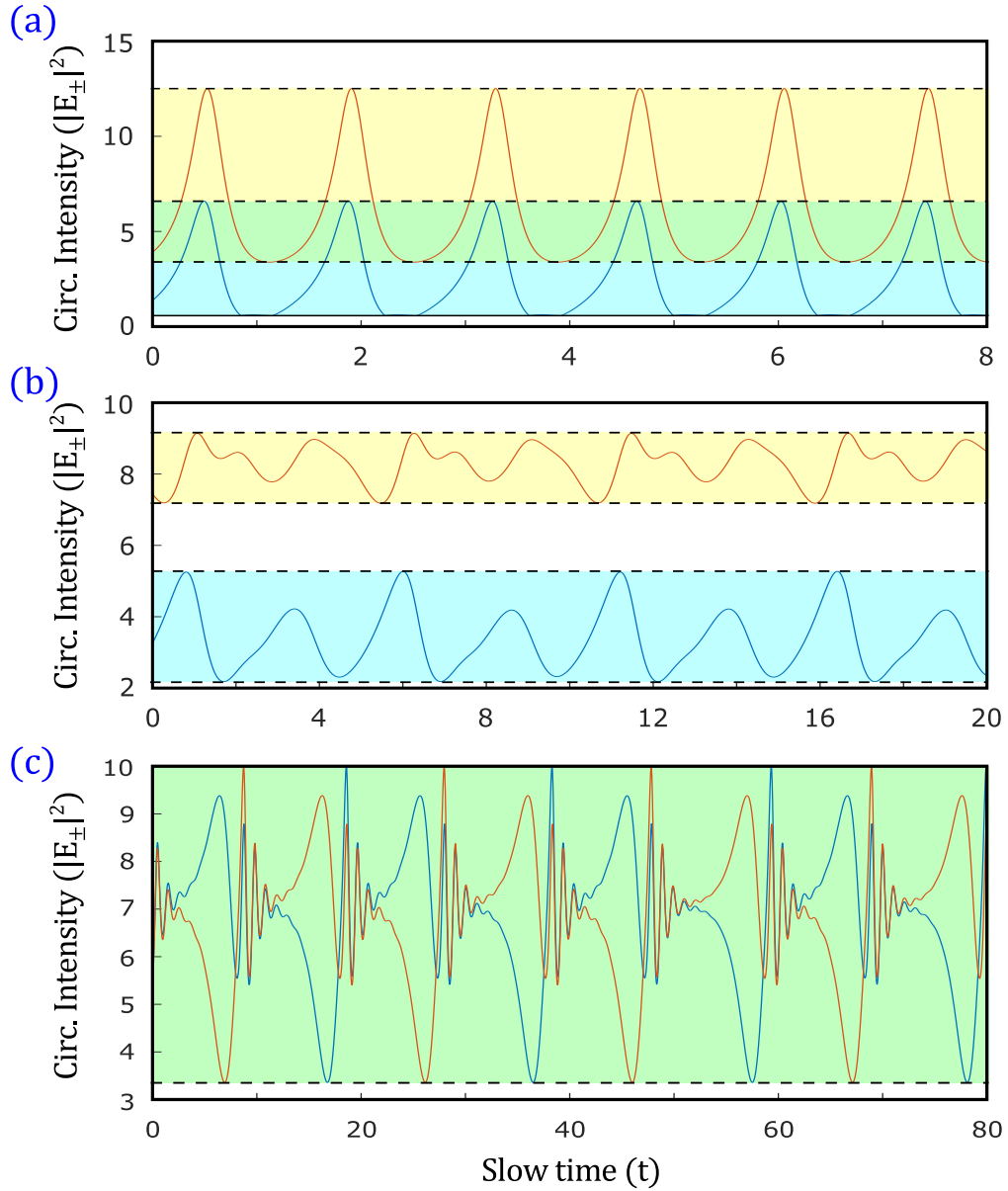
Figure 6.6: Breathing soliton dynamics for various detuning values by tracking
TCS peak intensities. For all $A = 1$, $B = 1.58$, $E_{in} = 2.1$. For (a) $\theta = 4.5$,
residing in the purple region of Fig. 6.5, and shows close to in-phase dynamics.
For (b,c), $\theta = 7.05$ and 8.1579 respectively which both reside in the blue
region of Fig. 6.5 which is characteristic of closer to anti-phase dynamics -
most obviously seen in the relatively simple dynamics of (b). (c) shows that
periodic switching dynamics are also possible for breathing solitons.

green region of Fig. 4.5, and there is the opportunity of observing the interesting phenomenon of spontaneous periodic switching of the dominant and suppressed breathing solitons.
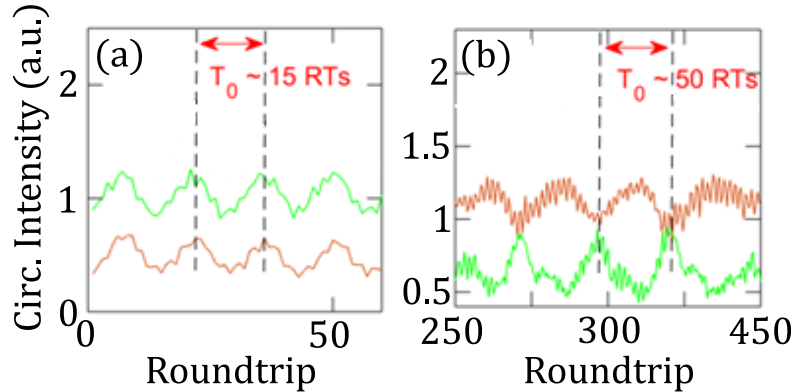
Figure 6.7: Preliminary and unpublished results of experiments performed at $A = 1$, $B = 1.58$, $E_{in} = 2.1$ with $\theta = 5.2$ and $\theta = 8$ for (a,b) respectively. The green and orange lines track the soliton peaks of the two field components respectively. (a) shows the peak evolution for a detuning in the purple region of Fig. 6.5 and confirms a close to in-phase relationship between the two fields. (b) on the other hand shows the evolution for a detuning in the blue region of Fig. 6.5 and confirms a more anti-phase relationship between the two fields. Experiment performed, and figure supplied, by Gang Xu [176, 177]. Details of experiment can be found in Ref. [37]. We have no claim over this experimental work, it is included only to provide comparison with theoretical predictions.

6.4 Chapter Summary

In this chapter we began by independently verifying the existence of temporal cavity solitons in a system described by a single LLE which is recovered from our studied coupled systems when enforcing that $E_+ = E_-$. We employed a combination of split-step Fourier and Runge-Kutta integration methods to show that these symmetric soliton profiles may naturally emerge from initial conditions containing adequately large non-homogeneous random perturbations, without any further required engineering.

Following this symmetric soliton observation we proceeded to remove the condition of forced symmetry and allowed the system to again naturally evolve for the same input conditions which resulted again in the formation of soliton

field profiles however now the two field profiles were asymmetric with the emergence of dominant and suppressed solitons similar to the phenomena observed for the homogeneous studies of previous chapters.

To observe the symmetry breaking bifurcation points of the symmetric TCS two detuning scans were simulated. One observed the full fast time profiles of the two field components and showed how unstable Turing-like pattern states may evolve within the system which beyond a certain detuning parameter may form asymmetric TCS. These asymmetric TCS may later restore their symmetry when passing a second detuning limit. A second scan showed this behaviour in a clear bifurcation diagram by tracking only the peaks of the TCS.

Finally preliminary investigations were described into the possibility of breathing dynamics occurring, where the fast-time symmetry broken soliton structures may begin to oscillate over slow-time. It was shown that this could occur in two distinct regions, in one region the fields evolved in a more in-phase manner while in the second the fields were more closely linked to anti-phase descriptions, these results were compared to experimental results from collaborators verifying their validity. It was further shown that theoretically symmetry-broken TCS would breath in complex ways with the potential for the periodic switching of the dominant and suppressed roles held by each of the two field components.

*"Science knows no country,
because knowledge belongs to humanity,
and is the torch which illuminates the world"*

– Louis Pasteur

Chapter 7

Additional Results on Symmetry Breaking in Kerr Ring Resonators

Contents

In this final chapter, for completeness, we discuss two further issues related
to symmetry breaking in nonlinear optical resonators. The first set of results
outlined here were presented by ourselves for useful discussion with the authors
of the paper 'Asymmetric balance in symmetry breaking' [37]. The second
section of this chapter concerns a model combining both counter-propagation
and field polarisation.

7.1 Bifurcation Restoration from the Balancing of Asymmetric Inputs

With our normal set of coupled equations describing homogeneous fields:

$$\frac{\partial E_\pm}{\partial t} = E_{in} + \left[-1 + i(A|E_\pm|^2 + B|E_\mp|^2 - \theta) \right] E_\pm, \tag{7.1}$$

both the two terms describing the input pumps, E_{in}, and two describing the
cavity detuning, θ, were respectively equal to one another for each of the two
fields. This situation may be referred to as having symmetric input parame-
ters. There is however no requirement in general for the input parameters to
be equal, one input beam could have a higher intensity than the other, or one
input beam could have a different cavity detuning to the second. By intro-
ducing an initial imbalance to the system, say to the input pump, we may try
to restore some typical features of the the symmetric-input system, such as
the pitchfork bifurcation indicative of spontaneous symmetry breaking, with
a second imbalance, say in the cavity detuning.

To study the impact of unbalanced input conditions, we use equations
adapted from Eq. (7.1) to describe the system

$$\frac{\partial E_+}{\partial t} = \sqrt{X} \cos\chi + \left[-1 + i(A|E_+|^2 + B|E_-|^2 - \theta_+) \right] E_+, \tag{7.2}$$

$$\frac{\partial E_-}{\partial t} = \sqrt{X} \sin\chi + \left[-1 + i(A|E_-|^2 + B|E_+|^2 - \theta_-) \right] E_-, \tag{7.3}$$

where X represents the total pump power and the imbalances are introduced
through the value of χ (note that $\chi = 45°$ restores an equal pump power) and
$\theta_\pm$. We may also define, without loss of generality, $\theta_+ = \theta$, $\theta_- = \theta_+ - \delta\theta = \theta - \delta\theta$, such that $\delta\theta = 0$ implies symmetric cavity detuning $\theta_+ = \theta_-$ [37].

By the same method as outlined in Chapter 3, we begin by finding the
stationary states of Eq. (7.2)-(7.3). These are given by

$$X \cos^2(\chi) = |E_+|^2 \left[1 + \left(A|E_+|^2 + B|E_-|^2 - \theta \right)^2 \right] , \tag{7.4}$$

$$X \sin^2(\chi) = |E_-|^2 \left[1 + \left(A|E_-|^2 + B|E_+|^2 - \theta + \delta\theta \right)^2 \right] . \tag{7.5}$$

Proceeding to rearrange Eq. (7.4) to make $|E_-|^2$ the subject of the equation
and substituting the result into Eq. (7.5), one obtains the result given by Eq.
(7.6). A similar method may then be applied to Eq. (7.5) only now making
$|E_+|^2$ the subject, which may then be substituted into Eq. (7.4) yielding the
result given by Eq. (7.8).

$$X \sin^2(\chi) = y_1 \left[1 + \left(Ay_1 + B|E_+|^2 - \theta + \delta\theta \right)^2 \right] , \tag{7.6}$$

with

$$y_1 = \frac{\sqrt{\frac{X \cos^2(\chi)}{|E_+|^2} - 1} - A|E_+|^2 + \theta}{B} , \tag{7.7}$$

and similarly

$$X \cos^2(\chi) = y_2 \left[1 + \left(Ay_2 + B|E_+|^2 - \theta \right)^2 \right] , \tag{7.8}$$

with

$$y_2 = \frac{\sqrt{\frac{X \sin^2(\chi)}{|E_+|^2} - 1} - A|E_+|^2 + \theta - \delta\theta}{B} . \tag{7.9}$$

Equations (7.6)-(7.9) allow you to plot $|E_\pm|^2$ against either the input inten-
sity or the cavity detuning in a manner similar to Figs (3.5-3.6) respectively.
Figure 7.1 shows the results of intensity and detuning scans. (a) and (b) show
the intensity and detuning scans respectively with only one input parameter
imbalance, with $\chi = 53.5°$, and it is plain to see that in both scans there
is little resembling a pitchfork bifurcation between the two fields. In panels
(c) and (d) we implement a second imbalance, this time in the cavity detun-
ing ($\delta\theta = 0.73332$ and $\delta\theta = 0.632$ respectively) to restore that which at first
glance appears to be a pitchfork bifurcation of the form studied in previous
chapters. It is the restoration of this bifurcation point which we use to define
a 'balancing' of asymmetric inputs.

Note that our choices of parameters for Fig. 7.1, particularly for panel (d),
were influenced by the experiments of collaborators, results later presented in
Fig. 5 of Ref. [37]. We do not observe the exact experimental results presented
there but this is likely due to the extreme sensitivity of the system to inputs
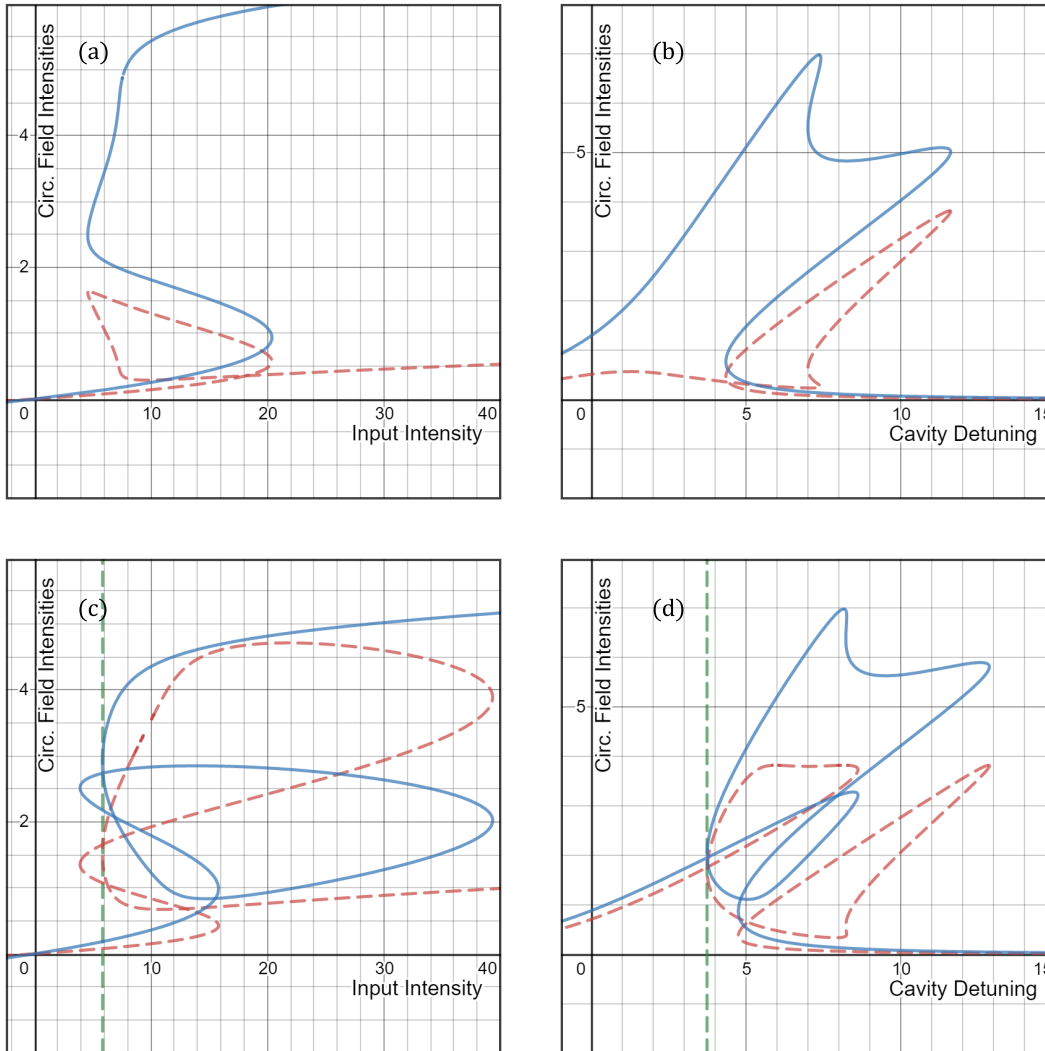
Figure 7.1: Intensity (a,c) and detuning (b,d) scans of Eq. (7.6)-(7.9), solid blue and dashed red respectively, for $A = 1, B = 1.57$, and with the initial imbalanced caused with $\chi = 53.5$. For the fixed common input in (a,c) $\theta = 5.45$, where as in (b,d) $X = 10.8$. In (a,b) no re-balancing is attempted, $\delta\theta = 0$, where as in (c,d) $\delta\theta = 0.73332$ and $\delta\theta = 0.632$ respectively, which restores a bifurcation point, marked with a dashed green line.
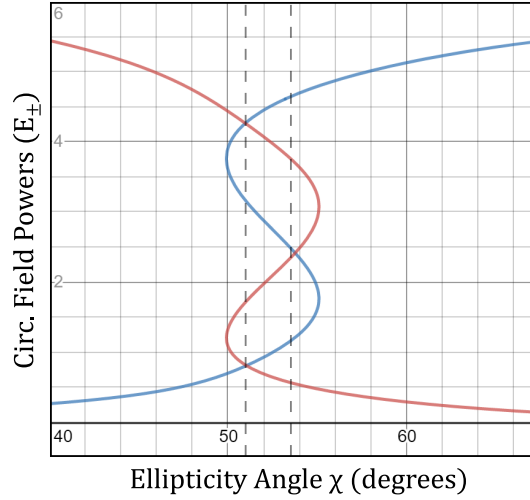
Figure 7.2: Equations (7.6)-(7.8) are used to plot the 'bubble' field intensities $E_\pm$ for a scan of the ellipticity angle χ. Here $A = 1$, $B = 1.57$, $\theta = 5.45$, $X = 10.8$ and $\delta\theta = 0.632$, which restore the bifurcation in 7.1(d). It is shown that under these parameters an ellipticity angle of approx. $51°$ momentarily restores mirror states between the two fields as observed experimentally in Ref. [37] at a slightly different ellipticity angle of $53.5°$.

and hence a small error in stated experimental parameters can cause a considerable difference in the system outcome. See our Fig. 7.2 for further theory comparison and agreement with Ref. [37].

Beginning to address the question of the type of bifurcation which is recovered, the first observation which immediately implies a difference between the restored bifurcation and the normal symmetry breaking pitchfork bifurcation previously studied comes from the very apparent fact, observe Fig. 7.1 once more, that there is no initial field intensity symmetry, $|E_+|^2 = |E_-|^2$, to break. That is to say the red and blue curves do not overlap for any extended period prior, or indeed after, the bifurcation, unlike in the similar Figs. 3.5-3.6. Although the bifurcations are not $|E_+|^2 = |E_-|^2$ symmetry breaking in nature, the question still remains as to if we restore two pitchforks bifurcations, all be it asymmetric to each other.

Figure 7.3 (a,b) show magnifications of the bifurcation points of the input intensity and cavity detuning scans of Fig. 7.1 (c,d) and there is the revelation that at the bifurcation point the gradient of the offshoot curve is not infinite; an important property of the normal $|E_+|^2 = |E_-|^2$ pitchfork bifurcation, Fig. 7.3 (c). The bifurcations seen in (a,b) with offshoot curves of non-infinite gradients are in fact more accurately modeled at a local level by a pitchfork
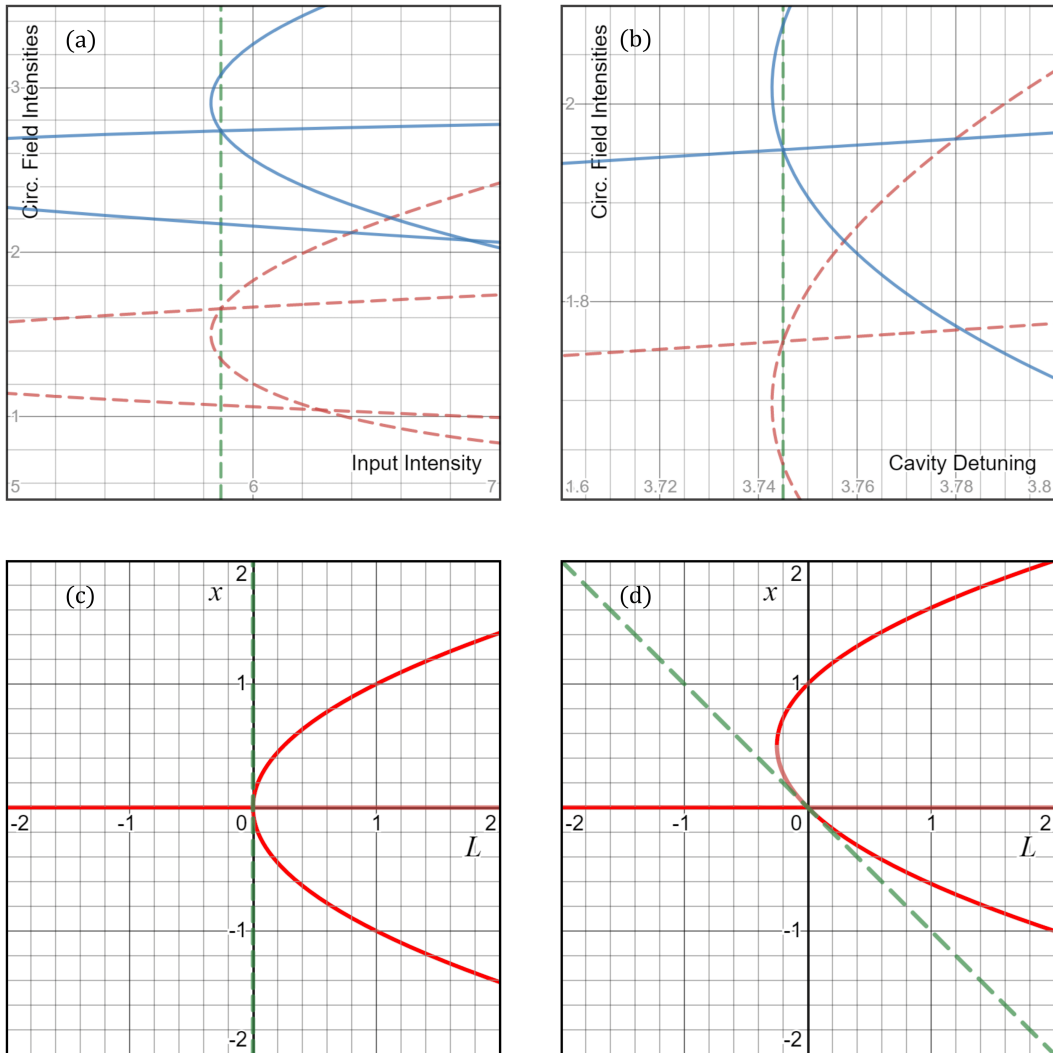
Figure 7.3: Bifurcation comparison. Panels (a,b) show zoomed in snapshots of the bifurcation in points Fig. 7.1 (a,b). Note the non-infinite gradient at the bifurcation point, uncharacteristic of the standard generic pitchfork bifurcation, panel (c). The bifurcations in (a,b) instead locally share their forms with a perturbed pitchfork bifurcation, panel (d). In (a,b) the green dashed lines show the x-axis value where the bifurcation takes place, whereas the green dashed line in (c,d) shows the gradient of the pitchfork's and perturbed pitchfork's offshoot curves at the bifurcation point.

bifurcation which has been perturbed, Fig. 7.3 (d). It is at this stage that momentarily we must address the mathematical theory of pitchfork bifurcations and their unfolding [37].

7.1.1   Universal Unfolding of the Pitchfork Bifurcation

We begin by introducing the equation which describes a standard pitchfork bifurcation,

$$P(x, L) = x^3 - Lx = 0 \ , \tag{7.10}$$

which was used by us to map out Fig. 7.3(c). Bifurcation theory states that the unfolding of a bifurcation occurs when the bifurcation function, here $P(x, L)$, is disturbed by some smooth perturbation [178–182], with the equation describing the universal unfolding of a bifurcation being one that gives all the essential types of bifurcations found in all unfoldings with the minimum number of variables. For a pitchfork bifurcation the universal unfolding, which yields all possible variants of imperfect pitchfork bifurcations, is given by

$$U(x, L, a, b) = P(x, L) + bx^2 + a \ , \tag{7.11}$$

where a, b are imperfection parameters. For a perfect pitchfork $a = b = 0$ and $U(x, L, a, b) = P(x, L)$.

Figure 7.4 is a phase diagram for the values of a, b of the universal unfolding of the pitchfork bifurcation, showing all possible forms of the imperfect pitchfork bifurcation, with the 'connected' perturbed pitchforks of the form seen in Fig. 7.3(d) being found along the line $a = 0$. If one therefor assumes that a, b are independent of one another, then an imbalance caused by the a-term can never be countered, thus restoring a connected pitchfork, by a second imbalance caused by the b-term.

If however we make the a-term instead a function of a, b, for example simply:

$$U(x, L, a, b) = P(x, L) + bx^2 + \tilde{a}(a, b) \ , \quad \tilde{a}(a, b) = a + b \ , \tag{7.12}$$

then it is now possible to shift the universal unfolding parameters to allow for asymmetry balancing, where we restore the connected perturbed pitchfork by balancing one asymmetric parameter b with a second a.

Figure 7.5 shows the new phase space of a, b for Eq. (7.12), with the connected perturbed pitchfork bifurcations now lying away from the $a = 0$ line and along the $\tilde{a} = 0$ line.
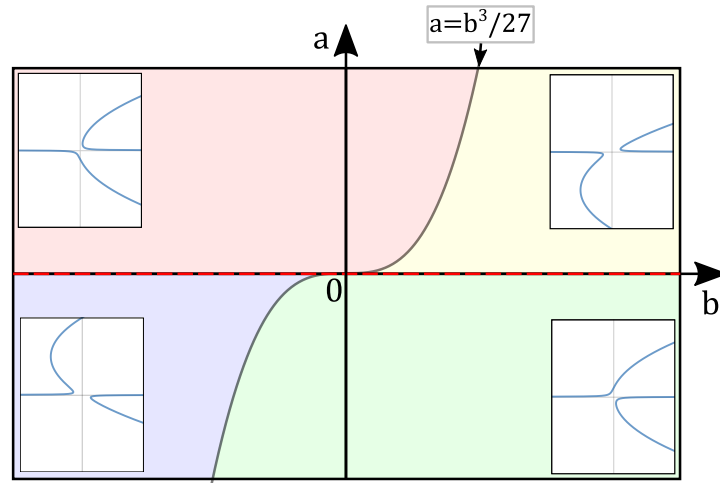
Figure 7.4: Phase space of the universal unfolding of the pitchfork bifurcation, showing all possible forms of the imperfect pitchfork bifurcation, Eq. (7.12). The dashed red line ($a = 0$) shows where the imperfect, but connected, pitchforks, as seen in Fig. 7.3(d), lie.
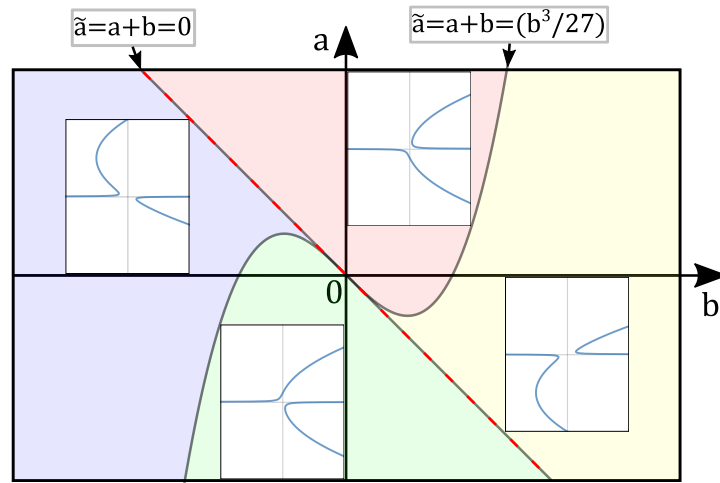
Figure 7.5: Phase space of the transformed universal unfolding of the pitchfork bifurcation, showing all possible forms of the imperfect pitchfork bifurcation Eq. (7.12). The dashed red line ($\tilde{a} = 0$) shows where the imperfect, but connected, pitchforks, as seen in Fig. 7.3(d), lie.

Returning discussions to our own studied system, the reason that we are able to restore a connected perturbed pitchfork bifurcation through the countering of one asymmetry χ with another, $\delta\theta$, is due to the underlying pitchfork being described by Eq. (7.12) with some, currently unknown, $\tilde{a}(\chi, \delta\theta)$.

We finish this section with the observation of the crossing of the $\tilde{a}(\chi, \delta\theta) = 0$ line for our system Eq. (7.6)-(7.8).

Figure 7.6 (similar for Fig. 7.7) shows the $\tilde{a}(\chi, \delta\theta) = 0$ crossing when scanning the cavity detuning (input intensity), with the top row of panels showing the HSS of Eq. (7.8) and the middle row showing the HSS of Eq. (7.6). For all panels of the figure a common imbalance in the input intensity $\chi = 48.5$ is present and this is countered with different cavity detuning imbalances $\delta\theta$ for each column.

In the far left column the cavity detuning imbalance under-compensates the input offset and this results in a disconnected perturbed pitchfork. When the pitchfork is disconnected, the system, which is assumed to have low noise, will always choose the same field to become dominant or suppressed during the scan, this is because the alternative role is inaccessible due to the disconnect (the bottom row of panels in the figure shows the selected path of each field). Similarly, the column second from left shows a better, but still under-compensating cavity detuning imbalance - again forcing field dominance or suppressed roles.

(Near) perfect compensation by the cavity detuning imbalance is finally seen in the middle column of Fig. 7.6, leading to a connected perturbed pitchfork bifurcation and thus implying that here $\tilde{a}(\chi = 48.5, \delta\theta \approx 0.26) = 0$ (Similarly seen in Fig. 7.7 for $\delta\theta \approx 0.31$). This leads to the possibility of either role, dominant or suppressed, being taken by either field since even minimal noise will be enough for the system to be attracted to either stable branch of the pitchfork due to the connected unstable middle branch.

Moving on to the right two columns of the Fig. 7.6 and 7.7, the cavity detuning imbalance now over-compensates the input offset, once again breaking the connection of the perturbed pitchfork and leaving only one path viable for the system to follow.

If there is enough noise within the system then it is possible for the system to jump to the alternate path, even when the perturbed pitchfork is not connected, observed experimentally in Ref. [37]. The requirement of this activation energy in the form of adequate noise within the system would be an important consideration for development of devices looking to utilise both field roles but who are unable to achieve a perfect balancing of the asymmetric inputs.
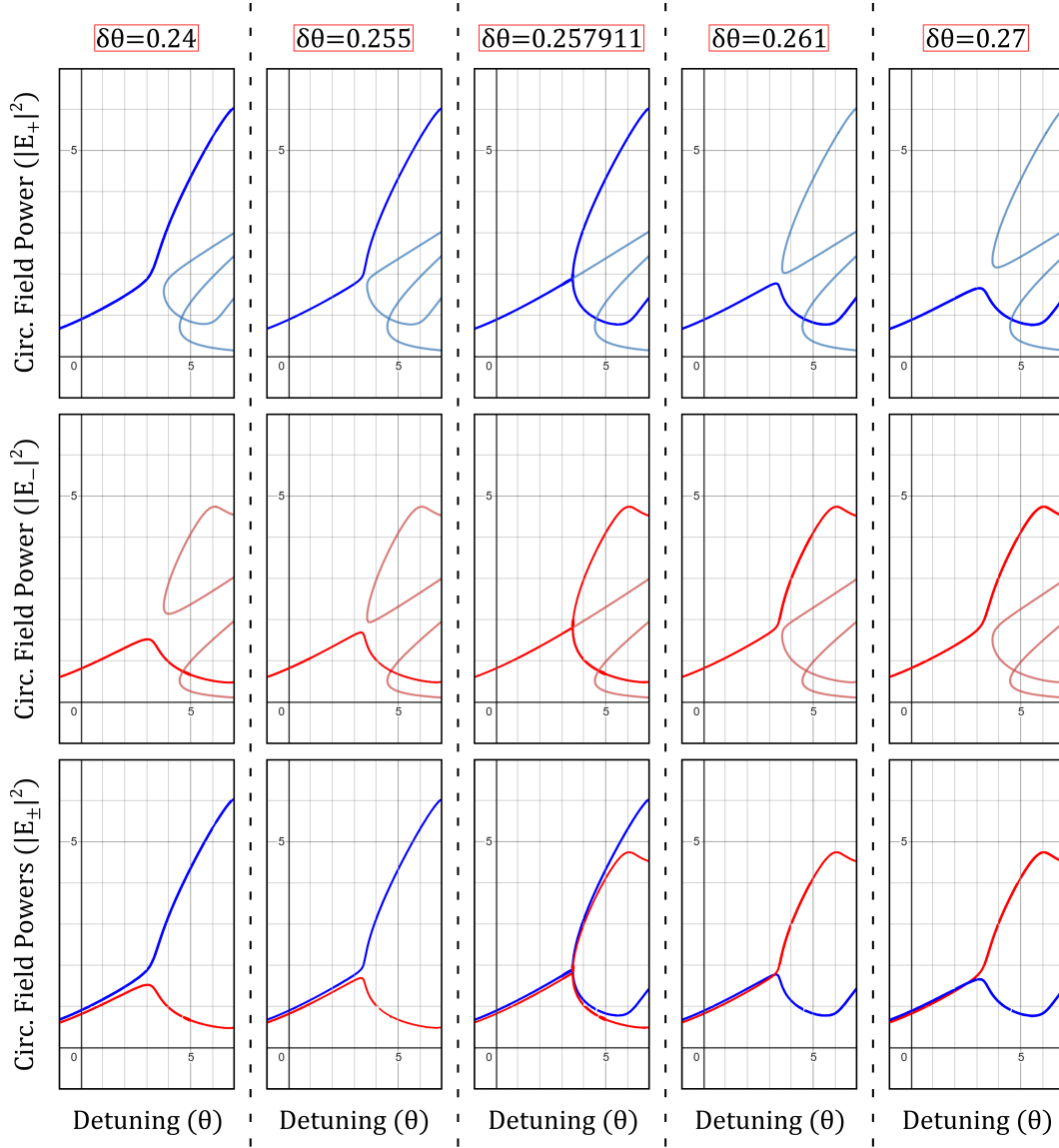
Figure 7.6: Various cavity detuning scans, θ, of Eq. (7.6) and Eq. (7.8) with imbalances in both input conditions. For all $A = 1$, $B = 1.57$, $\chi = 48.5$, $X = 10.8$. The top row of panels shows the HSS of Eq. (7.8), shown in blue, while the middle row shows the HSS of Eq. (7.6), in red. The columns of panels relate to a common value of the detuning imbalance, $\delta\theta$, with the respective values shown at the top of the column. Highlighted in bold blue and red are the paths that the system will take when scanning from low to high detuning. For clear viewing these bold paths, for both fields, are repeated in isolation from the other HSS on the bottom row.
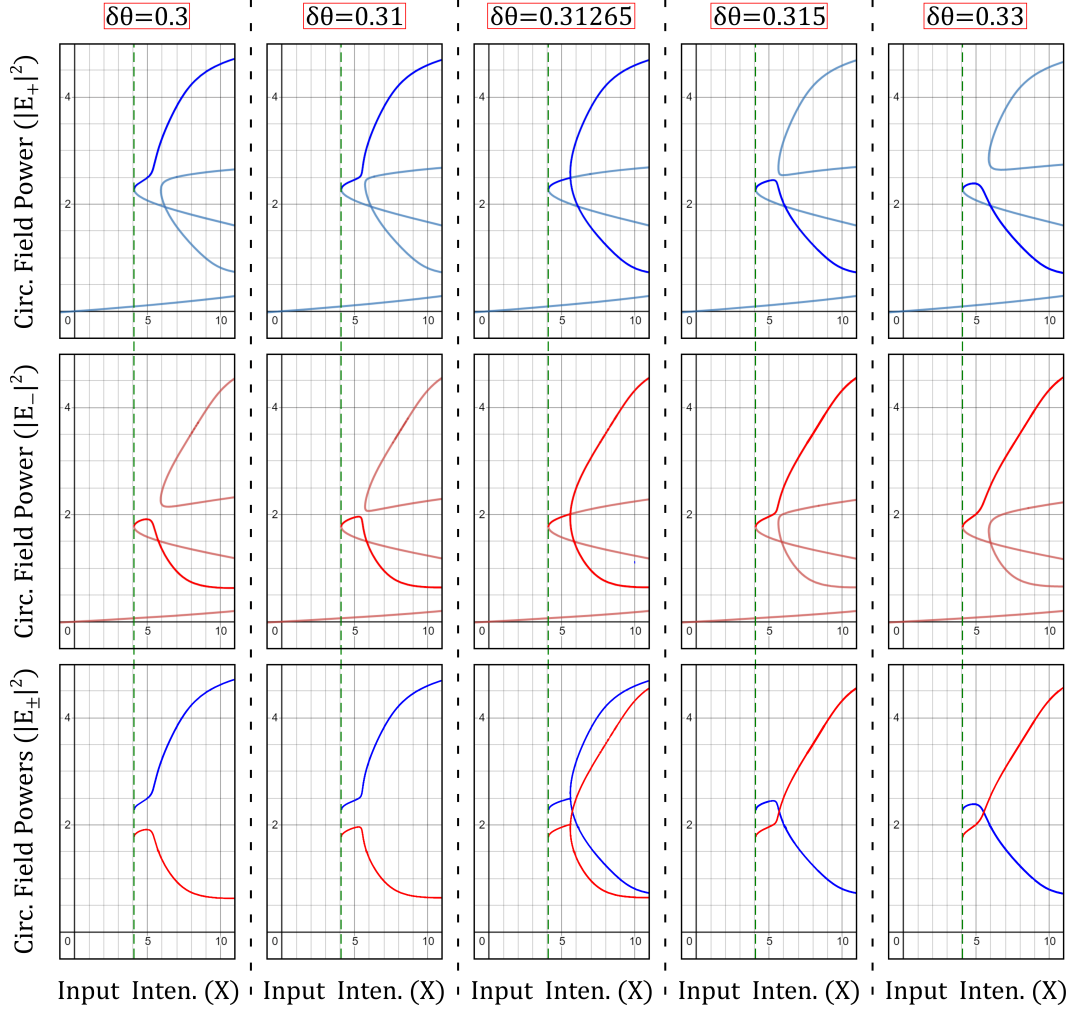
Figure 7.7: Various input intensity scans, X, of Eq. (7.6) and Eq. (7.8) with imbalances in both input conditions. For all $A = 1$, $B = 1.57$, $\chi = 48.5$, $\theta = 5.45$. The top row of panels shows the HSS of Eq. (7.8), shown in blue, while the middle row shows the HSS of Eq. (7.6), in red. The columns of panels relate to a common value of the detuning imbalance, $\delta\theta$, with the respective values shown at the top of the column. Highlighted in bold blue and red are the paths that the system will take when scanning from low to high input intensity. For clear viewing these bold paths, for both fields, are repeated in isolation from the other HSS on the bottom row. Note that the bold path assume the two field intensities are beginning the scan on the top branches of their respective s-shaped bistabilities.

7.2 Nested Symmetry Breaking - a Combined Model of both Circular Polarizations and Counter-propagation Direction

The two systems which have been extensively studied throughout this thesis
are two counter-propagating linearly polarised fields and two co-propagating
circularly polarised fields, both circulating a Kerr ring resonator. The two
systems both yield fruitful fields of study due to the complexity of the system
dynamics, yet there is the opportunity to further expand the scope of results
by asking one simple question: what if the two counter-propagating fields had
two orthogonally polarised components - i.e. what would happen if the two
systems were combined?

The interaction between two counter-propagating quasi-monochromatic
beams in an isotropic dielectric with Kerr nonlinearity has nonlinear com-
ponents of the polarization along the x and y directions expressed by:

$$
\begin{aligned}
P_{x,y} = {} & (\chi_{xxyy} + \chi_{xyxy} + \chi_{xyyx})\,|E_{x,y}|^2 E_{x,y} \\
& + (\chi_{xxyy} + \chi_{xyxy})\,|E_{y,x}|^2 E_{x,y} + \chi_{xyyx}E_{y,x}^2 E_{x,y}^*,
\end{aligned}
\tag{7.13}
$$

[183], where χ is the third-order susceptibility tensor and $E_{x,y}$ are the total
field envelopes along the x and y axis respectively. In the case of silica glass
fibers, where $\chi_{xxyy} \simeq \chi_{xyyx} \simeq \chi_{xyxy} \simeq \chi_{xxxx}/3$, Eq. (7.13) reduces to

$$
P_{x,y} = \chi_{xxxx}\left(|E_{x,y}|^2 E_{x,y} + \frac{2}{3}|E_{y,x}|^2 E_{x,y} + \frac{1}{3}E_{y,x}^2 E_{x,y}^*\right).
\tag{7.14}
$$

Jumping into the midpoint of the derivation contained within Ref. [33], a
combined model can then be derived through the substitution of Eq. (7.14)
in place of equation (2.1) of Ref. [33], which in the first instance leads to the
following coupled equations:

$$
\begin{aligned}
\frac{\partial E_x}{\partial t} &= \sqrt{2}\epsilon_0 - E_x - i\theta E_x + i\left(|E_x|^2 E_x + \frac{2}{3}|E_y|^2 E_x + \frac{1}{3}E_y^2 E_x^*\right)\,, \\
\frac{\partial E_y}{\partial t} &= -E_y - i\theta E_y + i\left(|E_y|^2 E_y + \frac{2}{3}|E_x|^2 E_y + \frac{1}{3}E_x^2 E_y^*\right)\,.
\end{aligned}
\tag{7.15}
$$

To include both propagation directions the following expansion of the total
field envelope **E** is then required:

$$\mathbf{E} = E_x\hat{\mathbf{x}} + E_y\hat{\mathbf{y}}$$
$$= \begin{pmatrix} E_x \\ E_y \end{pmatrix} = \begin{pmatrix} E_{x1}e^{ikz} + E_{x2}e^{-ikz} \\ E_{y1}e^{ikz} + E_{y2}e^{-ikz} \end{pmatrix} \tag{7.16}$$

and, saving the reader from some lengthily algebra, one may then proceed to
expand all terms of Eq. (7.15) in terms of $E_{x1}, E_{x2}, E_{y1}, E_{y2}$, negate the fast
varying terms which emerge, and collate all terms of $E_{x1}, E_{x2}, E_{y1}, E_{y2}$ into
separate equations. One may then finally arrive at the set of four coupled
equations (7.18)-(7.21), on the next page.

It is however possible to simplify Eqs (7.18)-(7.21) by following a process
similar to that described in Ref. [33], i.e. moving from a linear basis to a
circular one by defining:

$$u_1 = \frac{E_{x1} + iE_{y1}}{\sqrt{2}}, \qquad u_2 = \frac{E_{x1} - iE_{y1}}{\sqrt{2}},$$
$$v_1 = \frac{E_{x2} + iE_{y2}}{\sqrt{2}}, \qquad v_2 = \frac{E_{x2} - iE_{y2}}{\sqrt{2}}. \tag{7.17}$$

Again saving the reader from lengthily algebra, one can substitute Eqs
(7.18)-(7.21) into Eqs (7.17) and simplify appropriately to obtain the much
simpler set of equations, Eqs (7.22)-(7.25).

Unfortunately, owed to the inclusion of the complex conjugate terms within
the nonlinear components present in Eqs (7.22)-(7.25), it is not trivial to obtain
the set of all possible homogeneous stationary solutions, even by the method
previously employed. We can however still study how the system evolves from
some set of initial conditions by the Runge-Kutta method of integration.

Figure 7.8 shows one such evolution of Eq. (7.22)-(7.25), with the addition
of a small amount of random noise, for $\theta = 3.85$, $\epsilon_0^2 = 1.3$, and initial conditions
$u_{1,2}, v_{1,2} = 1 + i0$. Remarkably this figure shows that the system breaks its
symmetry twice, leading to final field intensities with four entirely different
stable values. It can be seen in Fig. 7.8(a) that initially the system is attracted
to the purely symmetric attractor before rapidly evolving away (similar to the
two field model), but rather than evolving to settle, the system is attracted
to a second attractor - one which forms the previously unobserved state of
two symmetric field intensities and two asymmetric. This attractor is also
unstable and hence the system once again evolves away from the attractor
before finally settling in the stable purely asymmetric state where all field
intensities are different. Fig. 7.8(b) shows the field intensities during this
evolution.

Allowing for Field Polarisation in the Counter-propagating Model (Linear Basis)

$$\frac{\partial E_{x1}}{\partial t} = \sqrt{2}\epsilon_0 - E_{x1} - i\theta E_{x1}$$
$$+ i\left[|E_{x1}|^2 E_{x1} + 2|E_{x2}|^2 E_{x1} + \frac{2}{3}\left(|E_{y1}|^2 E_{x1} + |E_{y2}|^2 E_{x1} + E_{y1}E_{y2}^* E_{x2}\right) + \frac{1}{3}\left(E_{y1}^2 E_{x1}^* + 2E_{y1}E_{y2}E_{x2}^*\right)\right] \tag{7.18}$$

$$\frac{\partial E_{x2}}{\partial t} = \sqrt{2}\epsilon_0 - E_{x2} - i\theta E_{x2}$$
$$+ i\left[|E_{x2}|^2 E_{x2} + 2|E_{x1}|^2 E_{x2} + \frac{2}{3}\left(|E_{y2}|^2 E_{x2} + |E_{y1}|^2 E_{x2} + E_{y2}E_{y1}^* E_{x1}\right) + \frac{1}{3}\left(E_{y2}^2 E_{x2}^* + 2E_{y1}E_{y2}E_{x1}^*\right)\right] \tag{7.19}$$

$$\frac{\partial E_{y1}}{\partial t} = -E_{y1} - i\theta E_{y1}$$
$$+ i\left[|E_{y1}|^2 E_{y1} + 2|E_{y2}|^2 E_{y1} + \frac{2}{3}\left(|E_{x1}|^2 E_{y1} + |E_{x2}|^2 E_{y1} + E_{x1}E_{x2}^* E_{y2}\right) + \frac{1}{3}\left(E_{x1}^2 E_{y1}^* + 2E_{x1}E_{x2}E_{y2}^*\right)\right] \tag{7.20}$$

$$\frac{\partial E_{y2}}{\partial t} = -E_{y2} - i\theta E_{y2}$$
$$+ i\left[|E_{y2}|^2 E_{y2} + 2|E_{y1}|^2 E_{y2} + \frac{2}{3}\left(|E_{x2}|^2 E_{y2} + |E_{x1}|^2 E_{y2} + E_{x2}E_{x1}^* E_{y1}\right) + \frac{1}{3}\left(E_{x2}^2 E_{y2}^* + 2E_{x1}E_{x2}E_{y1}^*\right)\right] \tag{7.21}$$

**Allowing for Field Polarisation in the Counter-propagating Model
(Circular Basis)**

$$
\begin{aligned}
\frac{\partial u_1}{\partial t} = {}& \epsilon_0 - u_1 - i\theta u_1 \\
& + i\frac{2}{3}\left(|u_1|^2 u_1 + 2|u_2|^2 u_1 + 2|v_1|^2 u_1 + 2|v_2|^2 u_1 + 2v_1 v_2^* u_2\right)
\end{aligned}
\tag{7.22}
$$

$$
\begin{aligned}
\frac{\partial u_2}{\partial t} = {}& \epsilon_0 - u_2 - i\theta u_2 \\
& + i\frac{2}{3}\left(|u_2|^2 u_2 + 2|u_1|^2 u_2 + 2|v_2|^2 u_2 + 2|v_1|^2 u_2 + 2v_2 v_1^* u_1\right)
\end{aligned}
\tag{7.23}
$$

$$
\begin{aligned}
\frac{\partial v_1}{\partial t} = {}& \epsilon_0 - v_1 - i\theta v_1 \\
& + i\frac{2}{3}\left(|v_1|^2 v_1 + 2|v_2|^2 v_1 + 2|u_1|^2 v_1 + 2|u_2|^2 v_1 + 2u_1 u_2^* v_2\right)
\end{aligned}
\tag{7.24}
$$

$$
\begin{aligned}
\frac{\partial v_2}{\partial t} = {}& \epsilon_0 - v_2 - i\theta v_2 \\
& + i\frac{2}{3}\left(|v_2|^2 v_2 + 2|v_1|^2 v_2 + 2|u_2|^2 v_2 + 2|u_1|^2 v_2 + 2u_2 u_1^* v_1\right)
\end{aligned}
\tag{7.25}
$$
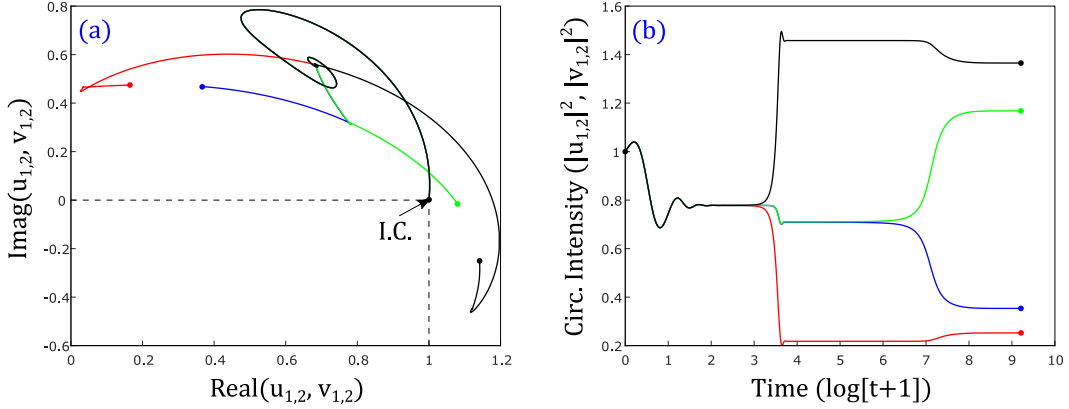
Figure 7.8: Temporal evolutions of Eq. (7.22)-(7.25) from initial conditions
of $u_{1,2}, v_{1,2} = 1 + i0$ with $\theta = 3.85$ and $\epsilon_0^2 = 1.3$. (a) shows the temporal
evolutions through the complex phase space, while (b) show how the coupled
field intensities vary over the same evolution.
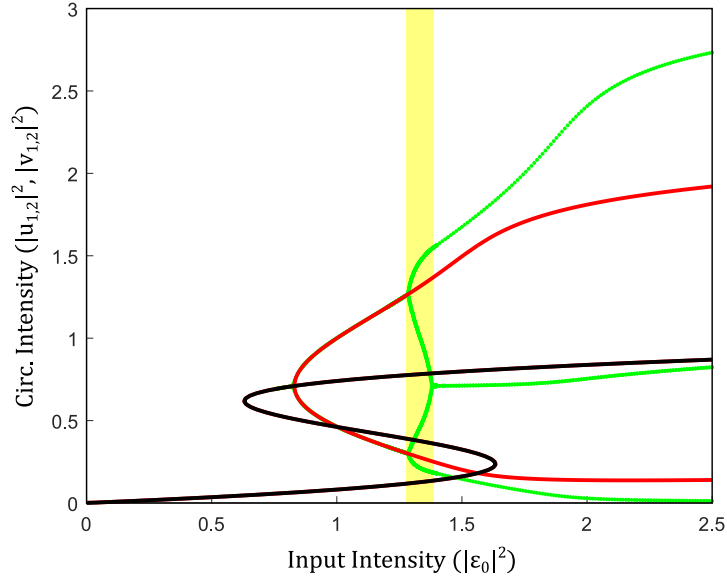
Figure 7.9: A high to low input intensity scan, shown in green, of the system
of equations (7.22)-(7.25) for $\theta = 3.85$. Overlaid are the purely symmetric
solution line (black), and the HSS of the degenerate system where there are
two asymmetric pairs of symmetric solutions (red). The highlighted region
shows where all four field intensities are asymmetric and stable.

Figure 7.9 shows a high to low input intensity scan of Eq. (7.22)-(7.25)
for the input conditions $\theta = 3.85$. One can see the well known solutions to
the degenerate case, where from the four studied fields there are two sets of
two symmetric fields, shown in red, and shown in black is the fully degen-
erate case where all four field intensities are symmetric (equal). The green
curve shows the 'new' solutions which are made possible by the four coupled
equations. Note that this green curve originates from the red curve with a
second symmetry breaking bifurcation which leads to a region, highlighted in
yellow, where all four studied fields are asymmetric to each other, which may
be described 'nested symmetry breaking'.

The potential for four symmetry broken fields implies that many of the
pre-reported behaviours in earlier chapters may be also expandable here, such
as four periodically interchanging fields. Further, if the system of Eq. (7.22)-
(7.25) is expanded to include slow-time considerations then the possibility for
four way symmetry broken temporal cavity solitons and breathers may also
be possible. Initial simulations imply that this region for four-way symmetry
breaking is widened for higher cavity detunings.

Turning attention to the higher input intensities of Fig. 7.9 one eventually
leaves the shaded region where all four field intensities are asymmetric and
arrives at an interesting behaviour where there is the partial restoration in
the system of symmetry. This partial symmetry restoration is very interesting
since it is very different to the symmetry restoration bifurcation described in
previous chapters. Firstly it is not a pitchfork bifurcation and secondly it only
restores the symmetry of two of the field intensities; it leads to the situation
of two stand alone asymmetric fields and a pair of two symmetric fields.

The prediction of four asymmetric solutions and this new semi-symmetry-
broken state of affairs could blow the range of observable dynamical behaviours
wide open and allow for many new, or extensions to pre-suggested, applica-
tions, such as components for use in all optical computing with higher degrees
of programmable freedom.

Routes for taking this work forward include a full bifurcation analysis of
both the nested symmetry breaking bifurcations and the partial symmetry
restoring bifurcations, and their conditions on forming. A linear stability anal-
ysis on the system would also be beneficial.

7.3 Chapter Summary

This chapter outlined the results of two small but relevant projects which
contain much scope for continued work.

In the first section we began by introducing an asymmetry to the system
of two homogeneous circulating fields in the form of different input pumps,
breaking the normally observable pitchfork bifurcation. We went on to show
that through introducing a second asymmetry to the system, this time from
imposing different cavity detunings, it is possible to restore two pitchfork-like
bifurcations.

Analysis of the restored bifurcation revealed that it was different in a couple
of ways to that seen in the system with symmetric inputs. Most obviously it
was no longer a symmetry breaking bifurcation due to the lack of inherent
symmetry in the system but more subtly the bifurcation itself was in fact a
perturbed version of the pitchfork.

Through discussions on the universal unfolding of the pitchfork bifurca-
tion, with a functional asymmetry present, $\tilde{a}(\chi, \delta\theta)$, which mathematically
transformed the system, it was shown that the connected perturbed pitchfork,
restored through our balancing of two asymmetries, was indeed in keeping
with the universal unfolding theory.

Finally we discussed the fact that even when the perturbed pitchfork is not
perfectly connected, the alternative path way be reached by the system but this
required some activation energy, supplied perhaps from adequate noise, to be
used. This path bias would be very important for the development of devices
hoping to replicate certain features of the spontaneous symmetry breaking
phenomenon with balanced asymmetric inputs, the system path choice being
favoured one way may hinder, or in fact be of benefit, to such applications.

In the second section of this chapter we derived a new model which predicts
the circulating intensities of counter-propagating fields while taking into ac-
count field polarisation effects. This system of four coupled equations predicts
nested symmetry breaking bifurcations, which lead to the new situations of
four symmetry broken fields, $u_1 = u_2 = v_1 = v_2$, and the strange case of two
asymmetric fields and a pair of symmetric fields, such as $u_1 = u_2 \neq v_1 \neq v_2$.
This system provides a very rich range of dynamics for further investigation
with more degrees of freedom for symmetry breaking, which may be very useful
for applications requiring more diversity than those based on the two equation
system.

*"The best laid schemes o' mice
an' men / Gang aft a-gley."*

– Robert Burns, To a Mouse

Chapter 8

Conclusions

During this thesis the theoretical models of various passive Kerr ring resonator setups were studied; primarily a system involving two counter circulating, linearly polarised, light fields and a system of two co-propagating light fields which are orthogonally polarised with respect to one another. Although not contained specifically within this thesis, many of the theoretical results which are contained were later experimentally verified by collaborators and details on these experiments can be found in the papers which complement many of these chapters. The main findings of this dissertation are summarised here.

It had been shown early on that a spontaneous symmetry breaking of the two systems, where two circulating fields go from having equal intensities to different intensities, with one field becoming dominant while the second is suppressed, can be described, in each case, by two coupled Lorentzian equations which model the intensities of the two circulating components. In Chapter 3 we showed that these equations can be manipulated to allow for the visualisation of this symmetry breaking in a multitude of ways with some providing mathematical or aesthetic advantages over others.

Following the restoration of a 'slow'-temporal derivative to these coupled equations, the system was subjected to a linear stability analysis which confirmed that the spontaneous emergence of asymmetric solutions was combined with a loss of stability of the symmetric solution, thus explaining experimental results showing asymmetry emerging naturally in favour of the symmetric possibility. This analysis, and the resulting eigenvalues, also showed that, for appropriate parameters, even the asymmetric solutions can become unstable,

leaving the system susceptible to oscillations.

The predicted local susceptibility of the system to oscillations prompted study into how these oscillations actually evolved on a macroscopic level. In Chapter 4, it was not only found that the predicted growing oscillations eventually cease their growth due to saturation, but also that the resulting oscillations were very diverse in their nature. It was shown that simple sinusoidal oscillations can undergo sequential period-doubling bifurcations, upon appropriate changes to input conditions, which had the potential to eventually lead to deterministic chaos, the collision of Feigenbaum cascades, and crises.

One of the more interesting results to emerge from this study into potential system oscillations came from the spontaneous emergence of order within chaos. This spontaneous order was found to be brought about by the merging of two attractors and physically leads to the periodic interchange between the dominant and suppressed roles which the two circulating fields take, implying a partial symmetry restoration in the system.

In Chapter 5 we then went on to generalise the analysis of the coupled equations describing the two ring resonator setups to include arbitrary self- and cross-phase modulation. This expanded the theoretical predictions to encapsulate ring resonators made from a multitude of different Kerr materials and states of matter, for example hollow fibers filled with a Kerr liquid or gas.

Variations in the self- and cross-phase modulation strengths were found to not only alter the required conditions on the laser input to observe symmetry breaking, but also to lead to other useful phenomenon such as a theoretically infinite symmetry broken region (where no symmetry restoring bifurcation occurred) and the ability to generate symmetry broken solutions below the threshold for symmetric optical bistability.

Generalisations to the linear stability analysis were also made in Chapter 5, and this revealed that the range of system susceptibility to oscillations increased with the cross-phase modulation and that higher values could also lead to broader regions where the periodic switching of the dominant and suppressed roles remained viable before reversion to chaotic oscillations.

Following the restoration of a second temporal derivative in Chapter 6, this time a second order fast-time derivative describing group velocity dispersion, the set of equations studied became a coupled set of Lugiato-Lefever equations.

This allowed for the study of temporal evolutions which took place on the time scale of one resonator round-trip. The validity of this model was however now limited to only the case of two co-propagating fields with orthogonal polarisations. It was solved using the split-step Fourier method.

In this chapter we showed that temporal cavity solitons form under certain circumstances in the coupled system and, through scanning values of the cavity detuning, were shown to not only also experience spontaneous symmetry breaking but for this breaking to actually occur at lower conditions than that required by the homogeneous solutions.

Analogous to the homogeneous field oscillations, the peaks of the TCS were also found to oscillate, or breathe, under certain circumstances. These breathing dynamics were found to have a similar diversity to those of the homogeneous solutions.

In the Chapter 7 two short projects were addressed to complement this thesis' analysis. The first part of this chapter concerned the balancing of asymmetric input conditions in an attempt at restoring a pitchfork-like bifurcation for the system. It was found that while a bifurcation is recovered through the proposed balancing procedure, this bifurcation was a perturbed variation of the standard symmetry breaking pitchfork bifurcation. The restored bifurcation was a variant from the universal unfolding of the pitchfork bifurcation and could be described as a connected perturbed pitchfork bifurcation. This restored the possibility for either field to take up the dominant or suppressed role within the system.

Away from the bifurcation restoring values of the balancing parameters, the bifurcation only allows for the system to follow one of the possible two stable branches of the unconnected perturbed pitchfork, that is unless some non-zero activation energy, perhaps supplied by small fluctuations, allows for the system to make the jump between paths.

The second part of Chapter 7 concerned itself with the derivation of a model which combined the two systems of primary interest; that is it modeled two counter-propagating fields while simultaneously allowing for field polarisation considerations.

The model derived could not be solved for homogeneous stationary states in the manner employed in previous chapters of this thesis due to the inclusion

119

of complex conjugate terms within the nonlinearity itself; it could however be evolved by using a four way coupled Runge-Kutta method.

Numerical integration of the four-equation system for a scan of the input intensity revealed that, atop the symmetric and asymmetric solutions typical of the degenerate two-equation system, there was the possibility for 'nested' symmetry breaking bifurcations. This led to the possible case of a fully asymmetric system, where all circulating field components were asymmetric to each other, and also to the interesting case of a partially symmetric system, where two of the fields pair up and become symmetric while the remaining two are left asymmetric both to the symmetric pair and to each other.

This combined model and its resulting solutions provides a potentially very fruitful area for additional research. For example a linear stability analysis of the system would be revealing in terms of the potential for highly complex oscillations and a study of the required input conditions for this nested symmetry breaking and partial symmetry restoration may be of great interest to experimentalists looking to use the phenomenon to create devices with higher degrees of freedom over the two equation system.

"Just go forward in all your beliefs
and prove to me that I am not mistaken in mine"

– The First Doctor, Dr Who

Appendix A

Numerical Methods

Recall the the system of coupled purely temporal LLEs:

$$\frac{\partial E_\pm}{\partial t} = E_{in} - E_\pm - i\theta E_\pm - i\eta \frac{\partial^2 E_\pm}{\partial \tau^2} + i\left(A|E_\pm|^2 + B|E_\mp|^2\right)E_\pm \qquad \text{(A.1)}$$

To solve this PDE system we employed a combination of two known numerical methods for integration, 2nd order Runge-Kutta and the split-step Fourier method. For those who may not be familiar with these methods we give here a brief introduction to these methods before explaining their combination and ultimately their application to our studied coupled systems.

A.1 An Introduction to 2nd Order Runge-Kutta Integration

The Runge-Kutta method of integration is very well known and follows a similar idea to that of Euler's method, it solves an initial value problem by propagating the solution by a sequence of small steps, but rather than evaluating the studied function only once at each step it evaluates it a number of times. For those interested in the history development and derivation of the Runge-Kutta method a nice paper on the subject is Ref. [184].

Most will be aware that there are higher order Runge-Kutta methods which boast better accuracy, however there is good reason for us only using 2nd order here which should hopefully become apparent later.

The 2nd order Runge-Kutta method with a step size of h can be used to solve problems of the form

$$\frac{dy}{dx} = f(x, y), \qquad y(x_0) = y_0 \tag{A.2}$$

by using the recurrence relation

$$y_{n+1} = y_n + k_2 + \mathcal{O}(h^3), \qquad n = 0, 1, 2, ... \tag{A.3}$$

with

$$
\begin{aligned}
k_1 &= hf(x_n, y_n) \\
k_2 &= hf(x_n + \frac{1}{2}h, y_n + \frac{1}{2}k_1)
\end{aligned}
\tag{A.4}
$$

Since the error per step (local error) is $\mathcal{O}(h^3)$, the total, or global, error in integrating $H = Nh$ over N steps is given by $N\mathcal{O}(h^3) = H\mathcal{O}(h^3)/h = H\mathcal{O}(h^2)$. The method's error is there for 2nd order with respect to the integration step size.

A.2 An Introduction to Split-step Fourier Integration

The slightly less well known Split-step Fourier method is commonly used to solve nonlinear PDEs. It treats the linear and nonlinear aspects of the PDE differently making use of Fourier space to simplify some of the operations required for solving each subsequent integration step. If more detail is required than is briefly described here, a useful introduction to the method, along with example applications, was found in Ref. [185].

One starts the method by splitting the PDE into the linear and nonlinear parts, such that the PDE may be expressed like so

$$\frac{\partial F}{\partial t} = [\hat{D} + \hat{N}]F + C \tag{A.5}$$

where $\hat{D}$ and $\hat{N}$ denote the operators which, when applied to F, restore the linear and nonlinear parts of the original PDE respectively and C denotes any constant terms.

The Baker-Hausdorff formula can show that the error involved in treating the two operators as if they commute is $\mathcal{O}(h^2)$ [186]. Making this treatment, the solution after a small integration step $h = dt$ can be found by first accounting for $\hat{D}$ and then $\hat{N}$ [185].

On a side note, due to the just established error order of the split-step Fourier method, it should now become apparent as to why we only later use this method in combination with the 2nd order Runge-Kutta method. If we utilised the 4th order Runge-Kutta method then the overall error of the combined integration would still be $\mathcal{O}(dt^2)$, due to the split-step's error, and computational time would be needlessly increased due to the added complexity of the 4th order Runge-Kutta method.

Returning to the split-step Fourier method itself, we focus initially on the linear part of the PDE, which has an analytical solution in the frequency domain.

$$F_{D,\,n} = e^{dt\hat{D}}F_n \tag{A.6}$$

To make use of this solution we must employ the Fourier Transform $\mathcal{F}$ defined by

$$\hat{F}(k) = \mathcal{F}(F) = \int_{-\infty}^{\infty} F(\tau)e^{-2\pi k\tau}d\tau \tag{A.7}$$

with the inverse defined as

$$F(\tau) = \mathcal{F}^{-1}(\hat{F}) = \int_{-\infty}^{\infty} \hat{F}(k)e^{2\pi k\tau}dk \tag{A.8}$$

where k is the associated wave number of the transformed variable.

A useful trick, which will later be employed in solving Eq. (A.1), when using the split-step Fourier method is that:

$$\mathcal{F}\left(\frac{dF}{d\tau}\right) = ik\hat{F}, \quad \mathcal{F}\left(\frac{d^2F}{d\tau^2}\right) = -k^2\hat{F} \tag{A.9}$$

Overall this method amounts to the integration, by a small step, of the linear part of the PDE being expressed in real space by

$$F_{D,\,n} = \mathcal{F}^{-1}\mathcal{F}(e^{dt\hat{D}}F_n) \tag{A.10}$$

Next, the nonlinear operator and constants must be taken into account which we do by using the 2nd order Runge-Kutta method described above. In this way one obtains the full integration method for a small step dt:

$$F_{n+1} = F_{D,\,n} + k_2 + \mathcal{O}(dt^2), \tag{A.11}$$

with

$$k_2 = dt \left(\hat{N} \left[F_{D,n} + \frac{k_1}{2} \right] + C \right),$$
$$k_1 = dt \left(\hat{N} \left[F_{D,n} \right] + C \right). \tag{A.12}$$

A.3 Integrating Coupled LLEs

In the case of coupled purely temporal LLEs eq. (A.1) we apply these methods by first splitting the two equations into linear, nonlinear and constant parts:

$$\hat{D} = -i\eta \frac{\partial^2}{\partial \tau^2}, \quad \hat{N} = -1 - i\theta + i \left(A|E_\pm|^2 + B|E_\mp|^2 \right), \quad C = E_{in}. \tag{A.13}$$

Note: although not strictly nonlinear, we may move $-1 - i\theta$ from $\hat{D}$ to $\hat{N}$ since it is the $\frac{\partial^2}{\partial^2 \tau}$ term that we wish to isolate.

Then, by employing Eq. (A.10), we begin the Split-step Fourier method:

$$\begin{aligned}
E_{\pm D}(\tau, t + dt) &= \mathcal{F}^{-1} \mathcal{F}(e^{dt\hat{D}} E_\pm) \\
&= \mathcal{F}^{-1} \mathcal{F} \left[e^{dt\left(-i\eta \frac{\partial^2}{\partial \tau^2}\right)} E_\pm \right] \\
&= \mathcal{F}^{-1} \left[e^{idt\eta k^2} \mathcal{F}(E_\pm) \right]
\end{aligned} \tag{A.14}$$

We proceed to utilise the Runge-Kutta method to obtain:

$$E_{\pm, n+1} = \mathcal{F}^{-1} \left[e^{idt\eta k^2} \mathcal{F}(E_{\pm, n}) \right] + k_{\pm 2} + \mathcal{O}(dt^2) \tag{A.15}$$

with

$$k_{\pm 2} = dt \left[\left(-1 - i\theta + iA \left| E_{\pm D, n} + \frac{k_{\pm 1}}{2} \right|^2 + iB \left| E_{\mp D, n} + \frac{k_{\mp 1}}{2} \right|^2 \right) \left(E_{\pm D, n} + \frac{k_{\pm 1}}{2} \right) + E_{in} \right]$$
$$k_{\pm 1} = dt \left[\left(-1 - i\theta + iA \left| E_{\pm D, n} \right|^2 + iB \left| E_{\mp D, n} \right|^2 \right) E_{\pm D, n} + E_{in} \right] \tag{A.16}$$

Equation (A.15) then forms the recurrence relationship used to simulate the evolution of Eq. (A.1) throughout this thesis. This may be augmented

with a random component to simulate noise within the system. Note that in early chapters, where $\frac{\partial^2 E_\pm}{\partial \tau^2} = 0$, only the Runge-Kutta method is required for integration, since there is no need to split into linear and nonlinear parts, with the recurrence relation given by:

$$E_{\pm,\,n+1} = E_{\pm n} + k_{\pm 2} + \mathcal{O}(dt^2) \tag{A.17}$$

with

$$k_{\pm 2} = dt \left[\left(-1 - i\theta + iA \left| E_{\pm n} + \frac{k_{\pm 1}}{2} \right|^2 + iB \left| E_{\mp n} + \frac{k_{\mp 1}}{2} \right|^2 \right) \left(E_{\pm n} + \frac{k_{\pm 1}}{2} \right) + E_{in} \right]$$

$$k_{\pm 1} = dt \left[\left(-1 - i\theta + iA \left| E_{\pm n} \right|^2 + iB \left| E_{\mp n} \right|^2 \right) E_{\pm n} + E_{in} \right]$$

$$\tag{A.18}$$

The combined model discussed in the final chapter of this thesis is also solved by the Runge-Kutta method where the recurrence relation now incorporates the four fields in a manner not too dissimilar to Eq. (A.17).
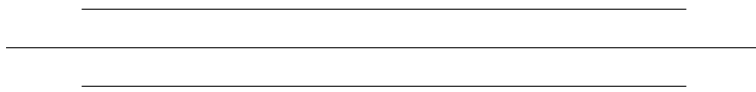
Bibliography

[1] R. W. Boyd, *Nonlinear optics, 3rd.* Academic press, 2008.

[2] G. N. Lewis, D. Lipkin, and T. T. Magel, "Reversible photochemical processes in rigid media. a study of the phosphorescent state," *Journal of the American Chemical Society*, vol. 63, no. 11, pp. 3005–3018, 1941.

[3] J. Kerr, "Xl. a new relation between electricity and light: Dielectrified media birefringent," *The London, Edinburgh, and Dublin Philosophical Magazine and Journal of Science*, vol. 50, no. 332, pp. 337–348, 1875.

[4] J. Kerr, "Liv. a new relation between electricity and light: Dielectrified media birefringent (second paper)," *The London, Edinburgh, and Dublin Philosophical Magazine and Journal of Science*, vol. 50, no. 333, pp. 446–458, 1875.

[5] P. Grelu, *Nonlinear optical cavity dynamics: from microresonators to fiber lasers.* John Wiley & Sons, 2015.

[6] A. Pasquazi, M. Peccianti, L. Razzari, D. J. Moss, S. Coen, M. Erkintalo, Y. K. Chembo, T. Hansson, S. Wabnitz, P. Del'Haye, *et al.*, "Microcombs: A novel generation of optical sources," *Physics Reports*, vol. 729, pp. 1–81, 2018.

[7] S. Spillane, T. Kippenberg, and K. Vahala, "Ultralow-threshold raman laser using a spherical dielectric microcavity," *Nature*, vol. 415, no. 6872, pp. 621–623, 2002.

[8] P. Del'Haye, A. Schliesser, O. Arcizet, T. Wilken, R. Holzwarth, and T. J. Kippenberg, "Optical frequency comb generation from a monolithic microresonator," *Nature*, vol. 450, no. 7173, pp. 1214–1217, 2007.

[9] P. Del'Haye, O. Arcizet, A. Schliesser, R. Holzwarth, and T. J. Kippenberg, "Full stabilization of a microresonator-based optical frequency comb," *Physical Review Letters*, vol. 101, no. 5, p. 053903, 2008.

[10] F. Ferdous, H. Miao, D. E. Leaird, K. Srinivasan, J. Wang, L. Chen, L. T. Varghese, and A. M. Weiner, "Spectral line-by-line pulse shaping of on-chip microresonator frequency combs," *Nature Photonics*, vol. 5, no. 12, pp. 770–776, 2011.

[11] J. S. Levy, A. Gondarenko, M. A. Foster, A. C. Turner-Foster, A. L. Gaeta, and M. Lipson, "Cmos-compatible multiple-wavelength oscillator for on-chip optical interconnects," *Nature photonics*, vol. 4, no. 1, pp. 37–40, 2010.

[12] L. Razzari, D. Duchesne, M. Ferrera, R. Morandotti, S. Chu, B. Little, and D. Moss, "Cmos-compatible integrated optical hyper-parametric oscillator," *Nature Photonics*, vol. 4, no. 1, p. 41, 2010.

[13] T. Herr, K. Hartinger, J. Riemensberger, C. Wang, E. Gavartin, R. Holzwarth, M. Gorodetsky, and T. Kippenberg, "Universal formation dynamics and noise of kerr-frequency combs in microresonators," *Nature photonics*, vol. 6, no. 7, pp. 480–487, 2012.

[14] A. Kaplan and P. Meystre, "Enhancement of the Sagnac effect due to nonlinearly induced nonreciprocity," *Optics letters*, vol. 6, no. 12, pp. 590–592, 1981.

[15] G. B. Malykin, "Sagnac effect in ring lasers and ring resonators. how does the refractive index of the optical medium influence the sensitivity to rotation?," *Physics-Uspekhi*, vol. 57, no. 7, p. 714, 2014.

[16] S. Sunada, "Large sagnac frequency splitting in a ring resonator operating at an exceptional point," *Physical Review A*, vol. 96, no. 3, p. 033842, 2017.

[17] Z. Feng, Y. He, W. Yan, F. Yang, W. Han, and Z. Li, "Progress of waveguide ring resonators used in micro-optical gyroscopes," in *Photonics*, vol. 7, p. 96, Multidisciplinary Digital Publishing Institute, 2020.

[18] H. Zhang, J. Chen, J. Jin, J. Lin, L. Zhao, Z. Bi, A. Huang, and Z. Xiao, "On-chip modulation for rotating sensing of gyroscope based on ring resonator coupled with mach-zehnder interferometer," *Scientific reports*, vol. 6, no. 1, pp. 1–9, 2016.

[19] S. Coen and M. Erkintalo, "Temporal cavity solitons in kerr media," *Nonlinear Optical Cavity Dynamics: From Microresonators to Fiber Lasers*, pp. 11–40, 2016.

[20] F. Leo, S. Coen, P. Kockaert, S.-P. Gorza, P. Emplit, and M. Haelterman, "Temporal cavity solitons in one-dimensional kerr media as bits in an all-optical buffer," *Nature Photonics*, vol. 4, no. 7, pp. 471–476, 2010.

[21] F. Leo, L. Gelens, P. Emplit, M. Haelterman, and S. Coen, "Dynamics of one-dimensional kerr cavity solitons," *Optics express*, vol. 21, no. 7, pp. 9180–9191, 2013.

[22] S. Coen, H. G. Randle, T. Sylvestre, and M. Erkintalo, "Modeling of octave-spanning kerr frequency combs using a generalized mean-field lugiato–lefever model," *Optics letters*, vol. 38, no. 1, pp. 37–39, 2013.

[23] L. Del Bino, J. M. Silver, M. T. Woodley, S. L. Stebbings, X. Zhao, and P. Del'Haye, "Microresonator isolators and circulators based on the intrinsic nonreciprocity of the kerr effect," *Optica*, vol. 5, no. 3, pp. 279–282, 2018.

[24] N. Moroney, L. Del Bino, M. T. Woodley, G. N. Ghalanos, J. M. Silver, A. Ø. Svela, S. Zhang, and P. Del'Haye, "Logic gates based on interaction of counterpropagating light in microresonators," *Journal of Lightwave Technology*, vol. 38, no. 6, pp. 1414–1419, 2020.

[25] J. Ma, X. Jiang, and M. Xiao, "Kerr frequency combs in large-size, ultra-high-q toroid microcavities with low repetition rates," *Photonics Research*, vol. 5, no. 6, pp. B54–B58, 2017.

[26] Y. Xuan, Y. Liu, L. T. Varghese, A. J. Metcalf, X. Xue, P.-H. Wang, K. Han, J. A. Jaramillo-Villegas, A. Al Noman, C. Wang, *et al.*, "High-q silicon nitride microresonators exhibiting low-power frequency comb initiation," *Optica*, vol. 3, no. 11, pp. 1171–1180, 2016.

[27] X. Liu, C. Sun, B. Xiong, L. Wang, J. Wang, Y. Han, Z. Hao, H. Li, Y. Luo, J. Yan, *et al.*, "Integrated high-q crystalline aln microresonators for broadband kerr and raman frequency combs," *ACS Photonics*, vol. 5, no. 5, pp. 1943–1950, 2018.

[28] Z. Ye, K. Twayana, P. A. Andrekson, *et al.*, "High-q si 3 n 4 microresonators based on a subtractive processing for kerr nonlinear optics," *Optics express*, vol. 27, no. 24, pp. 35719–35727, 2019.

[29] A. Kordts, M. H. Pfeiffer, H. Guo, V. Brasch, and T. J. Kippenberg, "Higher order mode suppression in high-q anomalous dispersion sin microresonators for temporal dissipative kerr soliton formation," *Optics letters*, vol. 41, no. 3, pp. 452–455, 2016.

[30] H. Gibbs, *Optical bistability: controlling light with light.* Elsevier, 2012.

[31] L. Lugiato and R. Lefever, "Spatial Dissipative Structures in Passive Optical Systems," *Physical Review Letters*, vol. 58, no. 21, pp. 2209–2211, 1987.

[32] A. Kaplan and P. Meystre, "Directionally asymmetrical bistability in a symmetrically pumped nonlinear ring interferometer," *Optics Communications*, vol. 40, no. 3, pp. 229–232, 1982.

[33] J. Geddes, J. V. Moloney, E. M. Wright, and W. Firth, "Polarisation patterns in a nonlinear cavity," *Optics communications*, vol. 111, no. 5-6, pp. 623–631, 1994.

[34] A. Gasch and D. Jäger, "Nonlinear nonreciprocity and directional bistability in a ring resonator with a quadratic nonlinear medium," *Physical review letters*, vol. 59, no. 19, p. 2145, 1987.

[35] L. Del Bino, J. M. Silver, S. L. Stebbings, and P. Del'Haye, "Symmetry breaking of counter-propagating light in a nonlinear resonator," *Scientific Reports*, vol. 7, p. 43142, 2017.

[36] S. Zhang. Private communication, 16/12/2020.

[37] B. Garbin, J. Fatome, G.-L. Oppo, M. Erkintalo, S. G. Murdoch, and S. Coen, "Asymmetric balance in symmetry breaking," *Physical Review Research*, vol. 2, no. 2, p. 023244, 2020.

[38] W. Bogaerts, P. De Heyn, T. Van Vaerenbergh, K. De Vos, S. Kumar Selvaraja, T. Claes, P. Dumon, P. Bienstman, D. Van Thourhout, and R. Baets, "Silicon microring resonators," *Laser & Photonics Reviews*, vol. 6, no. 1, pp. 47–73, 2012.

[39] L. Mercadé, L. L. Martín, A. Griol, D. Navarro-Urrios, and A. Martínez, "Microwave oscillator and frequency comb in a silicon optomechanical cavity with a full phononic bandgap," *Nanophotonics*, vol. 1, no. ahead-of-print, 2020.

[40] B. Nikolaus and D. Grischkowsky, "12× pulse compression using optical fibers," *Applied Physics Letters*, vol. 42, no. 1, pp. 1–2, 1983.

[41] D. Strickland and G. Mourou, "Compression of amplified chirped optical pulses," *Optics communications*, vol. 56, no. 3, pp. 219–221, 1985.

[42] L. Lugiato, F. Prati, and M. Brambilla, *Nonlinear Optical Systems*. Cambridge University Press, 2015.

[43] A. Husakou, V. Kalosha, and J. Herrmann, "Nonlinear phenomena with ultra-broadband optical radiation in photonic crystal fibers and hollow waveguides," in *Optical Solitons*, pp. 299–325, Springer, 2002.

[44] M. Haelterman, S. Trillo, and S. Wabnitz, "Dissipative modulation instability in a nonlinear dispersive ring cavity," *Optics communications*, vol. 91, no. 5-6, pp. 401–407, 1992.

[45] G. P. Agrawal, *Applications of nonlinear fiber optics*. Academic press, 2020.

[46] K. Blow and N. Doran, "Global and local chaos in the pumped nonlinear schrödinger equation," *Physical review letters*, vol. 52, no. 7, p. 526, 1984.

[47] L. A. Lugiato, "Ii theory of optical bistability," *Progress in optics*, vol. 21, pp. 69–216, 1984.

[48] F. Bassani, *Encyclopedia of condensed matter physics*. Elsevier acad. press, 2005.

[49] M. Haelterman, S. Trillo, and S. Wabnitz, "Additive-modulation-instability ring laser in the normal dispersion regime of a fiber," *Optics letters*, vol. 17, no. 10, pp. 745–747, 1992.

[50] V. E. Zakharov and L. A. Ostrovsky, "Modulation instability: the beginning," *Physica D: Nonlinear Phenomena*, vol. 238, no. 5, pp. 540–548, 2009.

[51] J. M. Dudley, F. Dias, M. Erkintalo, and G. Genty, "Instabilities, breathers and rogue waves in optics," *Nature Photonics*, vol. 8, no. 10, pp. 755–764, 2014.

[52] G. Baskaran and P. W. Anderson, "Gauge theory of high-temperature superconductors and strongly correlated fermi systems," *Physical Review B*, vol. 37, no. 1, p. 580, 1988.

[53] J. Bernstein, "Spontaneous symmetry breaking, gauge theories, the higgs mechanism and all that," *Reviews of modern physics*, vol. 46, no. 1, p. 7, 1974.

[54] J. Rossi, R. Carretero-González, P. Kevrekidis, and M. Haragus, "On the spontaneous time-reversal symmetry breaking in synchronously-pumped passive kerr resonators," *Journal of Physics A: Mathematical and Theoretical*, vol. 49, no. 45, p. 455201, 2016.

[55] Y. Xu and S. Coen, "Experimental observation of the spontaneous breaking of the time-reversal symmetry in a synchronously pumped passive kerr resonator," *Optics letters*, vol. 39, no. 12, pp. 3492–3495, 2014.

[56] B. Peng, Ş. K. Özdemir, F. Lei, F. Monifi, M. Gianfreda, G. L. Long, S. Fan, F. Nori, C. M. Bender, and L. Yang, "Parity–time-symmetric whispering-gallery microcavities," *Nature Physics*, vol. 10, no. 5, p. 394, 2014.

[57] F. Copie, M. T. Woodley, L. Del Bino, J. M. Silver, S. Zhang, and P. Del'Haye, "Interplay of polarization and time-reversal symmetry breaking in synchronously pumped ring resonators," *Physical review letters*, vol. 122, no. 1, p. 013905, 2019.

[58] P. Kevrekidis, Z. Chen, B. Malomed, D. Frantzeskakis, and M. Weinstein, "Spontaneous symmetry breaking in photonic lattices: Theory and experiment," *Physics Letters A*, vol. 340, no. 1-4, pp. 275–280, 2005.

[59] V. Savona, "Spontaneous symmetry breaking in a quadratically driven nonlinear photonic lattice," *Physical Review A*, vol. 96, no. 3, p. 033826, 2017.

[60] O. Bahat-Treidel, O. Peleg, and M. Segev, "Symmetry breaking in honeycomb photonic lattices," *Optics letters*, vol. 33, no. 19, pp. 2251–2253, 2008.

[61] F. Zhang, M. Pu, J. Luo, H. Yu, and X. Luo, "Symmetry breaking of photonic spin-orbit interactions in metasurfaces," *Opto-Electronic Engineering*, vol. 44, no. 03, pp. 319–325, 2017.

[62] S. Weinberg, "Nonlinear realizations of chiral symmetry," *Physical Review*, vol. 166, no. 5, p. 1568, 1968.

[63] M. Liu, D. A. Powell, I. V. Shadrivov, M. Lapine, and Y. S. Kivshar, "Spontaneous chiral symmetry breaking in metamaterials," *Nature communications*, vol. 5, no. 1, pp. 1–9, 2014.

[64] C. Viedma, "Chiral symmetry breaking during crystallization: complete chiral purity induced by nonlinear autocatalysis and recycling," *Physical review letters*, vol. 94, no. 6, p. 065504, 2005.

[65] Q.-T. Cao, H. Wang, C.-H. Dong, H. Jing, R.-S. Liu, X. Chen, L. Ge, Q. Gong, and Y.-F. Xiao, "Experimental demonstration of spontaneous chirality in a nonlinear microresonator," *Physical review letters*, vol. 118, no. 3, p. 033901, 2017.

[66] P. Hamel, S. Haddadi, F. Raineri, P. Monnier, G. Beaudoin, I. Sagnes, A. Levenson, and A. M. Yacomotti, "Spontaneous mirror-symmetry breaking in coupled photonic-crystal nanolasers," *Nature Photonics*, vol. 9, no. 5, pp. 311–315, 2015.

[67] Y. Liu, X. Ling, X. Yi, X. Zhou, S. Chen, Y. Ke, H. Luo, and S. Wen, "Photonic spin hall effect in dielectric metasurfaces with rotational symmetry breaking," *Optics letters*, vol. 40, no. 5, pp. 756–759, 2015.

[68] M. Rahmani, A. S. Shorokhov, B. Hopkins, A. E. Miroshnichenko, M. R. Shcherbakov, R. Camacho-Morales, A. A. Fedyanin, D. N. Neshev, and Y. S. Kivshar, "Nonlinear symmetry breaking in symmetric oligomers," *ACS Photonics*, vol. 4, no. 3, pp. 454–461, 2017.

[69] G. Gligorić, P. P. Beličev, D. Leykam, and A. Maluckov, "Nonlinear symmetry breaking of aharonov-bohm cages," *Physical Review A*, vol. 99, no. 1, p. 013826, 2019.

[70] T. Mayteevarunyoo, B. A. Malomed, and G. Dong, "Spontaneous symmetry breaking in a nonlinear double-well structure," *Physical Review A*, vol. 78, no. 5, p. 053601, 2008.

[71] M. A. Gorlach, D. A. Dobrykh, A. P. Slobozhanyuk, P. A. Belov, and M. Lapine, "Nonlinear symmetry breaking in photometamaterials," *Physical Review B*, vol. 97, no. 11, p. 115119, 2018.

[72] E. M. Wright, P. Meystre, W. Firth, and A. Kaplan, "Theory of the nonlinear sagnac effect in a fiber-optic gyroscope," *Physical Review A*, vol. 32, no. 5, p. 2857, 1985.

[73] M. T. Woodley, J. M. Silver, L. Hill, F. Copie, L. Del Bino, S. Zhang, G.-L. Oppo, and P. Del'Haye, "Universal symmetry-breaking dynamics for the kerr interaction of counterpropagating light in dielectric ring resonators," *Physical Review A*, vol. 98, no. 5, p. 053863, 2018.

[74] R. M. May, "Simple mathematical models with very complicated dynamics," *Nature*, vol. 261, no. 5560, pp. 459–467, 1976.

[75] J. Pierce, "Logistic bifurcation map," *Wikimedia Commons*, (accessed: 28.08.2020).

[76] B. Maes, M. Fiers, and P. Bienstman, "Self-pulsing and chaos in short chains of coupled nonlinear microcavities," *Physical Review A*, vol. 80, no. 3, p. 033805, 2009.

[77] S. Abdollahi and V. Van, "Analysis of optical instability in coupled microring resonators," *JOSA B*, vol. 31, no. 12, pp. 3081–3087, 2014.

[78] Y. Dumeige and P. Féron, "Coupled optical microresonators for microwave all-optical generation and processing," *Optics letters*, vol. 40, no. 14, pp. 3237–3240, 2015.

[79] Y. Dumeige and P. Féron, "Stability and time-domain analysis of the dispersive tristability in microresonators under modal coupling," *Physical Review A*, vol. 84, no. 4, p. 043847, 2011.

[80] A. E. Fomin, M. L. Gorodetsky, I. S. Grudinin, and V. S. Ilchenko, "Nonstationary nonlinear effects in optical microspheres," *JOSA B*, vol. 22, no. 2, pp. 459–465, 2005.

[81] C. Bao, B. Shen, M.-G. Suh, H. Wang, K. Şafak, A. Dai, A. B. Matsko, F. X. Kärtner, and K. Vahala, "Oscillatory motion of a counterpropagating kerr soliton dimer," *Physical Review A*, vol. 103, no. 1, p. L011501, 2021.

[82] L. Gelens, S. Beri, G. Van der Sande, G. Mezosi, M. Sorel, J. Danckaert, and G. Verschaffelt, "Exploring multistability in semiconductor ring lasers: Theory and experiment," *Physical review letters*, vol. 102, no. 19, p. 193904, 2009.

[83] A. Trita, G. Mezosi, M. J. Latorre-Vidal, M. Zanola, M. J. Strain, F. Bragheri, M. Sorel, and G. Giuliani, "All-optical directional switching in bistable semiconductor-ring lasers," *IEEE Journal of Quantum Electronics*, vol. 49, no. 10, pp. 877–885, 2013.

[84] T. J. Kippenberg, A. L. Gaeta, M. Lipson, and M. L. Gorodetsky, "Dissipative kerr solitons in optical microresonators," *Science*, vol. 361, no. 6402, 2018.

[85] H. Bao, A. Cooper, M. Rowley, L. Di Lauro, J. S. T. Gongora, S. T. Chu, B. E. Little, G.-L. Oppo, R. Morandotti, D. J. Moss, *et al.*, "Laser cavity-soliton microcombs," *Nature Photonics*, vol. 13, no. 6, pp. 384–389, 2019.

[86] H. Guo, M. Karpov, E. Lucas, A. Kordts, M. H. Pfeiffer, V. Brasch, G. Lihachev, V. E. Lobanov, M. L. Gorodetsky, and T. J. Kippenberg, "Universal dynamics and deterministic switching of dissipative kerr solitons in optical microresonators," *Nature Physics*, vol. 13, no. 1, pp. 94–102, 2017.

[87] J. K. Jang, A. Klenner, X. Ji, Y. Okawachi, M. Lipson, and A. L. Gaeta, "Synchronization of coupled optical microresonators," *Nature Photonics*, vol. 12, no. 11, pp. 688–693, 2018.

[88] G. Xu, A. Nielsen, B. Garbin, L. Hill, G.-L. Oppo, J. Fatome, S. G. Murdoch, S. Coen, and M. Erkintalo, "Spontaneous symmetry breaking of dissipative optical solitons in a two-component kerr resonator," *arXiv preprint arXiv:2008.13776*, 2020.

[89] Q.-F. Yang, X. Yi, K. Y. Yang, and K. Vahala, "Counter-propagating solitons in microresonators," *Nature Photonics*, vol. 11, no. 9, p. 560, 2017.

[90] J. Amigo, L. Kocarev, and J. Szczepanski, "Theory and practice of chaotic cryptography," *Physics Letters A*, vol. 366, no. 3, pp. 211–216, 2007.

[91] F. Monifi, J. Zhang, Ş. K. Özdemir, B. Peng, Y.-x. Liu, F. Bo, F. Nori, and L. Yang, "Optomechanically induced stochastic resonance and chaos transfer between optical fields," *Nature Photonics*, vol. 10, no. 6, pp. 399–405, 2016.

[92] G. Giacomelli, F. Marin, and I. Rabbiosi, "Stochastic and bona fide resonance: An experimental investigation," *Physical Review Letters*, vol. 82, no. 4, p. 675, 1999.

[93] M. Virte, K. Panajotov, H. Thienpont, and M. Sciamanna, "Deterministic polarization chaos from a laser diode," *Nature Photonics*, vol. 7, no. 1, p. 60, 2013.

[94] J. Hillbrand, D. Auth, M. Piccardo, N. Opačak, E. Gornik, G. Strasser, F. Capasso, S. Breuer, and B. Schwarz, "In-phase and anti-phase synchronization in a laser frequency comb," *Physical review letters*, vol. 124, no. 2, p. 023901, 2020.

[95] A. Giraldo, B. Krauskopf, N. G. Broderick, J. A. Levenson, and A. M. Yacomotti, "The driven-dissipative bose–hubbard dimer: phase diagram and chaos," *New Journal of Physics*, vol. 22, no. 4, p. 043009, 2020.

[96] L. Lamport, "Buridan's principle," *Foundations of Physics*, vol. 42, no. 8, pp. 1056–1066, 2012.

[97] C. Chow, B. Gutkin, D. Hansel, C. Meunier, and J. Dalibard, *Methods and Models in Neurophysics: Lecture Notes of the Les Houches Summer School 2003*, ch. 6.4.3.2 Hopf Bifurcation of the Rotor System. Elsevier, 2004.

[98] G. Chen and X. Liu, *Friction dynamics*, ch. 2.7. Global bifurcations. Elsevier, 2016.

[99] E. Knobloch and M. Proctor, "The double hopf bifurcation with 2:1 resonance," *Proceedings of the Royal Society of London. A. Mathematical and Physical Sciences*, vol. 415, no. 1848, pp. 61–90, 1988.

[100] G. Oppo and A. Politi, "Collision of feigenbaum cascades," *Physical Review A*, vol. 30, no. 1, p. 435, 1984.

[101] A. Ben-Tal, "Symmetry restoration in a class of forced oscillators," *Physica D: Nonlinear Phenomena*, vol. 171, no. 4, pp. 236–248, 2002.

[102] M. Woodley, L. Hill, L. Del Bino, G.-L. Oppo, and P. Del'Haye, "Self-switching kerr oscillations of counter-propagating light in microresonators," *arXiv preprint arXiv:2005.01411*, 2020.

[103] T. Schneider, "Self-and cross-phase modulation," in *Nonlinear Optics in Telecommunications*, pp. 143–165, Springer, 2004.

[104] F. Shimizu, "Frequency broadening in liquids by a short light pulse," *Physical Review Letters*, vol. 19, no. 19, p. 1097, 1967.

[105] R. Stolen and C. Lin, "Self-phase-modulation in silica optical fibers," *Physical Review A*, vol. 17, no. 4, p. 1448, 1978.

[106] M. N. Islam, L. F. Mollenauer, R. H. Stolen, J. R. Simpson, and H.-T. Shang, "Cross-phase modulation in optical fibers," *Optics letters*, vol. 12, no. 8, pp. 625–627, 1987.

[107] W. Firth, I. Galbraith, and E. Wright, "Diffusion and diffraction in dispersive optical bistability," *JOSA B*, vol. 2, no. 6, pp. 1005–1009, 1985.

[108] W. Firth and C. Paré, "Transverse modulational instabilities for counterpropagating beams in Kerr media," *Optics letters*, vol. 13, no. 12, pp. 1096–1098, 1988.

[109] W. Firth, A. Fitzgerald, and C. Paré, "Transverse instabilities due to counterpropagation in Kerr media," *JOSA B*, vol. 7, no. 6, pp. 1087–1097, 1990.

[110] C. Penman, W. Firth, and C. Paré, "Transverse polarisation instabilities in a kerr medium," *Optics communications*, vol. 96, no. 1-3, pp. 174–184, 1993.

[111] M. Schmidberger, D. Novoa, F. Biancalana, P. S. J. Russell, and N. Joly, "Multistability and spontaneous breaking in pulse-shape symmetry in fiber ring cavities," *Optics express*, vol. 22, no. 3, pp. 3045–3053, 2014.

[112] J. B. Geddes, *Patterns, fishing and nonlinear optics*. The University of Arizona., 1994.

[113] J. Burgin, C. Guillon, and P. Langot, "Femtosecond investigation of the non-instantaneous third-order nonlinear suceptibility in liquids and glasses," *Applied Physics Letters*, vol. 87, no. 21, p. 211916, 2005.

[114] S. Das, S. Mukhopadhyay, N. Sinha, A. Saha, P. Datta, and S. Saltiel, "Modulation of effective nonlinearity ($\chi (3)$) due to cascaded processes in ppln for direct third harmonic generation," in *2006 Conference on Lasers and Electro-Optics and 2006 Quantum Electronics and Laser Science Conference*, pp. 1–2, IEEE, 2006.

[115] O. Balachninaite, R. Grigonis, A. Piskarskas, V. Sirutkaitis, and R. Eckardt, "Self-and cross-phase modulation in a ppln opo," in *Conference on Lasers and Electro-Optics*, p. CThC7, Optical Society of America, 2000.

[116] K. Miyata, N. Umemura, and K. Kato, "Phase-matched pure χ (3) third-harmonic generation in noncentrosymmetric bib 3 o 6," *Optics letters*, vol. 34, no. 4, pp. 500–502, 2009.

[117] A. S. Mayer, C. R. Phillips, and U. Keller, "Watt-level 10-gigahertz solid-state laser enabled by self-defocusing nonlinearities in an aperiodically poled crystal," *Nature communications*, vol. 8, no. 1, pp. 1–8, 2017.

[118] C.-W. Chen, J.-L. Tang, K.-H. Chung, T.-H. Wei, and T.-H. Huang, "Negative nonlinear refraction obtained with ultrashort laser pulses," *Optics express*, vol. 15, no. 11, pp. 7006–7018, 2007.

[119] F. Saltarelli, A. Diebold, I. Graumann, C. R. Phillips, and U. Keller, "Self-phase modulation cancellation in a high-power ultrafast thin-disk laser oscillator," *Optica*, vol. 5, no. 12, pp. 1603–1606, 2018.

[120] L. Hill, G.-L. Oppo, M. T. Woodley, and P. Del'Haye, "Effects of self- and cross-phase modulation on the spontaneous symmetry breaking of light in ring resonators," *Physical Review A*, vol. 101, no. 1, p. 013823, 2020.

[121] Y. Li, Z. Luo, Y. Liu, Z. Chen, C. Huang, S. Fu, H. Tan, and B. A. Malomed, "Two-dimensional solitons and quantum droplets supported by competing self-and cross-interactions in spin-orbit-coupled condensates," *New Journal of Physics*, vol. 19, no. 11, p. 113043, 2017.

[122] J. Allen, "The early history of solitons (solitary waves)," *Physica Scripta*, vol. 57, no. 3, p. 436, 1998.

[123] L. Debnath, "A brief historical introduction to solitons and the inverse scattering transform–a vision of scott russell," *International Journal of Mathematical Education in Science and Technology*, vol. 38, no. 8, pp. 1003–1028, 2007.

[124] A. J. S. Russell, "Report on waves, report of the 14th meeting of the british association for the advancement of science, 311-390," 1844.

[125] D. J. Korteweg and G. De Vries, "Xli. on the change of form of long waves advancing in a rectangular canal, and on a new type of long stationary waves," *The London, Edinburgh, and Dublin Philosophical Magazine and Journal of Science*, vol. 39, no. 240, pp. 422–443, 1895.

[126] L. Rayleigh, "On waves," *Phil. Mag.*, vol. 1, pp. 257–259, 1876.

[127] J. Boussinesq, "Théorie de l'intumescence liquide appelée onde solitaire ou de translation se propageant dans un canal rectangulaire," *CR Acad. Sci. Paris*, vol. 72, no. 755-759, p. 1871, 1871.

[128] J. Boussinesq, *Essai sur la théorie des eaux courantes*. Impr. nationale, 1877.

[129] D. Kordeweg and G. de Vries, "On the change of form of long waves advancing in a rectangular channel, and a new type of long stationary wave," *Phil. Mag*, vol. 39, pp. 422–443, 1895.

[130] W. Firth and A. Scroggie, "Optical bullet holes: robust controllable localized states of a nonlinear cavity," *Physical review letters*, vol. 76, no. 10, p. 1623, 1996.

[131] A. Scroggie, J. Jeffers, G. McCartney, and G.-L. Oppo, "Reversible soliton motion," *Physical Review E*, vol. 71, no. 4, p. 046602, 2005.

[132] N. Akhmediev and A. Ankiewicz, *Dissipative solitons: from optics to biology and medicine*, vol. 751. Springer Science & Business Media, 2008.

[133] T. Ackemann, W. Firth, and G.-L. Oppo, "Fundamentals and applications of spatial dissipative solitons in photonic devices," *Advances in atomic, molecular, and optical physics*, vol. 57, pp. 323–421, 2009.

[134] P. Grelu and N. Akhmediev, "Dissipative solitons for mode-locked lasers," *Nature photonics*, vol. 6, no. 2, pp. 84–92, 2012.

[135] S. Wabnitz, "Suppression of interactions in a phase-locked soliton optical memory," *Optics letters*, vol. 18, no. 8, pp. 601–603, 1993.

[136] M. Anderson, F. Leo, S. Coen, M. Erkintalo, and S. G. Murdoch, "Observations of spatiotemporal instabilities of temporal cavity solitons," *Optica*, vol. 3, no. 10, pp. 1071–1074, 2016.

[137] M. Anderson, Y. Wang, F. Leo, S. Coen, M. Erkintalo, and S. G. Murdoch, "Coexistence of multiple nonlinear states in a tristable passive kerr resonator," *Physical Review X*, vol. 7, no. 3, p. 031031, 2017.

[138] E. Lucas, M. Karpov, H. Guo, M. Gorodetsky, and T. J. Kippenberg, "Breathing dissipative solitons in optical microresonators," *Nature communications*, vol. 8, no. 1, pp. 1–11, 2017.

[139] X. Yi, Q.-F. Yang, K. Y. Yang, and K. Vahala, "Imaging soliton dynamics in optical microcavities," *Nature communications*, vol. 9, no. 1, pp. 1–8, 2018.

[140] A. L. Gaeta, M. Lipson, and T. J. Kippenberg, "Photonic-chip-based frequency combs," *Nature Photonics*, vol. 13, no. 3, pp. 158–169, 2019.

[141] J. K. Jang, M. Erkintalo, S. Coen, and S. G. Murdoch, "Temporal tweezing of light through the trapping and manipulation of temporal cavity solitons," *Nature communications*, vol. 6, no. 1, pp. 1–7, 2015.

[142] J. K. Jang, M. Erkintalo, J. Schröder, B. J. Eggleton, S. G. Murdoch, and S. Coen, "All-optical buffer based on temporal cavity solitons operating at 10 gb/s," *Optics letters*, vol. 41, no. 19, pp. 4526–4529, 2016.

[143] P. Marin-Palomo, J. N. Kemal, M. Karpov, A. Kordts, J. Pfeifle, M. H. Pfeiffer, P. Trocha, S. Wolf, V. Brasch, M. H. Anderson, *et al.*, "Microresonator-based solitons for massively parallel coherent optical communications," *Nature*, vol. 546, no. 7657, pp. 274–279, 2017.

[144] A. Fülöp, M. Mazur, A. Lorences-Riesgo, Ó. B. Helgason, P.-H. Wang, Y. Xuan, D. E. Leaird, M. Qi, P. A. Andrekson, A. M. Weiner, *et al.*, "High-order coherent communications using mode-locked dark-pulse kerr combs from microresonators," *Nature communications*, vol. 9, no. 1, pp. 1–8, 2018.

[145] D. T. Spencer, T. Drake, T. C. Briles, J. Stone, L. C. Sinclair, C. Fredrick, Q. Li, D. Westly, B. R. Ilic, A. Bluestone, *et al.*, "An optical-frequency synthesizer using integrated photonics," *Nature*, vol. 557, no. 7703, pp. 81–85, 2018.

[146] M.-G. Suh, X. Yi, Y.-H. Lai, S. Leifer, I. S. Grudinin, G. Vasisht, E. C. Martin, M. P. Fitzgerald, G. Doppmann, J. Wang, *et al.*, "Searching for exoplanets using a microresonator astrocomb," *Nature photonics*, vol. 13, no. 1, pp. 25–30, 2019.

[147] E. Obrzud, M. Rainer, A. Harutyunyan, M. H. Anderson, J. Liu, M. Geiselmann, B. Chazelas, S. Kundermann, S. Lecomte, M. Cecconi, *et al.*, "A microphotonic astrocomb," *Nature Photonics*, vol. 13, no. 1, pp. 31–35, 2019.

[148] M.-G. Suh, Q.-F. Yang, K. Y. Yang, X. Yi, and K. J. Vahala, "Microresonator soliton dual-comb spectroscopy," *Science*, vol. 354, no. 6312, pp. 600–603, 2016.

[149] A. Dutt, C. Joshi, X. Ji, J. Cardenas, Y. Okawachi, K. Luke, A. L. Gaeta, and M. Lipson, "On-chip dual-comb source for spectroscopy," *Science advances*, vol. 4, no. 3, p. e1701858, 2018.

[150] M.-G. Suh and K. J. Vahala, "Soliton microcomb range measurement," *Science*, vol. 359, no. 6378, pp. 884–887, 2018.

[151] P. Trocha, M. Karpov, D. Ganin, M. H. Pfeiffer, A. Kordts, S. Wolf, J. Krockenberger, P. Marin-Palomo, C. Weimann, S. Randel, *et al.*, "Ultrafast optical ranging using microresonator soliton frequency combs," *Science*, vol. 359, no. 6378, pp. 887–891, 2018.

[152] J. Riemensberger, A. Lukashchuk, M. Karpov, W. Weng, E. Lucas, J. Liu, and T. J. Kippenberg, "Massively parallel coherent laser ranging using a soliton microcomb," *Nature*, vol. 581, no. 7807, pp. 164–170, 2020.

[153] E. Averlant, M. Tlidi, K. Panajotov, and L. Weicker, "Coexistence of cavity solitons with different polarization states and different power peaks in all-fiber resonators," *Optics letters*, vol. 42, no. 14, pp. 2750–2753, 2017.

[154] E. Lucas, G. Lihachev, R. Bouchand, N. G. Pavlov, A. S. Raja, M. Karpov, M. L. Gorodetsky, and T. J. Kippenberg, "Spatial multiplexing of soliton microcombs," *Nature Photonics*, vol. 12, no. 11, pp. 699–705, 2018.

[155] C. Bao, P. Liao, A. Kordts, L. Zhang, A. Matsko, M. Karpov, M. H. Pfeiffer, G. Xie, Y. Cao, A. Almaiman, *et al.*, "Orthogonally polarized frequency comb generation from a kerr comb via cross-phase modulation," *Optics letters*, vol. 44, no. 6, pp. 1472–1475, 2019.

[156] A. U. Nielsen, B. Garbin, S. Coen, S. G. Murdoch, and M. Erkintalo, "Coexistence and interactions between nonlinear states with different polarizations in a monochromatically driven passive kerr resonator," *Physical review letters*, vol. 123, no. 1, p. 013902, 2019.

[157] M. Saha, S. Roy, and S. K. Varshney, "Polarization dynamics of a vector cavity soliton in a birefringent fiber resonator," *Physical Review A*, vol. 101, no. 3, p. 033826, 2020.

[158] D. N. Christodoulides and R. Joseph, "Vector solitons in birefringent nonlinear dispersive media," *Optics letters*, vol. 13, no. 1, pp. 53–55, 1988.

[159] M. Haelterman, A. Sheppard, and A. Snyder, "Bound-vector solitary waves in isotropic nonlinear dispersive media," *Optics letters*, vol. 18, no. 17, pp. 1406–1408, 1993.

[160] P. Balla and G. P. Agrawal, "Vector solitons and dispersive waves in birefringent optical fibers," *JOSA B*, vol. 35, no. 9, pp. 2302–2310, 2018.

[161] J. Haus, G. Shaulov, E. Kuzin, and J. Sanchez-Mondragon, "Vector soliton fiber lasers," *Optics letters*, vol. 24, no. 6, pp. 376–378, 1999.

[162] B. C. Collings, S. T. Cundiff, N. Akhmediev, J. M. Soto-Crespo, K. Bergman, and W. Knox, "Polarization-locked temporal vector solitons in a fiber laser: experiment," *JOSA B*, vol. 17, no. 3, pp. 354–365, 2000.

[163] V. Tsatourian, S. V. Sergeyev, C. Mou, A. Rozhin, V. Mikhailov, B. Rabin, P. S. Westbrook, and S. K. Turitsyn, "Polarisation dynamics of vector soliton molecules in mode locked fibre laser," *Scientific reports*, vol. 3, no. 1, pp. 1–8, 2013.

[164] P. Kockaert and M. Haelterman, "Stability and symmetry breaking of soliton bound states," *JOSA B*, vol. 16, no. 5, pp. 732–740, 1999.

[165] C. Cambournac, T. Sylvestre, H. Maillotte, B. Vanderlinden, P. Kockaert, P. Emplit, and M. Haelterman, "Symmetry-breaking instability of multimode vector solitons," *Physical review letters*, vol. 89, no. 8, p. 083901, 2002.

[166] A. Sigler and B. A. Malomed, "Solitary pulses in linearly coupled cubic–quintic ginzburg–landau equations," *Physica D: Nonlinear Phenomena*, vol. 212, no. 3-4, pp. 305–316, 2005.

[167] V. Skarka, N. Aleksić, M. Lekić, B. Aleksić, B. Malomed, D. Mihalache, and H. Leblond, "Formation of complex two-dimensional dissipative solitons via spontaneous symmetry breaking," *Physical Review A*, vol. 90, no. 2, p. 023845, 2014.

[168] O. Descalzi and H. R. Brand, "Breaking of symmetry of interacting dissipative solitons can lead to partial annihilation," *Physical Review E*, vol. 101, no. 4, p. 040201, 2020.

[169] S. T. Cundiff, B. Collings, N. Akhmediev, J. M. Soto-Crespo, K. Bergman, and W. Knox, "Observation of polarization-locked vector solitons in an optical fiber," *Physical review letters*, vol. 82, no. 20, p. 3988, 1999.

[170] M. Marconi, J. Javaloyes, S. Barland, S. Balle, and M. Giudici, "Vectorial dissipative solitons in vertical-cavity surface-emitting lasers with delays," *Nature Photonics*, vol. 9, no. 7, pp. 450–455, 2015.

[171] E. Averlant, M. Tlidi, H. Thienpont, T. Ackemann, and K. Panajotov, "Vector cavity solitons in broad area vertical-cavity surface-emitting lasers," *Scientific reports*, vol. 6, no. 1, pp. 1–7, 2016.

[172] M. Delqué, G. Fanjoux, and T. Sylvestre, "Induced symmetry-breaking and polarization switching of spatial solitons through vector collision," in *Bragg Gratings, Photosensitivity, and Poling in Glass Waveguides*, p. JMD22, Optical Society of America, 2007.

[173] R. Bonifacio and L. Lugiato, "Instabilities for a coherently driven absorber in a ring cavity," *Lettere al Nuovo Cimento (1971-1985)*, vol. 21, no. 15, pp. 510–516, 1978.

[174] B. Segard and B. Macke, "Self-pulsing in intrinsic optical bistability with two-level molecules," *Physical review letters*, vol. 60, no. 5, p. 412, 1988.

[175] J. McSloy, W. Firth, G. Harkness, and G.-L. Oppo, "Computationally determined existence and stability of transverse structures. ii. multi-peaked cavity solitons," *Physical Review E*, vol. 66, no. 4, p. 046606, 2002.

[176] L. Hill, G. Xu, J. Fatome, G.-L. Oppo, S. G. Murdoch, M. Erkintalo, and S. Coen, "Breathing dynamics of symmetry-broken polarized temporal cavity solitons in kerr ring resonators," in *Nonlinear Photonics*, pp. NpTu1D–3, Optical Society of America, 2020.

[177] G. Xu. Private communication, 24/06/2020.

[178] M. Alam, "Universal unfolding of pitchfork bifurcations and shear-band formation in rapid granular couette flow," *arXiv preprint cond-mat/0411572*, 2004.

[179] K. R. Meyer, "Singularities and groups in bifurcation theory, volume i (martin golubitsky and david g. schaeffer)," 1986.

[180] M. Golubitsky and D. Schaeffer, "A discussion of symmetry and symmetry-breaking," in *Proceedings of Symposia in Pure Mathematics*, vol. 40, pp. 499–515, AMER MATHEMATICAL SOC 201 CHARLES ST, PROVIDENCE, RI 02940-2213 USA, 1983.

[181] M. Golubitsky, I. Stewart, and D. G. Schaeffer, *Singularities and Groups in Bifurcation Theory: Volume II*, vol. 69. Springer Science & Business Media, 2012.

[182] T. B. Benjamin, "Bifurcation phenomena in steady flows of a viscous fluid. i. theory," *Proceedings of the Royal Society of London. A. Mathematical and Physical Sciences*, vol. 359, no. 1696, pp. 1–26, 1978.

[183] S. Pitois, G. Millot, and S. Wabnitz, "Nonlinear polarization dynamics of counterpropagating waves in an isotropic optical fiber: theory and experiments," *JOSA B*, vol. 18, no. 4, pp. 432–443, 2001.

[184] J. C. Butcher, "A history of runge-kutta methods," *Applied numerical mathematics*, vol. 20, no. 3, pp. 247–260, 1996.

[185] P. Suarez, "An introduction to the split step fourier method using matlab," 2016.

[186] G. Muslu and H. Erbay, "A split-step fourier method for the complex modified korteweg-de vries equation," *Computers & Mathematics with Applications*, vol. 45, no. 1-3, pp. 503–514, 2003.